Studies on Electronic Phase in High Magnetic Field for Layered Organic Conductors
（層状有機導体における強磁場電子相の研究）

Shiori Sugiura

February 2018

Studies on Electronic Phase in High Magnetic Field for Layered Organic Conductors

Shiori Sugiura

Doctoral Program in Materials Science and Engineering

Submitted to the Graduate School of
Pure and Applied Sciences
in Partial Fulfillment of the Requirements
for the Degree of Doctor of Philosophy in
Engineering

at the
University of Tsukuba

Contents

Abstract

Organic conductors have attracted considerable interest because of their fascinating electronic states, including Mott insulating, charge-ordering, metallic, and superconducting states. These states arise from the variety of the molecules and stacking structures. Many organic conductors have various layered structures composed of organic donor and accepter molecules. Because of the charge transfer from the donor to accepter molecules, hole charge carriers are introduced into the donor molecule layers, which form the highly two-dimensional (2D) or one-dimensional (1D) energy bands. The energy bands are well reproduced by the tight-binding approximation; it shows that the molecular orbitals are localized in each organic molecule. Because of the localization characteristic, the Coulomb correlation between the conducting π electrons is relatively enhanced, which leads to fascinating physical properties at low temperatures and high magnetic fields.

Among various layered organic conductors, in this dissertation, two types of highly 2D organic conductors are studied, and the results of the following research topics are separately presented: (1) Electronic and magnetic properties of the organic π–d system λ-$(BETS)_2FeCl_4$ and (2) Novel superconducting phase in the layered organic conductor β"-$(BEDT\text{-}TTF)_2SF_5CH_2CF_2SO_3$

To investigate the characteristic electronic states, systematic measurements of electric conductivity, magnetic torque, and magnetocaloric effects at low temperatures and high magnetic fields are performed. Important results that provide novel insights into the electronic states are obtained. In this dissertation, the brief overview of the results and conclusions for the target materials are presented.

Chapter 1 Electronic and magnetic properties of the organic π–d system

In strongly correlated electronic systems, an interplay between magnetism and electronic conduction has been extensively studied because it leads to fascinating electronic properties. Among various strongly correlated systems, the so-called π–d system in organic conductors, where there is a strong exchange interaction between the π electrons in the conducting organic layers and the localized $3d$ spins in the insulating layers, has attracted particular interest. This is because of its unique magnetic field–temperature phase diagram, including antiferromagnetic (AF) order, metal–insulator (M–I) transition, and superconducting (SC) transition.

A layered organic conductor λ-$(BETS)_2FeCl_4$ [BETS = bis(ethylenedithio)tetraselenafulvalene] is a typical π–d system; it is composed of the conducting BETS layers and insulating $FeCl_4$ layers. A highly two-dimensional (2D) energy band is formed by the π electrons in the conducting layers, and the $3d$ spins of the Fe^{3+} ions ($S = 5/2$) are localized in the insulating layers.

For λ-$(BETS)_2FeCl_4$, some anomalous phenomena have been observed by various experiments in a wide range of temperatures and fields. In the paramagnetic metallic (PM) phase, a large dielectric constant is observed for $T_{MI} < T < 70$ K by microwave response measurements at 44.5 GHz, which suggests that dielectric domains or stripes with less metallic conduction

inhomogeneously emerge in the π electronic state. The inhomogeneity is consistent with the observation of the splitting of a Bragg reflection peak by synchrotron radiation experiments and the broadening of the NMR line shape. In the antiferromagnetic insulating (AFI) phase, a large frequency dispersion is observed in the microwave response, which is ascribed to some collective modes associated with the charge degree of freedom of the π electrons. The polarization curves $P(E)$ obtained from in-plane dielectric constant measurements show a steep increase in the saturation value of P for $\mu_0 H > 5$ T, suggesting a certain dielectric order. At $T_{\rm MI}$, a first-order structural phase transition is known to takes place,but no detailed structural studies have been carried out so far.

(1) Charge transport in the antiferromagnetic insulating phase of λ-$(BETS)_2FeCl_4$

Resistance and dielectric constants have been measured in the AFI phase of the quasi-two-dimensional organic conductor λ-$(BETS)_2FeCl_4$ to understand charge transport. Nonlinear current–voltage (I–V) characteristics are observed at low temperatures, which are explained by a charge transport model based on the electric-field dependent Coulomb potential between thermally excited electrons and holes. A small dip in the magnetic field dependence of the resistance is found at 1.2 T, which is ascribed to a spin-flop transition. The large difference between the in-plane and out-of-plane dielectric constants shows the two-dimensionality of the Coulomb potential, which is consistent with the charge transport model. The angular dependence of the metal–insulator (M–I) transition field is determined and it suggests that the Zeeman effect of the 3d spins of the Fe ions plays an essential role.

(2) Magnetic torque studies in λ-$(BETS)_2FeCl_4$

Systematic measurements of the magnetic torque τ_m of the organic conductor λ-$(BETS)_2FeCl_4$ are performed to investigate the magnetic properties. In the magnetic field dependence of τ_m, a very sharp structure is observed at $\sim$1.2 T, which is attributed to the spin-flop transition. A step-like structure associated with a small hysteresis appears at $\sim$10 T, which is caused by the AFI–PM transition. In the angular dependence of τ_m for magnetic fields in the b^*–c plane, it is found that the zero-crossing angles significantly change with field and temperature. The changes provide reasonable evidence for the antiferromagnetic order of the π spins (not the Fe 3d spins) in the AFI phase. As a function of field angle, the AFI–PM transition field is minimum when the magnetization of the 3d spins is maximum.

(3) Magnetocaloric effect studies in λ-$(BETS)_2FeCl_4$

Magnetocaloric effect (MCE) measurements have been carried out in the π–d system λ-$(BETS)_2FeCl_4$. They show an AFI phase below $\sim$8.5 K. The MCE, directly related to the magnetic entropy, shows a small sharp peak at the spin-flop transition and a sharp dip at the AFI–PM transition. The overall feature above 3 K is qualitatively interpreted by a simple model of the antiferromagnetic (AF) π spins and paramagnetic 3d spins at the Fe sites. However, a broad dip in the MCE curve is additionally found at $\sim$5 T below $\sim$3 K, which is not explained by the above model. Comparison of the results with those of κ-$(BETS)_2FeBr_4$, indicates an AF

order of the $3d$ spins at the Fe sites.

Chapter 2. Novel superconducting phase in the layered organic conductor

In layered organic superconductors, the perpendicular coherence length is comparable to the interlayer spacing. Therefore, the layered structures can be modeled as stacks of Josephson junctions. When the field is applied parallel to the superconducting layers, the orbital effect against superconductivity is strongly quenched, which is the main reason of the anisotropic upper critical field (H_{c2}). In addition, the superconductivity is in a clean limit for most of organic superconductors. These two conditions, namely, the quenched orbital effect and clean-limit superconductivity, are particularly favorable for the emergence of a novel superconducting phase, the so-called Fulde–Ferrell–Larkin–Ovchinnikov (FFLO) phase. For conventional superconductors, the Zeeman effect breaks the superconductivity, giving the Pauli paramagnetic limit $H_{\rm Pauli}$. However, the FFLO superconductivity can survive even above $H_{\rm Pauli}$ sufficiently below T_c in parallel fields. The Cooper pairs in the FFLO phase are formed between the up and down spins on the Fermi surface polarized by the magnetic field. Consequently, the Cooper pairs have a non-zero center-of-mass momentum q, which leads to an order parameter oscillation (periodic nodal lines) in the real space, $\Delta = \Delta_0 \cos(qr)$. The FFLO transition from the homogeneous (conventional) superconducting phase is expected to occur at $\sim H_{\rm Pauli}$.

In the last decade, extensive efforts have been devoted to observed the FFLO phase in various layered organic superconductors, which are the best candidates for FFLO phase studies. At the FFLO phase transition, the formation of the nodal lines in the superconducting layers inevitably leads to a vortex reconfiguration. On the other hand, in highly 2D superconductors, each flux line can be decomposed into two parts: pancake vortex in the superconducting layer and Josephson vortex penetrating in the insulating layers between the superconducting layers. Depending on the field strength and direction, these vortex states are expected to show melting, layer decoupling, and so on, which make difficult to identify the FFLO transition unambiguously. Among the various thermodynamic quantities, the MCE is known to be highly sensitive to field-induced phase transitions. Therefore, the MCE is a powerful tool to investigate the FFLO transition as well as the vortex phase transitions.

The organic superconductor β"-(BEDT-TTF)$_2$SF$_5$CH$_2$CF$_2$SO$_3$ with the critical temperature $T_{\rm c} \approx 5$ K, where BEDT-TTF is bis(ethylenedithio)tetrathiafulvalene, has a layered structure composed of the BEDT-TTF conducting and SF$_5$CH$_2$CF$_2$SO$_3$ insulating layers. Because of the large SF$_5$CH$_2$CF$_2$SO$_3$ anion, the energy band formed by the BEDT-TTF molecular orbitals is highly 2D.

(1) Magnetic torque measurements

The angular and the field dependences of the magnetic torque are measured in β"-(BEDT-TTF)$_2$SF$_5$CH$_2$CF$_2$SO$_3$. Each torque curve exhibits a hysteresis between the up and down sweeps of the magnetic field, where the irreversibility fields ($H_{\rm irr}$) can be defined. The irre-

versible torque curve is caused by the strong pinning of the magnetic fluxes in the superconducting layers. The perpendicular diamagnetic susceptibility $-dM_z/dH_z$ as a function of field at various temperatures are obtained from the angular dependence of the magnetic torque.The diamagnetic signals at all the temperatures decrease with increasing field, which are associated with kink structures. The kink field $H_{\rm kink}$ is lower than $H_{\rm irr}$ for $T \leq 1.1$ K, which corresponds to the Pauli paramagnetic limit ∼9.9 T. The reduction of the diamagnetic susceptibility below $H_{\rm irr}$ with increasing magnetic field shows the presence of the FFLO phase.

(2) Magnetocaloric effect measurements

In the MCE ΔT curves, three series of peaks are observed. Only in a limited angle region ($|\theta| \lesssim 1.5°$), a broad peak (denoted by $H_{\rm peak1}$) is observed at ∼9.5 T, which is associated with a small hysteresis between the up and down sweeps.In general, ΔT changes the sign between the up and down sweeps due to the dH/dt term. However, supercooling and superheating processes lead to positive ΔT for both sweeps, which clearly shows that this is a first-order phase transition. With increasing temperature, the peak field $H_{\rm peak1}$ gradually decreases and the intensity is suppressed. This peak is ascribed to the FFLO transition. Since the periodic nodal line structure is formed in the FFLO phase, the vortices will be reconfigured in the sample, which also causes heating for both sweeps.

When the field is tilted from the superconducting layers, two additional series of peaks associated with a hysteresis are observed, namely sharp and broad peaks denoted by $H_{\rm peak2}$ and $H_{\rm peak3}$, respectively. Similarly, both the peaks are ascribed to first-order phase transitions. $H_{\rm peak2}$ and $H_{\rm peak3}$ show rapid increases as $\theta \to 0°$. The sharp peak at $H_{\rm peak2}$ suddenly vanishes at $\theta = -3.5°$. Similar angular dependence is observed at 1.7 K. The dip/peak in the up/down sweep at 1.7 K clearly shows that a high-field phase has a high magnetic entropy. The broad peak is observed at a lower field than the sharp peak. As $\theta \to 0°$, the intensity is suppressed but it is still visible at $\theta \approx 0°$.

(3) Resistance measurements

The resistance measurements are performed to investigate the FFLO phase and the vortex dynamics in the superconducting phase. In the angular dependence of the resistance, an angular-dependent magnetoresistance oscillation is observed, which is caused by the periodic orbital motion on the 2D Fermi surface. From these data, the cross section of the 2D Fermi surface of β"-(BEDT-TTF)$_2$SF$_5$CH$_2$CF$_2$SO$_3$ can be precisely obtained.

In the parallel fields, a non-zero interlayer resistance is observed in a wide field region, which is caused by the Josephson vortex dynamics. In the second-derivative curves, oscillatory behavior is observed in a high-field region below $H_{\rm c2}$. The oscillatory behavior is interpreted as the magnetic field-dependent commensurability effect between the wavelength of the FFLO order parameter oscillation $\lambda_{\rm FFLO}$ and the Josephson vortex lattice constant l. From the results at various temperatures, the magnetic field-temperature phase diagram of the FFLO phase is obtained, which is consistent with the MCE data.

Part I

Introduction of layered organic conductors

Chapter 1

Background

Until the beginning of the 20th century, organic compounds composed of non-metallic atoms were considered to be electrical insulators because they have closed-shell structures. However, in 1954, H. Akamatsu, H. Inokuchi and Y. Matsunaga synthesized a perylene-bromine complex, the first conducting organic material. In this complex, the halogen incorporated in the solid extracts electrons from the insulating perylene molecule. Because of the charge transfer, hole charge carriers are introduced into the organic molecules, which contribute to the conduction properties. After this discovery, various highly conducting organic materials, the so-called “charge transfer salts” or simply “organic conductors” have been synthesized, in which the charge transfer between different molecules plays an essential role. Because of their fascinating electronic properties, organic conductors have attracted immense interest and have been extensively studied so far.

The charge transfer salts have layered structures, composed of donor and acceptor molecule layers. Typical donor molecules are shown in Fig. 1 The schematic structure of the charge transfer salts is presented in Fig. 2.

Because of the charge transfer from the donor to acceptor molecules, hole charge carriers are introduced in the donor molecules although the acceptor molecules have closed shells.

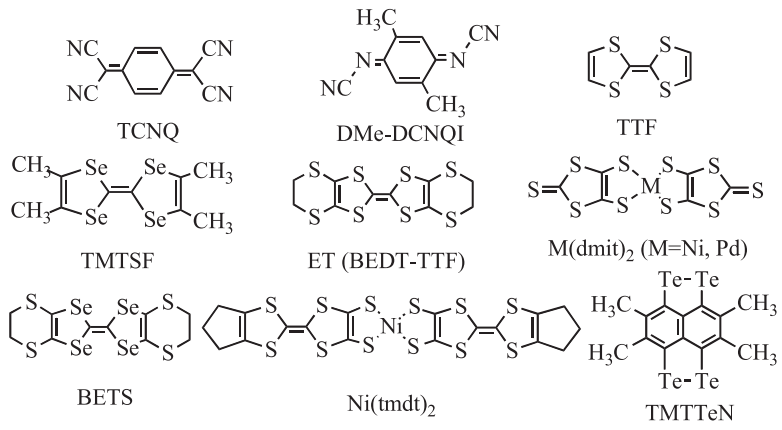

Figure 1: Donor molecules and their abbreviations.[1)]

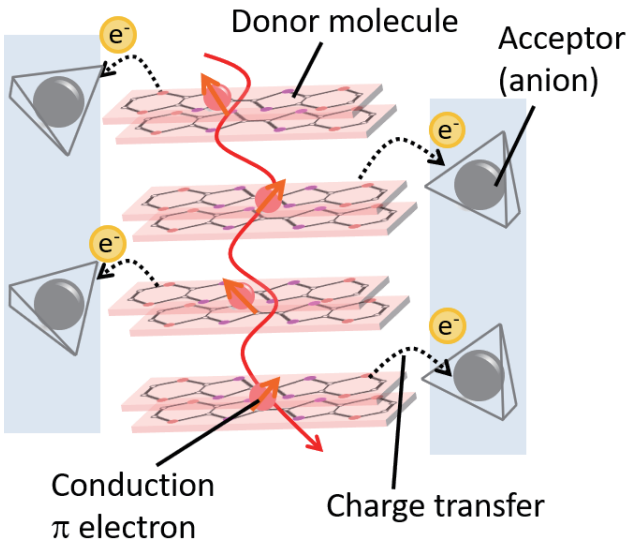

Figure 2: Schematic illustration of charge transfer between donor and acceptor molecule layers.

Consequently, the highest occupied molecular orbital (HOMO) of the donor molecule, which overlaps with those of the neighboring molecules, forms an energy band in the donor molecule layer. Because of this layered structure of the salt, its electronic state is highly anisotropic. Since the HOMO is mainly made of the π orbitals of the S or Se atoms, the conducting carriers are called "π electrons".

In the 1980's, the first superconductivity of charge transfer salts was discovered for $(TMTSF)_2PF_6$, which has a one-dimensional (1D) electronic structure. This salt shows a metal–insulator (M–I) transition at ambient pressure. This M–I transition is suppressed by a high pressure and then the salt shows superconductivity at $T_c = 0.9$ K. Following this discovery, various organic superconductors with higher T_c have been synthesized, most of which have two dimensional (2D) electronic states. The highest T_c in the charge transfer salts is $\sim$14 K in β'-(BEDT-TTF)$_2$ICl$_2$.[2)]

In charge transfer salts, the diversity of the structures and molecular combinations is responsible for the various conduction and magnetic properties. In addition, the donor molecular arrangement drastically affect the electronic states. Typical molecular arrangements, denoted by Greek letters, are depicted in Fig. 3.

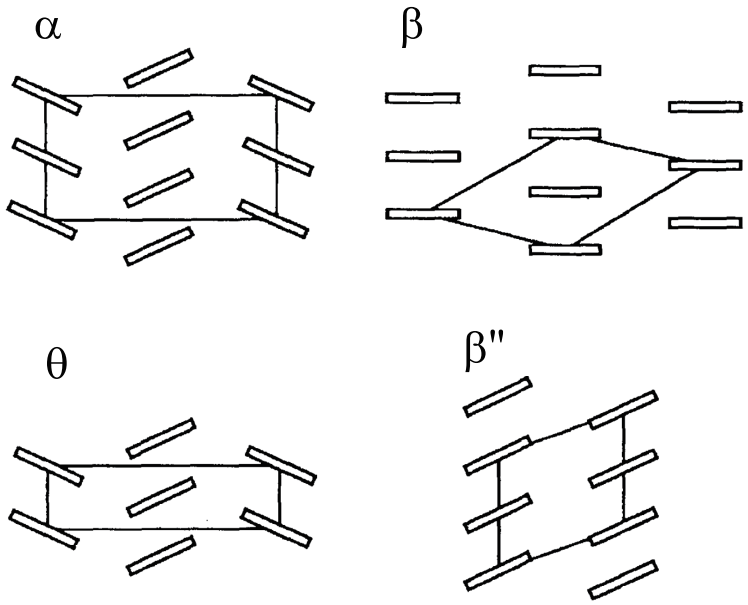

Figure 3: Molecular arrangements in the conducting layers of charge transfer salts[3)]

1.1 π–d organic systems

In strongly correlated electron systems, an interplay between magnetism and electronic conduction has been extensively studied, because it contributes to fascinating electronic properties. In charge transfer salts, the accepter molecules (anions) play an important role not only in the charge transfer from the donor molecules but also in imparting magnetic properties by introducing $3d$ local moments. Such magnetic organic salts are called π–d systems. The first metallic π–d system, (BEDT-TTF)$_4$H$_3$OFe(C$_2$O$_4$)$_3$C$_6$H$_5$CN was synthesized by Kurmoo et al., where large local $3d$ moments of the Fe ions are incorporated. This salt shows metallic conductivity at low temperatures and superconductivity at 7 K. However, the exchange interaction between the conducting π electrons and local $3d$ spins (π–d interaction) is negligibly small; the conducting and magnetic layers seem to be almost independent to each other.[4)]

Coronado *et al.* discovered the first ferromagnetic organic metal, (BEDT-TTF)$_3$[MnCr(C$_2$O$_4$)$_3$], which shows a ferromagnetic transition at 5.5 K and an extremely small coercive field of $\sim$0.001 T. Although the coexistence of metallic conductivity and ferromagnetic order was realized, the π–d interaction was extremely small.[5)]

The magnetic interaction between d and π electrons is written as

$$-J_{\pi d}\,(r)\,S_\pi \cdot S_d, \tag{1}$$

where S_π and S_d are the conducting spin and localized d spin, respectively, and $J_{\pi d}$ is the π–d interaction.

Among various π–d systems, λ-(BETS)$_2$FeCl$_4$ has the largest $J_{\pi d}$ and a characteristic field–temperature phase diagram. Such unique properties are attributed by a strong π–d interac-

Table 1: π–d organic systems

materials	$J_{\pi d}$ (K)	properties	References
λ-(BETS)$_2$FeCl$_4$	18	$T_{\rm N} = T_{\rm MI} = 8.3$ K, $T_{\rm c} = 5$ K	[1,6,7]
κ-(BETS)$_2$FeBr$_4$	8	Br: $T_{\rm N} = 2.5$ K, $T_{\rm c} = 1.3$ K	[1,6,7]
κ-(BETS)$_2$FeCl$_4$	3	Br: $T_{\rm N} = 0.45$ K, $T_{\rm c} = 0.1$ K	[6,8]
κ-(BDH-TTP)$_2$FeBr$_4$	2.6	$T_{\rm N} = 3.9$ K	[9]
(EDO-TTFVO)$_2$FeCl$_4$	2.91	$T_{\rm N} = 2.91$ K, metallic down to 0.3 K	[10]
(EDT-DSDTFVO)$_2$FeBr$_4$	7.58	metallic down to 4.2 K	[11]
(EDO-TTFVODS)$_2$FeBr$_4$	15	$T_{\rm N} = 3.3$ K	[12]

$T_{\rm N}$: Neel temperature, $T_{\rm MI}$: M–I transition temperature

$T_{\rm c}$: superconducting transition temperature

tion. In this dissertation, one of the research topics is the electronic state of λ-(BETS)$_2$FeCl$_4$. κ-(BETS)$_2$FeX$_4$ (X = Br, Cl) is the first antiferromagnetic (AF) metal that shows superconductivity at $\sim$1 K. κ-(BDH-TTP)$_2$FeX$_4$ is also metallic and shows an AF transition. All the other salts are semiconducting or insulating at low temperatures (Table 1).

1.2 Superconductivity

After liquid helium was successfully achieved by H. C. Onnes, superconductivity of mercury (critical temperature $T_{\rm c} = 4.15$ K) was discovered in 1911 using liquid helium. Following this, the superconducting state of many metallic elements, alloys, intermetallic compounds, and organic crystals at low temperature or high pressure has been confirmed.

In the frame-work of the standard superconducting theory, the BCS theory, superconductivity is stabilized by the condensation of Cooper pairs formed by antiparallel spins with momenta $\mathbf{k}$ and $-\mathbf{k}$ near the Fermi surface. The Cooper pairs are mediated by electron–phonon interaction. In perturbation theory, the electron-phonon interaction is given by

$$\mathcal{H}_1 = -\frac{g}{2\Omega}\sum_{\mathbf{q}_1}\sum_{\mathbf{k}_1\sigma_1}\sum_{\mathbf{k}_2\sigma_2} c^\dagger_{\mathbf{k}_1+\mathbf{q}_1\sigma_1} c_{\mathbf{k}_1\sigma_1} c^\dagger_{\mathbf{k}_2+\mathbf{q}_1\sigma_2} c_{\mathbf{k}_2\sigma_2} \ . \tag{2}$$

g and Ω are the electron–phonon coupling constant and volume, respectively. By the mean field approximation, this is reduced to

$$\mathcal{H}_1 = -\frac{g}{\Omega}\sum_{\mathbf{k}\mathbf{k}'}\left[\left\langle c^\dagger_{\mathbf{k}'_\uparrow} c^\dagger_{\mathbf{k}'_\downarrow}\right\rangle c_{-\mathbf{k}_\downarrow} c_{\mathbf{k}_\uparrow} + h.c.\right] = -\sum_{\mathbf{k}}\left[\Delta^\dagger c_{-\mathbf{k}_\downarrow} c_{\mathbf{k}_\uparrow} + h.c.\right] \tag{3}$$

Many of the basic superconducting phenomena are well understood by the BCS theory based on the above mentioned approximation. Here,

$$\Delta = \frac{g}{\Omega} \sum_{\mathbf{k}} \left\langle c^{\dagger}_{\mathbf{k}'_{\uparrow}} c^{\dagger}_{\mathbf{k}'_{\downarrow}} \right\rangle \tag{4}$$

is an order parameter of superconductivity. According to the BCS theory, the magnitude of Δ is equal to that of the energy gap of the superconductor's quasiparticle excitation; the energy of the entire system reduces by

$$E_c = \frac{1}{2} N(0) |\Delta|^2 \tag{5}$$

by using the density of state at the Fermi energy $N(0)$ than in the normal state.

The superconducting state is generally destroyed by magnetic fields by two mechanisms; the Zeeman effect and orbital effect. In the normal BCS state, the Cooper pairs are formed by up and down spins, which can not contribute to spin splitting. Therefore, in the magnetic field, the superconducting state is more unstable than the normal state. When the spin splitting energy is equal to the condensation energy, that is,

$$\frac{1}{2} \chi H^2 = \frac{1}{2} N(0) |\Delta|^2 , \tag{6}$$

the BCS state is destroyed. This effect is called the paramagnetic pair-breaking effect, which originally arises from the Zeeman effect. In this way, the Zeeman effect gives the upper limit of the critical field, called the Pauli limit H_{Pauli}. Using the Pauli susceptibility $\chi = 2\mu_{\mathrm{B}}^2 N(0)$ of the free electron model, H_{Pauli} is given by

$$H_{\mathrm{Pauli}} = \frac{\Delta}{\sqrt{2}\mu_{\mathrm{B}}}. \tag{7}$$

The Pauli limit sets a strong limit of the critical magnetic field.

For type-II superconductors in the magnetic field, the orbital effect leads to the emergence of an Abrikosov vortex state, forming a regular array of vortex lines parallel to the field. The kinetic energy of the superconducting current around the vortex cores reduces the superconducting condensation energy. The orbital limiting field at which vortex cores begin to overlap is simply given as

$$H_{\mathrm{orb}} = \Phi_0 / 2\pi\xi^2. \tag{8}$$

Here, $\Phi_0 = \pi\hbar c/|e|$ is the flux quantum and ξ is the superconducting coherence length. The upper critical field is determined by both Zeeman and orbital effects. The relative importance of both effects in the suppression of superconductivity is described by the Maki parameter

$$\alpha = \sqrt{2} \frac{H_{\mathrm{orb}}}{H_{\mathrm{Pauli}}} , \tag{9}$$

which is the ratio of H_{orb} to H_{Pauli} at $T = 0$.

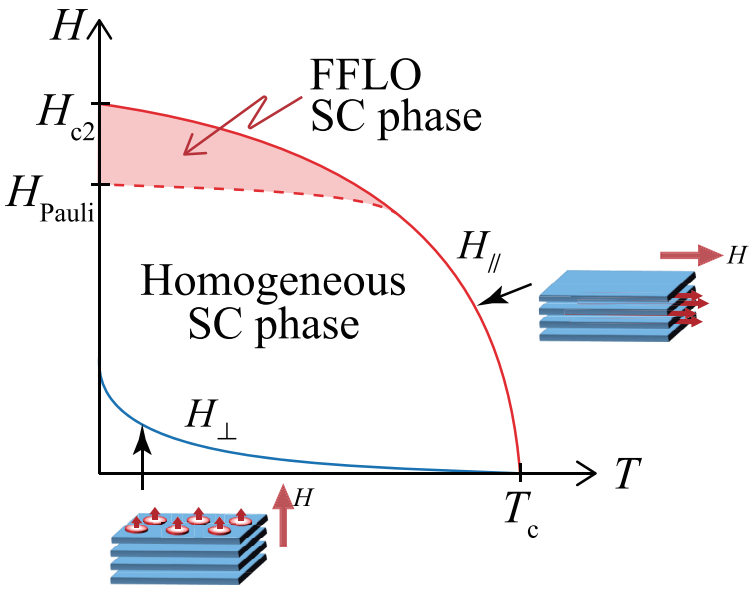

Figure 4: Schematic H–T phse diagram.

1.3 FFLO state

Novel superconductivity is one of the most intriguing topics in solid state physics. In general, the superconducting Cooper pairs are broken by the Zeeman effect, which gives the Pauli paramagnetic limit H_{Pauli}.[67] The paramagnetic pair-breaking effect is reduced by the formation of a new pairing state $(\mathbf{k}\uparrow, -\mathbf{k}\downarrow +q)$ with $q \approx 2\mu_{\mathrm{B}}H/\hbar v_{\mathrm{F}}$, where v_{F} is the Fermi velocity and q is the center-of-mass momentum. The mechanism is called the Fulde–Ferrell–Larkin–Ovchinnikov (FFLO) state, which was theoretically established by P. Fulde, R. A. Ferrell, A. Larkin, and Y. Ovchinnikov in 1964.[13,14] In high magnetic fields, the Fermi surface is polarized by the Zeeman effect, and up and down spin Fermi surfaces are formed. In the FFLO phase, Cooper pairs are formed between polarized Fermi surfaces and, consequently, have a non-zero center-of-mass momentum q.

Using the center-of-mass coordinate $\mathbf{r}$, the order parameter is given as

$$\Delta(\mathbf{r},\rho) = \frac{1}{\Omega}\sum_{\mathbf{k}} e^{i\mathbf{k}\rho} \sum_{\mathbf{q}} e^{i\mathbf{k}\mathbf{r}} \left\langle c_{-\mathbf{k}+\frac{\mathbf{q}}{2}\downarrow} c_{\mathbf{k}+\frac{\mathbf{q}}{2}\uparrow} \right\rangle \tag{10}$$

and

$$\Delta(\mathbf{r},\mathbf{k}) = \sum_{\mathbf{q}} e^{i\mathbf{q}\mathbf{r}} \left\langle c_{-\mathbf{k}+\frac{\mathbf{q}}{2}\downarrow} c_{\mathbf{k}+\frac{\mathbf{q}}{2}\uparrow} \right\rangle \tag{11}$$

is obtained, where $\Delta(\mathbf{r},\mathbf{k}) \equiv \int d^3\mathbf{r}\rho e^{ik\rho}\Delta(\mathbf{r},\rho)$. In the FFLO phase, the order parameter is obtained as

$$\Delta(\mathbf{r},\mathbf{k}) \propto \cos(\mathbf{q}\mathbf{r}), \tag{12}$$

This equation implies that a non-zero center-of-mass momentum q leads to an order parameter oscillation (periodic nodal lines) in the real space.

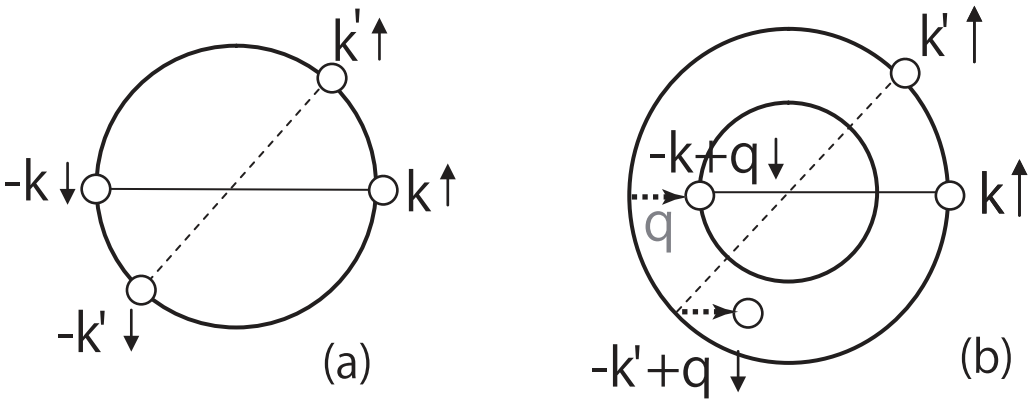

Figure 5: Schematic illustration of paring states.[68)]

In the homogeneous superconducting phase, the wave length of the FFLO order parameter oscillation $\lambda_{\mathrm{FFLO}} = 2\pi/q$ is infinite, but it is expected to jump to a finite value at the FFLO phase transition. Subsequently, λ_{FFLO} decreases with increasing magnetic field up to H_{c2}. At H_{c2}, λ_{FFLO} will be comparable to the in-plane coherence length $\xi_{\|}$; $\xi_{\|}$ sets the lower limit of λ_{FFLO}.

The FFLO phase can be stabilized in clean type-II superconductors with a large orbital critical field such that pair breaking by the orbital effect is suppressed more strongly than by the Zeeman effect. Therefore, the Maki parameter α must be greater than 1.

Layered organic conductors are clean type-II superconductors, where the orbital effect can be strongly reduced by applying the magnetic field exactly parallel to the conducting layers. In such cases, the Maki parameter increases, which is one of the necessary conditions for the FFLO phase. Therefore, the layered organic superconductors are the best candidates for the study of the FFLO phase. Some indications that suggest the presence of the FFLO phase have been reported for some 2D superconductors.[69–72,82,85,102)]

1.4 Vortex phases

Below the lower critical field H_{c1}, there is no penetration of flux in the superconductor, whereas when the applied field strength is between H_{c1} and H_{c2}, partial penetration of flux cores. In highly 2D superconductors, each flux line can be decomposed into two parts: pancake vortex (PV) in the superconducting layer and Josephson vortex (JV) penetrating in the insulating layers between the superconducting layers. The superconductivity develops a mixed state, where microscopic structure of both normal and superconducting regions is formed.

In the mixed state, superconducting vortices can be viewed as non-superconducting (normal) cores surrounded by circulating superconducting current. Outside of the core of the vortices, the superconducting material retains its superconducting nature, and the field decays in accordance with the London equation. Because the vortices behave like particles with repulsive interaction,

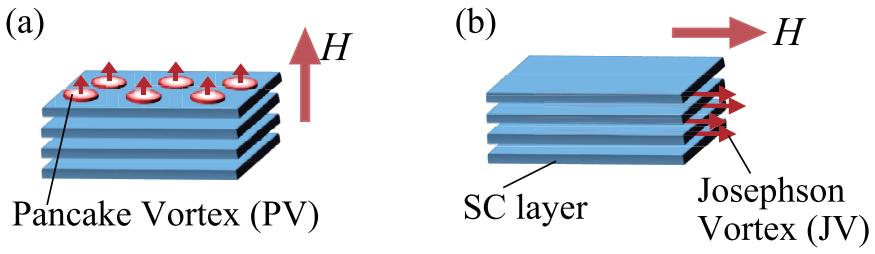

Figure 6: Schematic illustration of pancake and Josephson vortices.

they are called vortex matter.

The vortex matter has been extensively studied because of the fascinating phenomena associated with it especially for highly 2D layered superconductors. In layered superconductors, a perpendicular superconducting coherence length $\xi_\perp$ is comparable to the thickness of the superconducting layer. Each superconducting layer sandwiched by insulating layers is Josephson-coupled with the next layers (Josephson couple). Therefore, layered superconductors can be modeled as stacks of Josephson junctions.

PVs are formed in the individual superconducting layers, whose core radius is given by the in-plane coherence length $\xi_\parallel$. These PVs are pinned at some inhomogeneity in the superconducting layers, such as impurities, lattice defects, and sample edges, where the superconducting order parameter is reduced.

At low temperatures and magnetic fields, the superconducting layers are strongly Josephson-coupled, and the flux lines penetrate the superconducting layers in a straight path. The PVs form an elastically disordered but a nearly 3D regular lattice. This vortex phase is called Bragg glass, which is a glass and yet nearly as ordered as a perfect crystal. As the magnetic field strength increases, the Josephson coupling weakens and the disorder effect is effectively enhanced, resulting in entangled flux lines.

The weakening of Josephson coupling leads to decoupling of the superconducting layers but a disordered 2D lattice structure remains in each superconducting layer. This phase is called vortex glass. Because of the entangled structure in the vortex glass phase, the flux lines between the superconducting layers are kinked, where the JVs are formed. As the field further increases, the vortex glass melts, and both PVs and JVs fluctuate greatly (Fig. 8). Above the melting transition field, vortices take instantaneous positions but there is no long-range order; therefore, the system can be described as a vortex liquid.

Two mechanisms cause the melting transition; thermal and quantum fluctuations. As temperature increases, the thermal fluctuation amplitude enhances. When the fluctuation amplitude becomes comparable to the vortex lattice constant, the vortex solid melts at a certain temperature, which is called thermal melting. The strength of thermal fluctuations is measured on the basis of the Ginzburg number:

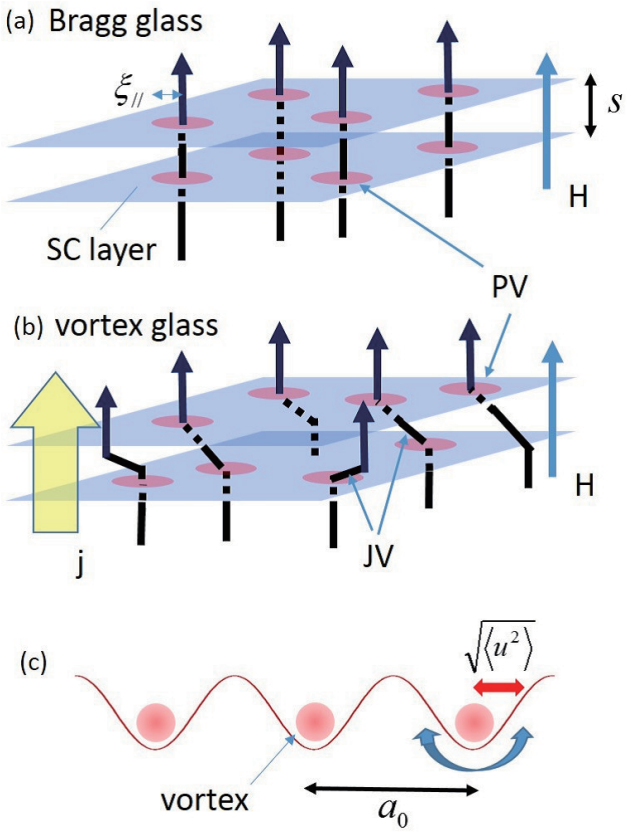

Figure 7: Schematics of flux lines.[26)]

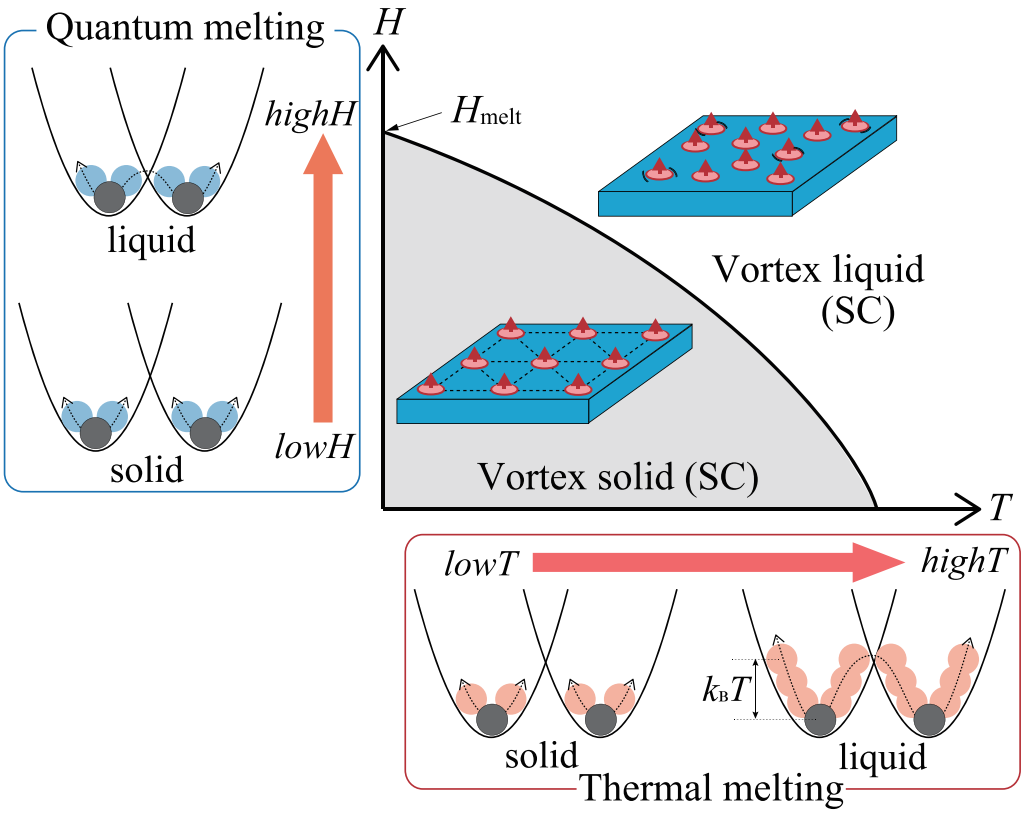

Figure 8: Schematic illustration of melting transitions of vortices.

$$G_i = \frac{1}{2}\left[\frac{T_c}{H_{c2}^2 m^* \xi_{\parallel}(0)^3}\right]^2 , \tag{13}$$

where m^* is an effective mass ratio, $m^* = m_{eff}^{\perp}/m_{eff}^{\parallel} = H_{c2}^{\perp}/H_{c2}^{\parallel}$, and $\xi_{\parallel}(0)$ is the in-plane coherence length at zero temperature. For classical 3D superconductors, $G_i \approx 10^{-11}$, whereas for layered organic superconductors and high-T_c cuprates, $G_i \approx 10^{-2}-10^{-3}$. On the other hand, as the magnetic field increases, the vortex lattice constants $a_{\mathrm{PV}} = \sqrt{\Phi_0/H}$ and $a_{\mathrm{JV}} = \Phi_0/sH$ decrease, where Φ_0 and s are the flux quantum and layer spacing, respectively. When the lattice constants become comparable to the amplitude of the vortex fluctuation, the vortex solid melts. This melting transition is called quantum melting transition and can take place even at zero temperature because of the zero-point quantum fluctuation of the vortex lattice. The quantum fluctuations are quantified on the basis of the ratio of the normal state sheet resistivity of each layer (ρ_N) to quantum resistance $Q = (e^2/\hbar)\,\rho_N/d$, where d is the interlayer spacing.

In the organic superconductor κ(BEDT-TTF)$_2$Cu$_2$(NCS)$_2$, magnetothermal instabilities in the mixed state are observed, which are associated with transitions between metastable quasi 2D vortex lattice phases. The abrupt cessation of magnetization jumps associated with these instabilities serve as an indication of melting of this quasi 2D vortex lattice phase. It is suggested that the melting transition may be driven by quantum rather than thermal fluctuations.[27)]

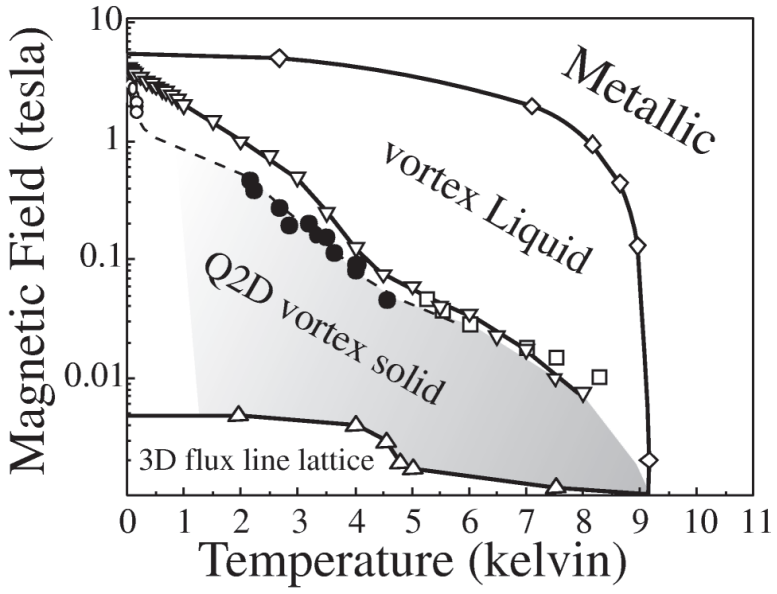

Figure 9: Mixed state vortex phase diagram of κ-(BEDT-TTF)$_2$Cu$_2$(NCS)$_2$.[27)]

Chapter 2

Research subjects

2.1 λ-$(BETS)_2FeCl_4$

A single crystal of λ-$(BETS)_2FeCl_4$[BETS=bis(ethylenedithio)tetraselenafulvalene] was synthesized by conventional electrochemical method.[7,64] The structure was determined at 10 K and 298 K. The crystal contains triclinic unit cells with space group $P\bar{1}$ (Table 2). The crystal structure is shown in Fig. 10. Two BETS molecules and the $FeCl_4^-$ anion are crystallographically independent. The BETS molecules are stacked along the a axis.

The extended Huckel tight-binding band calculation yields a 2D closed Fermi surface with 23%of the Brillouin zone and a corrugated extended Fermi surface. (Fig. 11) Although systematic temperature-dependent changes in the overlap integrals are barely observed, the gap between the two types of Fermi surfaces becomes small at 10 K.

λ-$(BETS)_2FeCl_4$ undergoes a metal–insulator (M–I) transition at 8.3 K (T_{MI}). The M–I transition is recognized as a Mott transition because of a strong on-site Coulomb repulsion. This is known to be a first order structural phase transition;[7] however, the detailed structural studies of this transition have not been performed yet. The resistivity slightly decreases with decreasing temperature and is maximum at ∼100 K, indicating the strong correlation of π electrons.[1,7] In the metallic phase, some interesting phenomena have been reported: large dielectric constants for $T_{MI} < T < 70$ K,[15] splitting of a Bragg reflection peak,[30] and broadening of the NMR line shape.[16,17] The results of the above mentioned reports allude to the ferroelectric-like metallic state in the PM phase.

The magnetic susceptibility measurements for the field applied parallel and perpendicular to the needle axes (|| c) revealed that the antiferromagnetic (AF) and M–I transition takes place cooperatively at T_{MI}. The spin-flop transition appears around 1.2 T. The magnetic torque experiments conducted by Sasaki et al. showed that the AF easy axis tilted from the c-axis by about 30°–40°.[55]

The antiferromagnetic insulating (AFI) phase below T_{MI} is broken by a magnetic field of ∼10 T, and the paramagnetic metallic (PM) phase is recovered. In the PM phase, the measurements of Shubnikov–de Haas oscillations confirm the presence of a 2D Fermi surface. (Fig. 13)[21,22]

Table 2: Crystal data and experimental details[7)]

Material	λ-$(BETS)_2FeCl_4$	
Chemical formula	$FeSe_8Cl_4S_8C_{20}H_{16}$	
Formula weight	1341.9	
Radiation	Mo(Kα)	
Temp	298 K	10 K
a/Å	16.164(3)	15.890(7)
b/Å	18.538(3)	18.378(8)
c/Å	6.5928(8)	6.531(4)
α/deg	98.40(1)	98.61(4)
β/deg	96.67(1)	96.67(1)
γ/deg	112.52(1)	112.05(3)
V/Å^3	1773.0(5)	1716(1)
Space group	$P\bar{1}$	$P\bar{1}$
Z	2	2
R, R_w	0.038, 0.038	0.087, 0.079
GOF	1.14	4.41

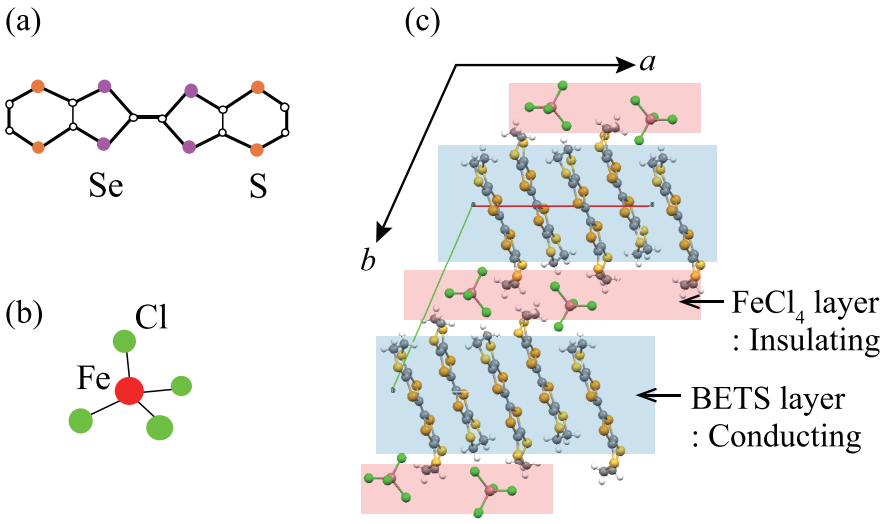

Figure 10: Crystal structures of λ-$(BETS)_2FeCl_4$[7)]

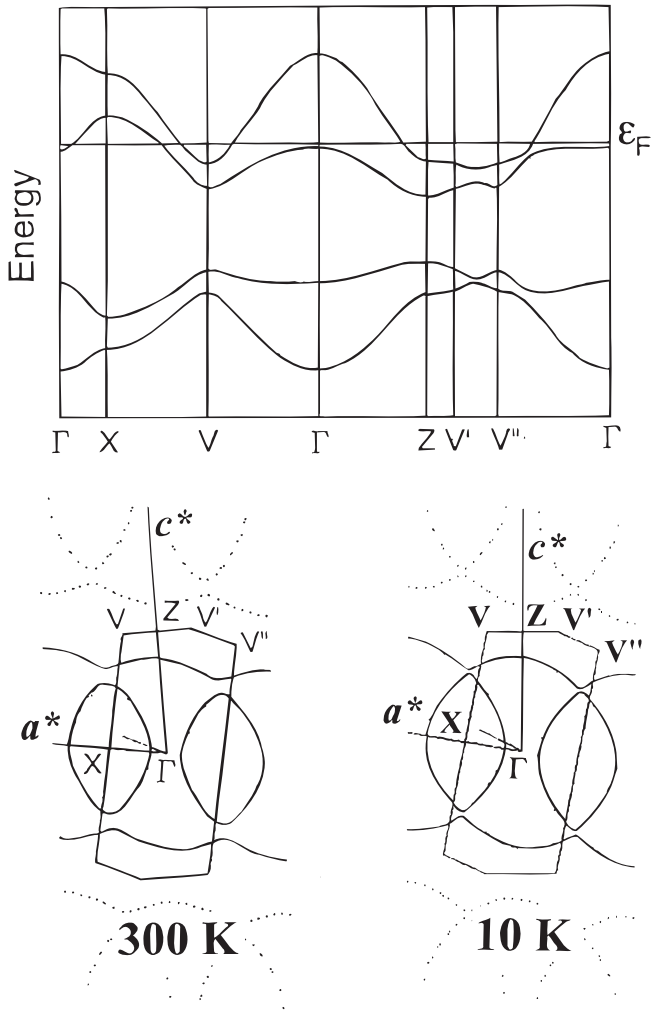

Figure 11: Band structure and Fermi surface of λ-$(BETS)_2FeCl_4$[7)]

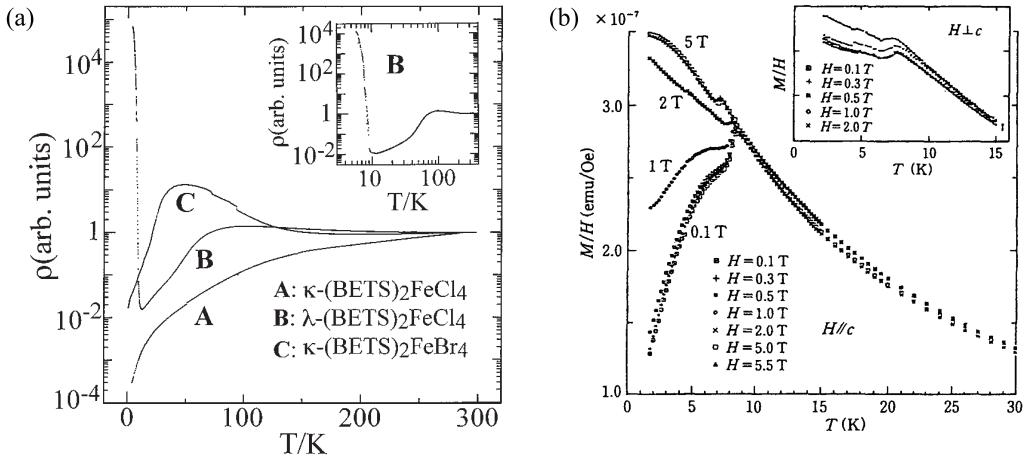

Figure 12: Resistance and magnetic susceptibility of λ-$(BETS)_2FeCl_4$[8)]

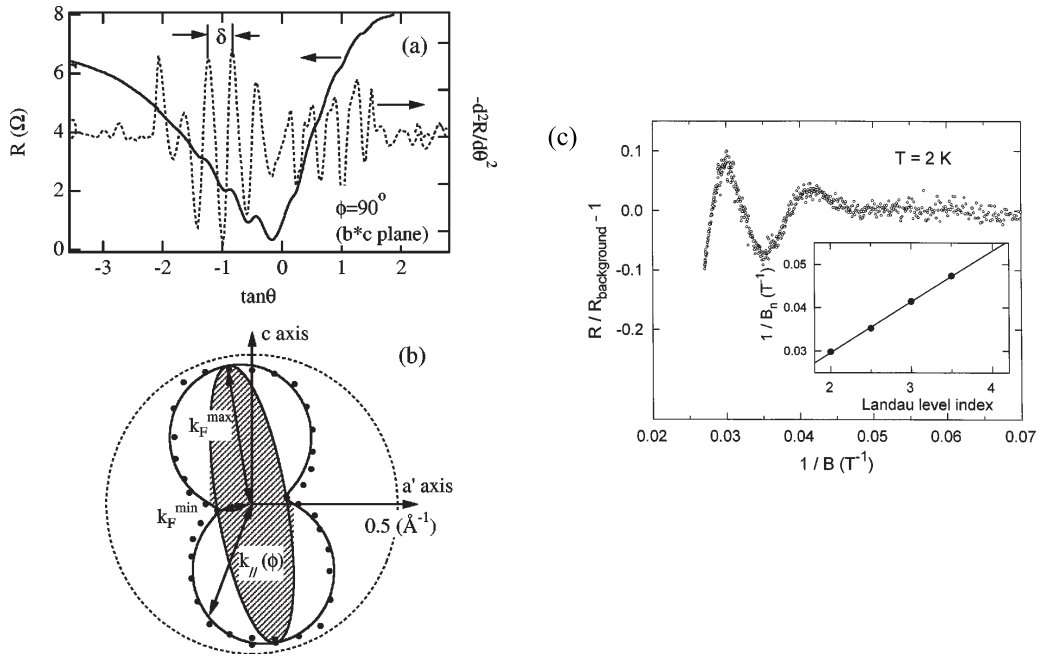

Figure 13: Angular-dependent magnetoresistance and SdH oscillations of λ-$(BETS)_2FeCl_4$.[18)]

These results agree well with the results of band calculation. In magnetic fields above ∼17 T, a superconducting phase is induced when the magnetic field is applied parallel to the conducting a'–c plane, which is explained by the Jaccarino–Peter compensation mechanism. In the field induced superconducting phase, the existence of a novel superconducting state, so-called the FFLO phase, near the upper critical field is suggested.[23,24,28,83)]

The AFI–PM transition mechanism has been extensively studied so far. A theoretical study suggested the Mott insulator transition in the π spin site and AF order in the $3d$ spin site.[19)] However, a study of the specific heat in the AFI phase suggests a new concept regarding the AF order state, that is, the AF order mainly exists in the π spin site. In the temperature dependence of specific heat, a broad peak is observed in the AFI phase. The total magnetic entropy reaches $R\ln(6)$, which corresponds to the degrees of freedom of the $3d$ spin. This result strongly suggests that the $3d$ spin system maintains a paramagnetic state in the AFI phase.

In the AFI phase, a large dispersion in the high frequency response[15,29)] and nonlinear current–voltage (I–V) characteristics[47)] are reported. The drastic nonlinear transport characteristics are observed in the I–V curve, revealing a so-called negative resistance effect at an applied electric field or a current density higher than the threshold value. This phenomenology is well explained by a nonlinear equation for a positive feedback system.

After that, the Mössbauer measurements of the ^{57}Fe ions confirmed a fast relaxation state of the $3d$ spins in the AFI phase,[50)] which are consistent with the specific heat measurements. Moreover, recent theoretical studies[49,51)] show that the AF order in the π spins can be induced by paramagnetic $3d$ spins with magnetic anisotropy via $J_{\pi d}$.

Table 3: Crystal data and experimental details[87)]

Material	β"-(BEDT-TTF)$_2$SF$_5$CH$_2$CF$_2$SO$_3$	
Chemical formula	$(C_{10}H_8S_8)_2^+ \cdot (C_2H_2CF_2SO_2)^-$	
Formula weight	1040.45	
Space group	$P\bar{1}$	
Z	2	
R, R_w	0.046, 0.045	
Temp	123 K	298 K
a/Å	9.1536(6)	9.260(2)
b/Å	11.4395(8)	11.635(2)
c/Å	17.4905(12)	17.572(5)
α/deg	94.316(1)	94.69(3)
β/deg	91.129(1)	91.70(1)
γ/deg	102.764(1)	103.10(2)
V/Å^3	1779.9(2)	1835.5(9)

2.2 β"-(BEDT-TTF)$_2$SF$_5$CH$_2$CF$_2$SO$_3$

The organic superconductor β"-(BEDT-TTF)$_2$SF$_5$CH$_2$CF$_2$SO$_3$ (β"-SF$_5$ salt) with the critical temperature $T_c \approx 5$ K, is synthesized by an electrochemical method.[87)] The crystal structure is shown in Fig. 14. The conducting BEDT-TTF cation layers are well separated by the large SF$_5$CH$_2$CF$_2$SO$_3$ anion layers. The crystallographic data of the β"-SF$_5$ salt is shown in Table 3.[87)]

The resistance and magnetization of the β"-SF$_5$ salt were first measured by Geiser et al. They reported that the resistivity shows a semiconducting behavior to a broad maximum temperature of ∼100 K, beyond which it decreases in a metallic fashion.[87)] Below 6 K, the resistance begins to drop to reach zero at 4.4 K. In addition, large diamagnetization is reported, whose onset is at 5.2 K in the best sample.

The electrical band structure of the β"-SF$_5$ salt is calculated by extended Huckel tight-binding calculations, which show that the Fermi surface associates with a 2D hole pocket and a pair of wavy 1D sheets. The 2D Fermi surface occupies 25.4 % of the first Brilluin zone.[87)] Experimentally, the Fermi surface is obtained by de Haas–van Alphen, Shubnikov–de Haas, and angular-dependent magnetoresistance oscillations (AMRO).[89,91)] The SdH oscillation frequencies follow the $1/\cos\theta$ angular dependence expected for a 2D Fermi surface, and the fundamental frequency corresponds to 5 % of the first Brillouin zone. The effective masses are $m_c = 1.9m_e$ and m_b=$3.9m_e/g$.[89)] The interlayer resistance measurements, indicate the no coherent interlayer transport. A perfect quasi 2D electric system is also realized in the β"-SF$_5$

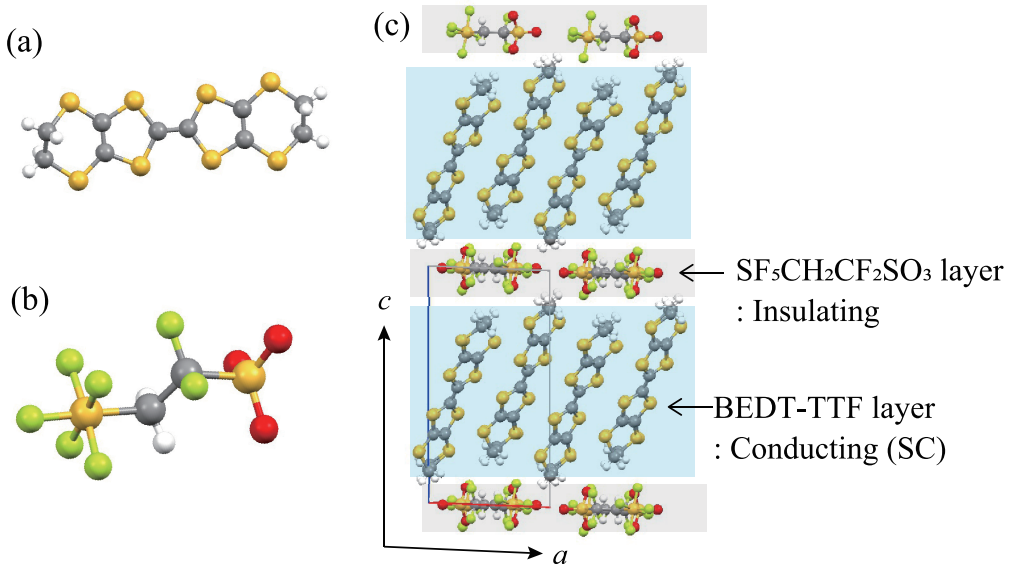

Figure 14: Crystal structures of the β"-SF_5 salt[87)]

salt.[92)]

To characterize the superconductivity, some experiments were performed. In the heat capacity measurements, the specific heat jump at the superconducting transition can be well described by the strong-coupling BCS theory.[90)] In magnetic fields, the critical field H_{c2} strongly depends on the field angle θ, which is the angle between the conducting layer and the magnetic field direction. When the magnetic field is perpendicular to the conducting layers, the superconductivity is strongly suppressed; $H_{c2} \approx 1.2$ T, whereas when the magnetic field is parallel to the conducting layers, it is stabilized up to ~15 T for the best sample; $H_{c2} \approx 15$ T.

In the weak coupling BCS theory, the Pauli paramagnetic limit is $H_{\mathrm{Pauli}} = 1.84T_{\mathrm{c}}$, which sets a strong limit to superconductivity. The value of $H_{c2} \approx 15$ T of the β"-SF_5 salt is shown in Table 3, which is considerably higher than that of the Pauli limit ($H_{\mathrm{Pauli}} \approx 10$ T). Higher H_{c2} will result in large anisotropy; the H_{c2} value rapidly decrease with the tilting of the magnetic field from the conducting layers. Therefore, the FFLO phase is expected to occur in a high magnetic field, which can stabilize the superconductivity above the Pauli limit.

Efforts have been devoted to discover the FFLO phase transition in the β"-SF_5 salt, and the FFLO phase boundary has been reported in the resonance frequency (RF) response (RF change of a tunnel diode oscillator), NMR and heat capacity measurements.[74–76)] In the magnetic field parallel to the conducting layer, the RF response and NMR measurements show two anomalies at low temperatures, which are assigned to H_{c2} and FFLO transition, respectively. In contrast, in the heat capacity measurement, two different anomalies are observed only when the field is slightly tilted from the superconducting layers. These data suggest some phase transition only in the tilted field. In this way, the phase diagram of the β"-SF_5 salt is still controversial.

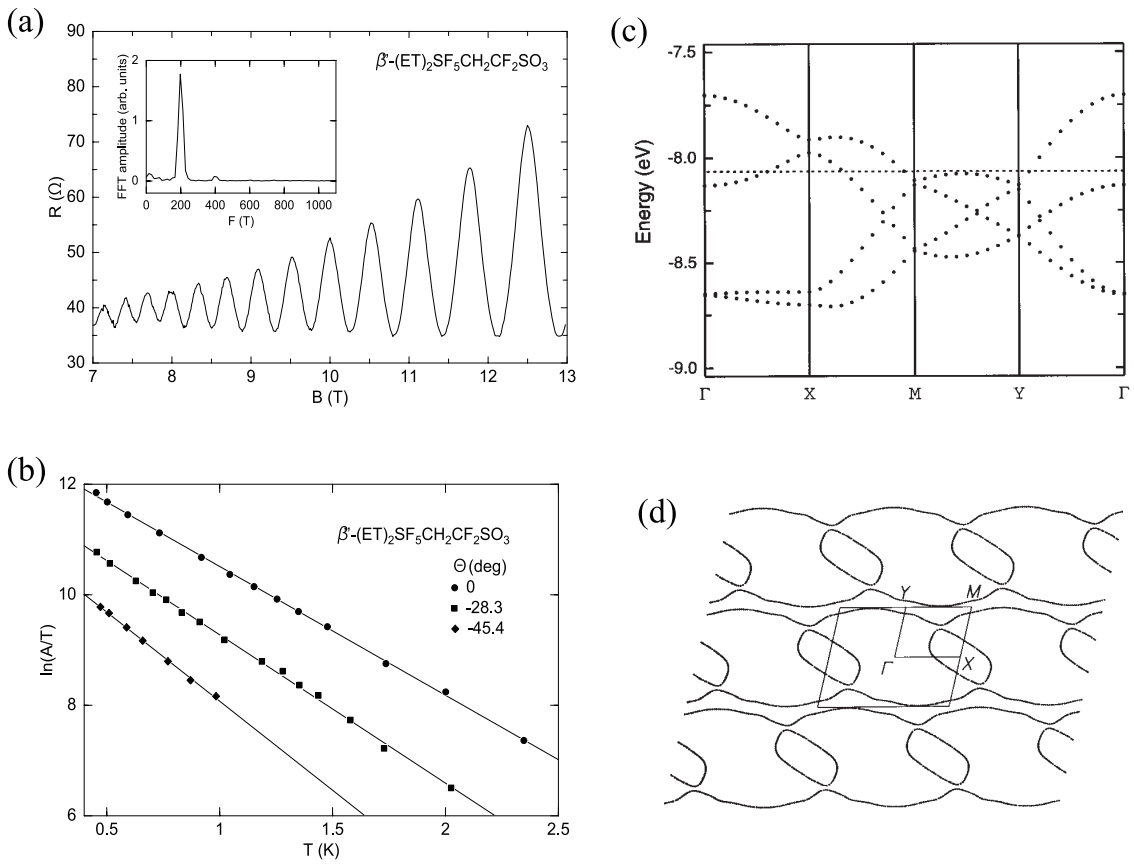

Figure 15: Resistance of the β"-SF_5 salt as a function of applied magnetic field at $\theta = 0°$. The inset shows the Fourier transform of the resistive conductance oscillations. (b) Temperature dependence of the A/T term, where A refers to the SdH amplitude. (c) Dispersion relations of the four highest occupied bands calculated for the β"-SF_5 salt. (d) Fermi surfaces calculated for the β"-SF_5 salt. The closed pockets located at X and its equivalent points are hole surfaces.[89)]

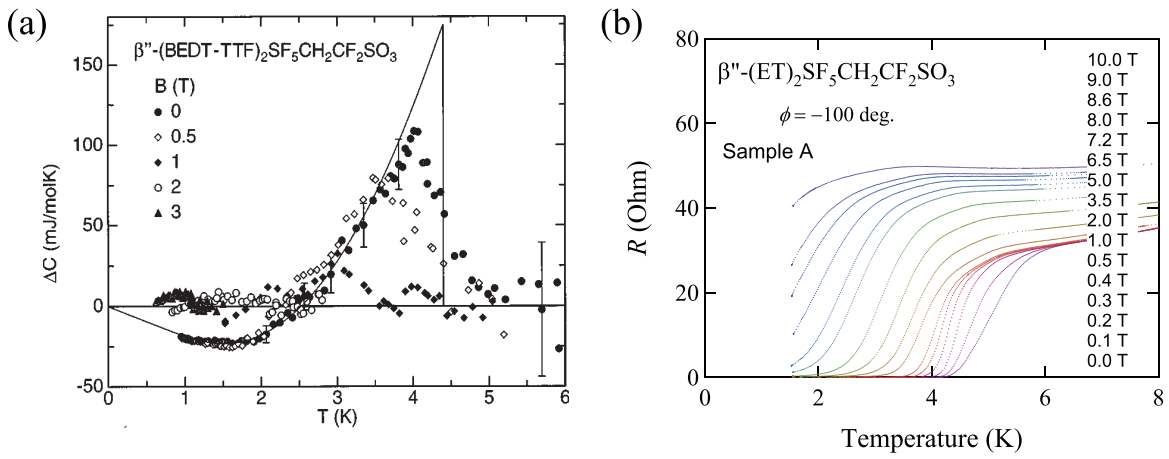

Figure 16: (a) Specific-heat difference ΔC between superconducting and normal C. The solid line is a fit of the $B = 0$ data according to the BCS theory with strong coupling.[90] (b) Interlayer resistance as a function of temperature T for several values of magnetic field.[91]

Table 4: Superconducting parameters in layered organic superconductors

Material	T_c [K]	$\mu_0 H_{c2}$[T]	$\mu_0 H_{c2\parallel}$[T]	$H_{c2\parallel}/H_{c2\perp}$	$\mu_0 H_{FFLO}$[T]	$\mu_0 H_{\rm FFLO}/T_c$[T/K]	CE	Ref.
κ-$(ET)_2Cu(NCS)_2$	9.5–10	7	28–34	4.3	21–23	2.0–2.2	none	*3
λ-$(BETS)_2GaCl_4$	5–5.7	4	12–13	3	9.5–10	1.7–2.0	none	*4
λ-$(BETS)_2FeCl_4$	3–4	-	16*1	-	7*1	1.8–2.1	◯	*5
β"-SF_5	4.7–5.2	1.3	14	11.5	9.5-10	1.9–2.1	*2	*6
β"-Ga	4.8	2.5	21	8.4	15	3.1	◯	

*1: estimated by considering the internal field.[24]

*2: not reported.

*3: 77, 79–81, 101–103)

*4: 84, 86, 99)

*5: 24, 28, 83, 98)

*6: 74, 75)

ET: BEDT-TTF

β"-SF_5: β"-$(ET)_2SF_5CH_2CF_2SO_3$

β"-Ga: β"-$(BEDTTTF)_4[(H_3O)Ga(C_2O_4)_3]C_6H_5NO_2$

CE: commensurability effect

Ref: references

Chapter 3

Purpose

Various physical properties of layered organic conductors have been reported, in which the conducting π electrons of the organic donor molecules that form low-dimensional electric systems play an important role. In particular, it is observed that field-induced phase transitions occur in the magnetic field, which are caused by characteristic structures and interactions in the layered structure. For this dissertation, two material systems were chosen and measured systematically. One is a salt of the π–d system, λ-$(BETS)_2FeCl_4$. In the π–d system, an interplay between magnetism and electronic conduction causes AF order and field-induced superconducting transition in the magnetic field. The other system is a layered organic superconductor, β"-$(BEDT\text{-}TTF)_2SF_5CH_2CF_2SO_3$ (β"-SF_5 salt), for which the presence of the FFLO phase has been indicated in high magnetic fields at low temperatures.

(1) Conduction and magnetic properties in the organic π–d system λ-$(BETS)_2FeCl_4$

In the π–d systems, some interesting phenomena have been observed at low temperatures: e.g., M–I transition, AF order, and superconducting transition. Among various π–d systems, λ-$(BETS)_2FeCl_4$ gained considerable interest and has been extensively studied because of its unique magnetic field–temperature phase diagram, which shows AF insulating, metal, and field induced superconducting phases with increasing magnetic field at low temperatures.

In λ-$(BETS)_2FeCl_4$, some anomalous phenomena have been observed by various experiments in a wide range of temperature and field. In particular, in this system, the mechanism of the AFI–PM transition at a low temperature is a long-standing central issue. To provide an important insight into the AFI phase, we measured the resistance, I–V characteristics, magnetic torque, and magnetocaloric effect (MCE). Comparisons of a non-magnetic salt and other π–d systems, the strong π–d interaction makes complicated spin structures, which should cause all of the anomalies.

(2) Novel superconducting phase in the layered organic conductor

β"-$(BEDT\text{-}TTF)_2SF_5CH_2CF_2SO_3$

In general, the superconducting Cooper pairs are broken by the Zeeman effect, which gives the Pauli paramagnetic limit H_{Pauli}. However, when the superconductivity is in the clean limit and the orbital effect is strongly quenched, the Cooper pairs can survive at superconductivity even above H_{Pauli}, which results in the so-called FFLO phase. The FFLO phase has been extensively researched. However, vortex phase transitions give rise to considerable ambiguity in the interpretation of the experimental data.

To observe the FFLO phase transition distinct from vortex melting transitions, we measured the magnetic torque, MCE, and resistance in the β"-SF_5 salt. Because of its highly 2D superconductivity, the β"-SF_5 salt is the best candidate for the FFLO phase studies.

Part II

Experimental technique

Chapter 1

Fermi surface measurements

The resistance of the metal strongly depends on the Fermi surface topology. In the strong magnetic field limit satisfying $\omega_c\tau \gg 1$, where ω_c is a cyclotron frequency and τ is a relaxation time, the magnetoresistance saturates or diverges is determined by whether a closed or open orbit. When the Fermi surface is closed, a quantum oscillation is observed, in which the magnetoresistance oscillates as a function of the magnetic field due to Landau quantization.

Conducting electrons form the Fermi surface, whose structure contributes to the physical properties of metals such as electrical and magnetic properties. Therefore, it is important to clarify the structure of the Fermi surface, and for this purpose, angular-dependent magnetoresistance oscillations (AMRO) and quantum oscillations are powerful tools.

1.1 Angular-dependent magnetoresistance oscillation (AMRO)

When the sample has a layered structure in the $x-y$ plane, an electron has a two-dimensional Fermi surface with a cylindrical structure extending in the k_z direction. This Fermi surface shape corresponds to the energy dispersion expressed as

$$E = \frac{\hbar^2}{m_{\mathrm{eff}}}\left(k_x^2 + k_y^2\right) - 2t\cos\left(ck_z\right). \tag{14}$$

Here, it is assumed that electrons [effective mass m_{eff}, wavenumber (k_x, k_y, k_z)] behave as free electrons in a two-dimensional plane, a transfer integral exists between conducting planes t, and the distance between conducting layers is c. Assuming that t is smaller than the Fermi energy, the conductivity in the z direction using the linearized Boltzmann transport equation can be written as

$$\sigma_{zz}\left(\theta\right) = \sigma_{zz}^0\left[J_0^2\left(ck_{\mathrm{F}}\tan\theta\right) + \sum_{m=1}^{\infty}\frac{2J_m^2\left(ck_{\mathrm{F}}\tan\theta\right)}{1+\left(\omega_c\tau\nu\cos\theta\right)^2}\right], \tag{15}$$

$$\sigma_{zz}^0 = \frac{2e^2 m_{\mathrm{eff}} t^2\tau}{\pi\hbar^4}\ , \quad \omega_c = \frac{eH}{m_{\mathrm{eff}}}. \tag{16}$$

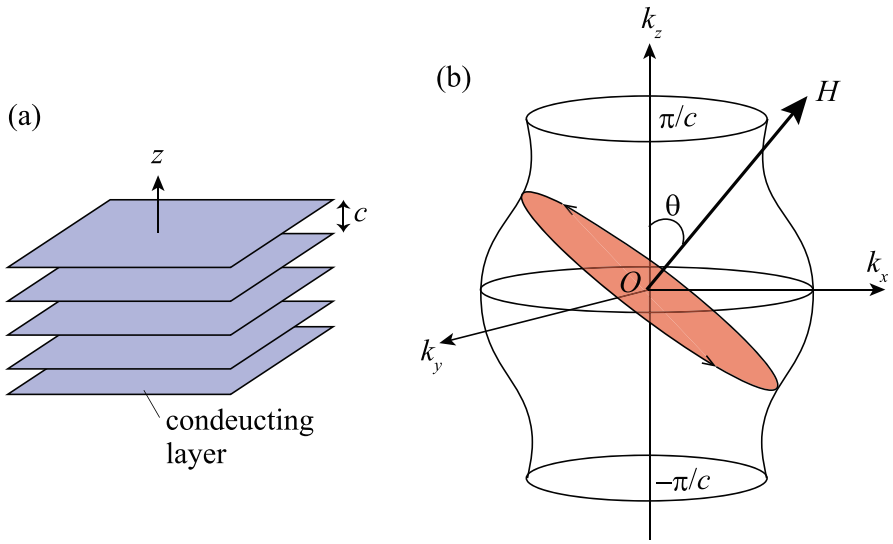

Figure 17: Schematic illustration of (a) a layered structure and (b) a 2D Fermi surface.

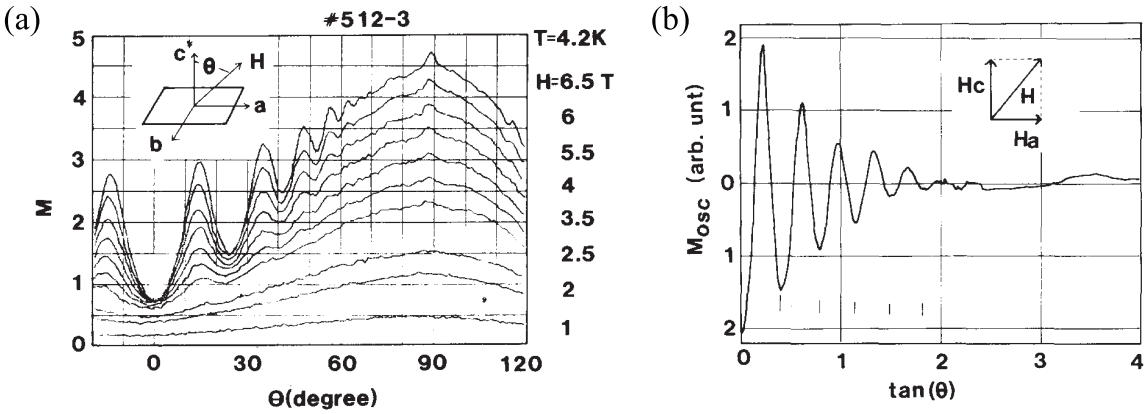

Figure 18: Magnetoresistance of θ-(BEDT-TTF)$_2$I$_3$[100)]

J_n is the Bessel function of order n, k_{F} is the Fermi wavenumber, and e is the elementary charge. When $\omega_c\tau \gg 1$, the first term of the equation greatly contributes because the second term approaches zero. When z is greater than 1, the zero order Bessel function approaches

$$J_0 = \sqrt{\frac{2}{\pi z}} \cos\left(z - \frac{\pi}{4}\right). \tag{17}$$

If the magnetic field angle θ satisfies the equation

$$ck_{\mathrm{F}} \tan\theta = \pi\left(n - 1/4\right), \tag{18}$$

the conductivity in the z direction is zero and the resistance diverges. The experimental, result of resistance show a sharp peak due to the influence of the Bessel function of the first or higher order, which is a periodic peak when plotted with $\tan\theta$. This is called AMRO, and the Fermi wavenumber is obtained from the oscillating period.

1.2 Quantum oscillation

When conducting electrons have a closed Fermi surface, in the magnetic field, they show a cyclotron motion in a plane perpendicular to the field. Since the Lorentz force is always perpendicular to both the velocity vector of the electron and the magnetic field, energy is not received by the interaction with the magnetic field and is always constant. This implies that electrons always move in the constant-energy surface in k-space, and they move on the Fermi surface unless scattered. A quantum mechanical, the energy level of electrons moving in the cyclotron orbit is quantized and is

$$E_n = \hbar\omega_c\left(n + \frac{1}{2}\right) + \frac{\hbar^2 k_z^2}{2m}\ , \quad n = 0,\ 1,\ 2,\ 3\ldots, \tag{19}$$

when the magnetic field is in the z direction. As the magnetic field increases, each Landau level rises and crosses the Fermi level in a certain magnetic field. Since electrons transfer between the Landau levels, the energy of the electron system periodically changes with increasing magnetic field. Because of this periodic change, quantum oscillations are observed in various state quantities such as density of state, magnetization, and specific heat. The quantum oscillations observed in magnetization and resistance measurements are called de Haas–van Alphen and Shubnikov–de Haas oscillations, respectively.

In the free electron approximation, the quantum oscillation component of magnetization can be written as

$$M_{\parallel} \propto V\left(\frac{H}{F}\right)^{1/2} \sum_{p=1}^{\infty} \frac{1}{p^{3/2}} R_{\mathrm{T}} R_{\mathrm{D}} R_{\mathrm{S}} \sin\left[2\pi p\left(\frac{F}{H} - \frac{1}{2}\right) + \Phi\right]. \tag{20}$$

Here, V is the volume of the sample and R_T, R_D, and R_S are the attenuation factors of the quantum oscillation. F of the oscillation term is the frequency of the quantum oscillation, which is written as

$$F = \frac{\hbar}{2\pi e} A_{\mathrm{F}}, \tag{21}$$

where A_{F} is the cross-sectional area of the Fermi surface. From this relationship, the cross-sectional area of the Fermi surface can be determined directly from the frequency of quantum oscillations. Therefore, we can determine the 3D structure of the Fermi surface by observing the quantum oscillations in various magnetic field angles. Equation (20) also indicates that the interval of the oscillations is inversely proportional to the magnetic field intensity. The phase factor Φ in Eq. (20) takes the values $+\pi/4$ and $-\pi/4$ at the maximum and minimum cross-sectional areas of the Fermi surface, respectively.

The oscillation component of the density of state $D(H)$ is written as

$$D\left(H\right) \propto V\left(\frac{H}{F}\right)^{1/2} \sum_{p=1}^{\infty} \frac{1}{p^{1/2}} R_{\mathrm{T}} R_{\mathrm{D}} R_{\mathrm{S}} \cos\left[2\pi p\left(\frac{F}{H}-\frac{1}{2}\right)+\Phi\right], \tag{22}$$

and conductivity is written as

$$\sigma = \sigma_0\left(H\right)\left(1+\frac{D(H)}{D_0}\right). \tag{23}$$

Here, $\sigma_0\left(H\right)$ and D_0 are non-oscillatory components of the conductivity and the density of state, respectively.

Chapter 2

Refrigerator and Probe

2.1 Helium refrigerator

For this study, Oxford 20 T and 17 T superconducting magnets were used. The 17 T superconducting magnet system combined with a ^{4}He cryostat can cool the sample space down to 1.5 K.

The 17 T superconducting magnet with the ^{4}He system can additionally install a ^{3}He cryostat. Fig. 20 shows the operating principle of the ^{3}He cryostat. The ^{3}He gas is liquefied by the helium outside the jacket. Sample space is cooled down to ∼0.5 K by using an external pump.

2.2 Dilution refrigerator

The 20 T superconducting magnet system is combined with a ^{3}He dilution refrigerator, which can continuously cool the sample to ∼30 mK.

Figure 21 shows the schematic diagram of the refrigerator. First, the ^{3}He-^{4}He mixture gas is condensed by the condenser placed in the 1 K pot. The ^{4}He liquid passes continuously through the bath into the 1K pot via a needle valve, and here it is pumped and cooled to ∼1.5 K. The mixture flows through the condenser and the still chamber, where it is condensed and cooled. Next, the mixture flows past the cold plate, where more heat is transferred from the mixture, until the mixture ends up in the mixing chamber.

In the mixing chamber, the ^{3}He–^{4}He mixture separates into two phases, the ^{3}He-rich and ^{4}He-rich phases. In the ^{3}He-rich phase, which is located the upper phase, the ^{3}He concentration is almost 100%. On the other hand, the ^{4}He rich phase, which is located the lower phase, ^{3}He is diluted to ∼6.6%. The ^{3}He dilute phase is pumped into the still and the ^{3}He liquid in the concentrated phase is transferred into the dilute phase. The system then gains entropy and is cooled 20–30 mK.

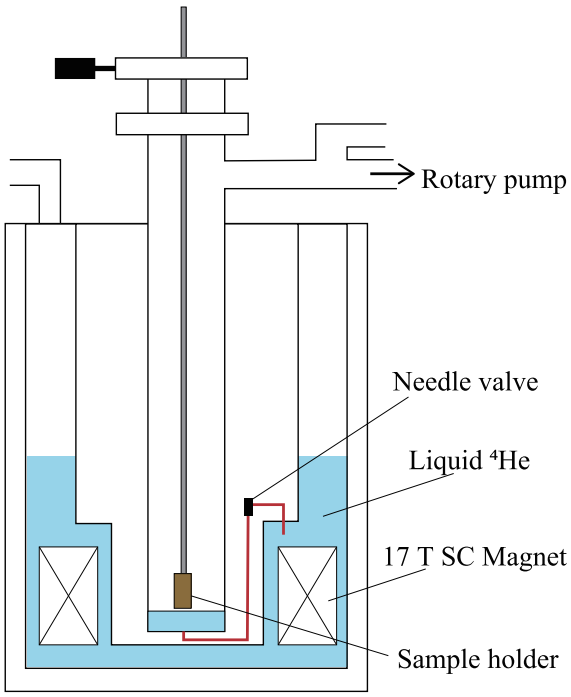

Figure 19: Schematic illustration of the variable-temperature insert cryostat.

2.3 Probes

The magnetic field angle is precisely controlled by the stepping motor controller with a one-axis rotation probe for dilution refrigerator and one- and two-axis rotation probes for ^{4}He and ^{3}He cryostats, respectively. The sample can be rotated in the field with a resolution of $\sim 0.1°$.

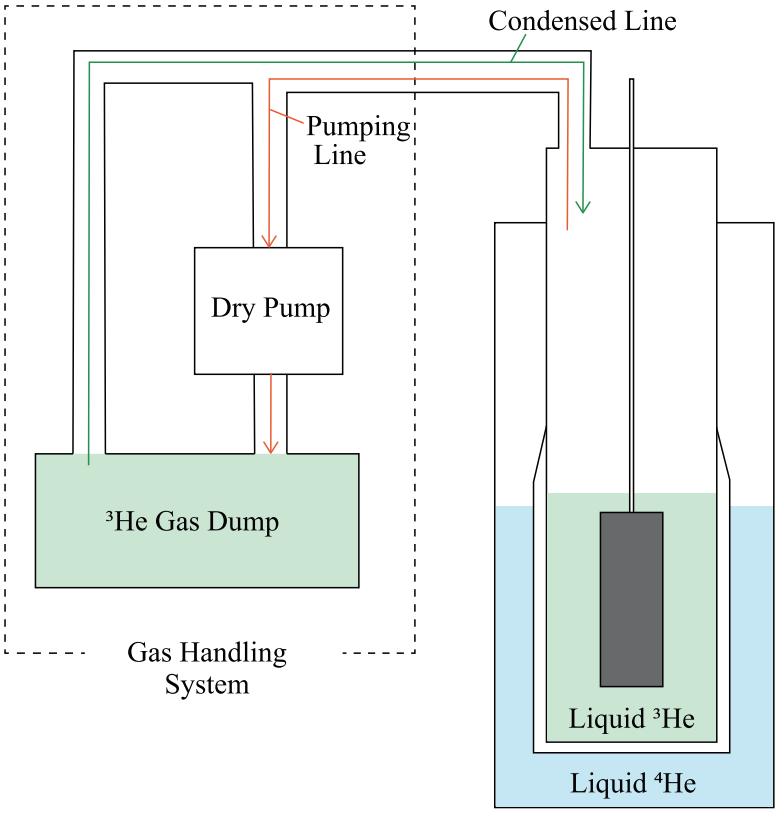

Figure 20: Schematic illustration of the ^{3}He cryostat.

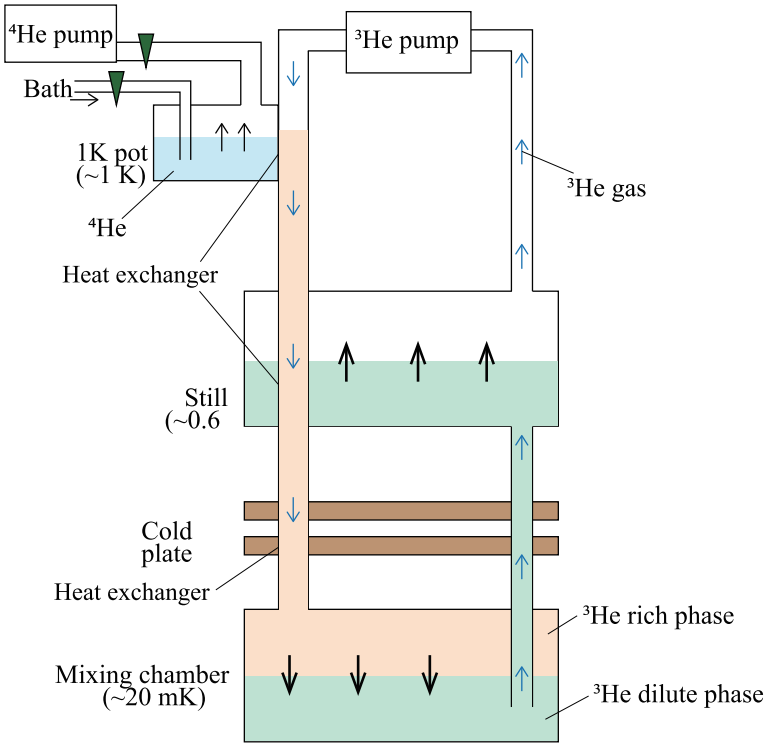

Figure 21: Schematic illustration of the ^{3}He dilution refrigerator.

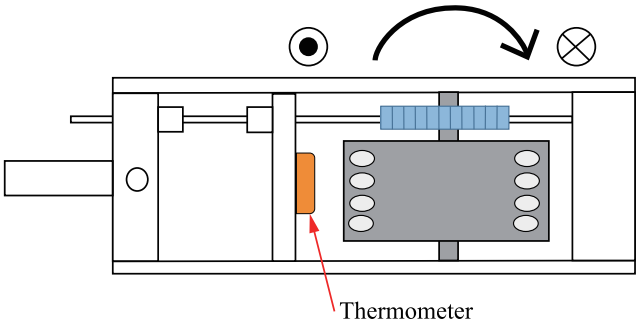

Figure 22: Schematic illustration of the one-axis rotation probe.

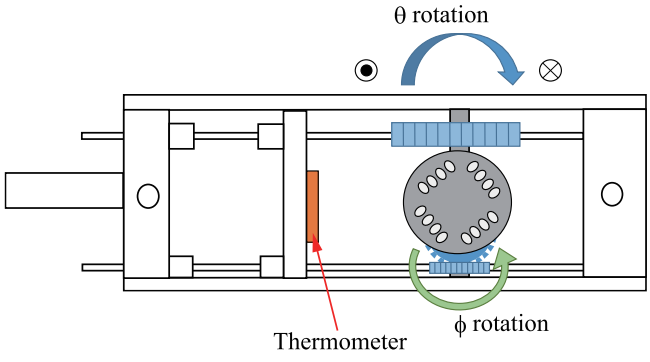

Figure 23: Schematic illustration of the two-axis rotation probe.

Chapter 3

Experimental details

3.1 Resistance and dielectric constant

In general, it is well known that current J is proportional to voltage E, which is called Ohm's law:

$$J = E/\rho, \tag{24}$$

where ρ is the resistivity of the sample. In Ohm's law, the resistivity is independent of the current. However, in the condensed, density wave, superconducting, and charge-ordering states, nonlinear current–voltage (I–V) characteristics are observed, where the resistivity depends on the current, $\rho(J)$. Such nonlinear I–V characteristics in organic conductors provide information on the electronic state of a collective motion in a density-wave state, neutral–ionic transition in charge transfer salts, and melting of a charge-aligned state.

Assuming a parallel plate capacitor having an area S and a distance d with a uniform electric field applied between the plates, a charge density between the electrode plates $\pm\sigma_f$ is given by

$$D = \varepsilon_0 E, \tag{25}$$

where ε_0 is the dielectric constant of vacuum, $|D| = \sigma_f$, and the electromotive force

$$E = \sigma_f/\varepsilon_0. \tag{26}$$

The total amount of the true charge on the electrode plate Q and the potential difference between the electrode plates V are given by

$$Q = \sigma_f S \tag{27}$$

and

$$V = Ed = \frac{\sigma_f}{\varepsilon_0}, \tag{28}$$

respectively. Therefore, the capacitance of the capacitor is defined as

$$C = \frac{Q}{V} = \frac{\varepsilon_0 S}{d}. \tag{29}$$

When the dielectric is inserted between the parallel plates, D is rewritten as

$$D = \varepsilon_0 E + P, \tag{30}$$

where P is a polarization vector. Using an electrical susceptibility χ, $P = \chi\varepsilon_0 E$. Thus,

$$D = \varepsilon_0 E + \chi\varepsilon_0 E = \varepsilon_0 (1 + \chi) E \equiv \varepsilon_0\varepsilon_1 E \ , \ \varepsilon_1 \ = 1 + \chi. \tag{31}$$

The capacitance of the capacitor is written as

$$C = \frac{Q}{V} = \frac{\varepsilon_0\varepsilon_1 S}{d}. \tag{32}$$

The I–V characteristics and resistivity were measured by a four-terminal method. In the AFI phase, the resistance increases to 10^8 Ω. Therefore, special care should be taken to measure the resistance. In the high-resistance region, the DC current was applied using a source meter (Keithley 2400) and the sample voltage was detected by an electrometer (Keithley 6514) whose internal impedance ($> 2 \times 10^{11}$ Ω) is much higher than that of the sample resistance. In the low-resistance region, the AC current was applied using a lock-in amplifier (Stanford Research Systems SR830). For both AC and DC measurements, the currents were applied along the a'–c conducting plane. It was ensured that both AC and DC measurements for the same samples give the same resistance values in the intermediate resistance region.

The dielectric constants were measured by a two-terminal method using a lock-in amplifier at 1 Hz–2 kHz. . Gold wires of 10 μm diameter were attached to crystals with carbon paste. Coaxial cables were used to reduce the stray capacitance of the experimental setup. The electrical contacts were made using carbon paste on the sides of the crystals. The AC voltage was kept at a low value of ∼0.1 V.

3.2 Magnetic torque

The sample has two typical directions in the magnetic field, namely, the easy and the hard axes, where the sample is easy and hard to magnetize, respectively. The difference of electron energies between the field parallel to the easy and hard axes is defined as the magnetic anisotropy. This magnetic anisotropy generally arises from the crystal magnetic anisotropy, dipole interaction, and spin–orbit coupling.

When the magnetic field is parallel to the easy/hard axis, the anisotropy energy is minimum/maximum. When the magnetic field is not parallel to the easy/hard axis, a magnetic torque is induced on the sample, which is a force that rotates the sample in the magnetic field.

In the case of the PM phase, the magnetic anisotropy arises from the anisotropy of the magnetic susceptibility. Magnetization M in a field H is given by $M = \chi H$, where χ is the 3×3 magnetic susceptibility tensor having diagonal elements. The magnetization vector can be written as

$$\begin{pmatrix} M_x \\ M_y \\ M_z \end{pmatrix} = \begin{pmatrix} \chi_x & 0 & 0 \\ 0 & \chi_y & 0 \\ 0 & 0 & \chi_z \end{pmatrix} \begin{pmatrix} H_x \\ H_y \\ H_z \end{pmatrix}. \tag{33}$$

As the magnetic susceptibility in a paramagnetic phase is independent of the magnetic field, the magnetic anisotropy energy is written as

$$E_M = \int_0^M H dM = \frac{1}{2} H \chi H = \frac{1}{2} H M \ . \tag{34}$$

The magnetic torque is given by

$$\tau_m = -\frac{\partial F}{\partial \theta} = \int \frac{\partial M}{\partial \theta} dH = \frac{1}{2} \left(\chi_x - \chi_y \right) H^2 \sin 2\theta \ , \tag{35}$$

where F is the free energy. From the above equation, it is clear that the magnetic torque in the PM phase has a periodicity of 180°.

In the AF phase, the magnetization is considered to be the sum of two sublattice magnetizations. In the zero magnetic field, spins are of AF order and the magnetization is parallel to the spin axis, where the magnetic anisotropy energy is minimum. In the magnetic field, the direction of magnetization is determined by the anisotropy of the free energy, given by the sum of the exchange energy, Zeeman energy, and anisotropic energy.

When the sample has uniaxial anisotropy, in the magnetic field parallel to the easy axis, there is a critical field in the AF phase called spin-flop transition field H_{SF}. The spin direction is suddenly changed from parallel to perpendicular to the field at H_{SF}. (Fig. 24) With increasing magnetic field, the magnetization shows a sudden increase at H_{SF}, and above H_{SF}, it increases monotonically. (Fig. 24) The ratio of H and H_{SF} changes the angular and magnetic field dependences of the magnetic torque in the AF phase.

The magnetic torque was measured by a piezoresistive microcantilever technique.[97] The piezocantilever chip used here is composed of an atomic force microscope cantilever, where a sample is mounted, and a reference lever. This monolithic construction can cancel out the magnetoresistance of the piezoresistance in fields by using a bridge circuit. (Fig. 25) The single crystal was attached to the cantilever with silicone grease. The signal was detected by a lock-in amplifier (Stanford Research Systems SR830).

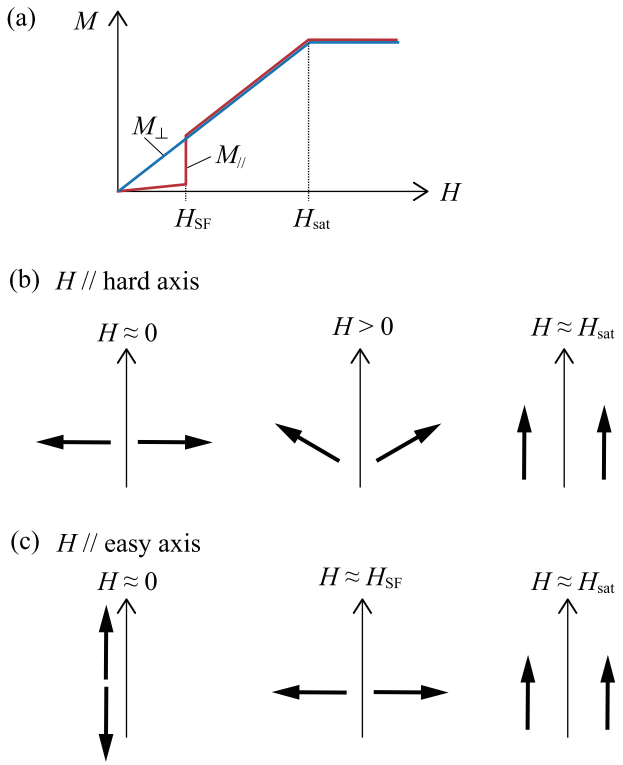

Figure 24: (a) Schematic illustration of magnetization curves of an antiferromagnetic system. H_{SF} and H_{sat} are the spin-flop transition and the saturation field, respectively. (b) and (c) show the schematics of the spins when the field is parallel to the magnetic hard and easy axis, respectively.

3.3 Magnetocaloric effect

Thermal measurements are the most powerful tool to investigate phase transitions and to obtain the entropies of systems. The magnetocaloric effect (MCE) measurement is valuable to investigate the thermal properties of the sample in the magnetic field.

From the definition of entropy S, the difference of the heat dQ is written as

$$dQ = TdS \ . \tag{36}$$

By assuming temperature T and magnetic field H to be independent parameters for the system, the entropy can be expressed as functions of T and H; $S = (T, H)$. This gives a total differential of

$$dS\,(T,H) = \left(\frac{\partial S}{\partial T}\right)_H dT + \left(\frac{\partial S}{\partial H}\right)_T dH. \tag{37}$$

Therefore, dQ can be rewritten as

$$dQ = T\left(\frac{\partial S}{\partial T}\right)_H dT + T\left(\frac{\partial S}{\partial H}\right)_T dH. \tag{38}$$

A temperature difference between the sample temperature T_{s} and the reference temperature T_{r} is defined as

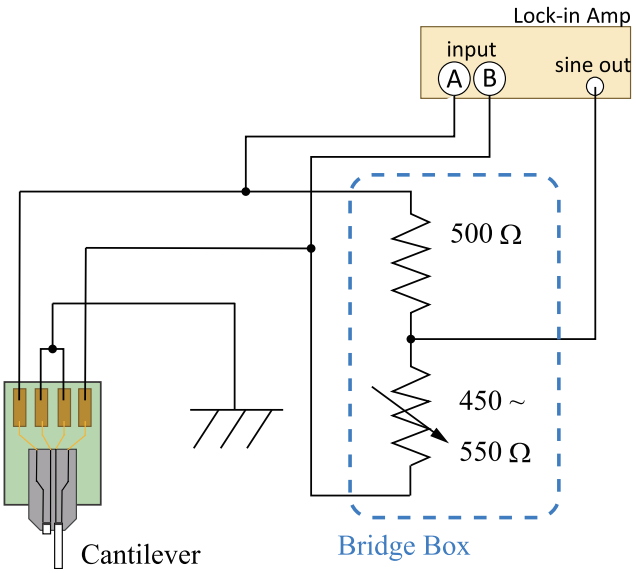

Figure 25: Schematic of the bridge circuit for torque measurements.

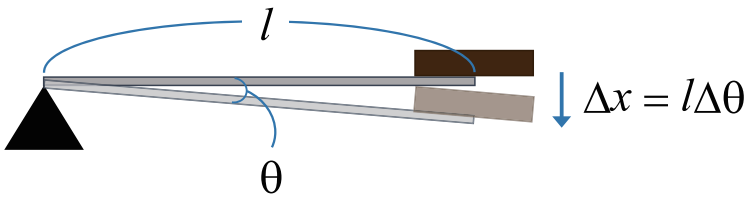

Figure 26: Schematic of a cantilever.

$$\Delta T = T_{\mathrm{s}} - T_{\mathrm{r}} \ . \tag{39}$$

The product of ΔT and thermal conductivity κ is equal to the amount of heat transferred per unit time P,

$$-\kappa \Delta T = P = \frac{dQ}{dt} \ . \tag{40}$$

Hence, the MCE (ΔT) is written as

$$\Delta T = -\tau \frac{d\,(\Delta T)}{dt} - \frac{T}{\kappa} \left(\frac{\partial S_m}{\partial H} \right)_T \frac{dH}{dt} + \delta T \ . \tag{41}$$

The first term shows thermal relaxation with a time constant $\tau = C/\kappa$, where C and κ are the heat capacity of the sample and addenda and the thermal conductance between the sample and heat bath, respectively. In the second term, S_m is the magnetic entropy of the sample. The

third term shows additional heating due to the latent heat and supercooling (or superheating) effect at the first order phase transition or some other effects.

As seen in Eq. (41), the MCE arises from the entropy change $(\partial S_m/\partial H)_T$, which implies that the MCE is highly sensitive to the entropy change in the magnetic field.

The MCE is measured by using a handmade semi-adiabatic cell with thermometers (Fig. 27).[54] Two thermometers (Lakeshore Cernox bare chips) are weakly thermally connected to the heat bath by thin Pt(W) wires of $\sim$10 μm. A single crystalline sample is attached to a thermometer (T_s) by the Apiezon N grease. The other thermometer is used as a reference (T_r).

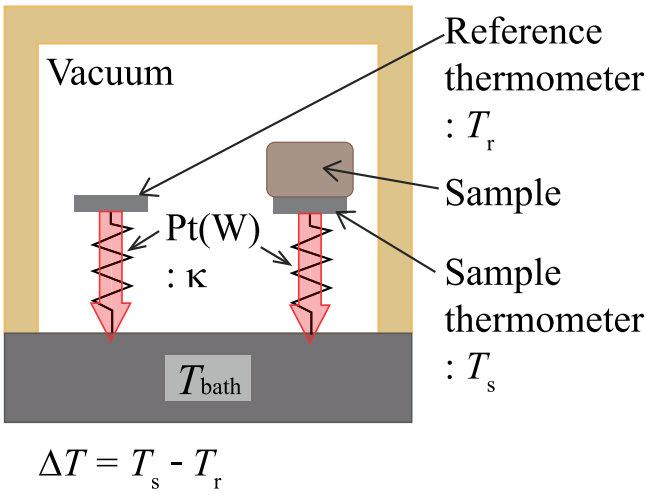

Figure 27: Schematic illustration of the vacuum cell for the MCE measurements.

Part III

Transport and Magnetic properties in the π–d organic conductor λ-$(BETS)_2FeCl_4$

Chapter 1

Experimental results

1.1 Transport property

1.1.1 Temperature and field dependences of resistance

The temperature dependence of the in-plane resistance at a low-bias voltage for sample #1 is shown in Fig. 28. In the measurements, a low voltage is maintained to achieve nearly linear I–V characteristics. The broad peak at ∼100 K and the observation of the M–I transition ($T_{\rm MI}$ = 8.5 K) are consistent with previous studies.[7)]

In the AFI phase, the resistance exponentially increases with decreasing temperature. In the Arrhenius plot (inset), we note that the linear behavior $R = R_0 \exp(\Delta/2k_{\rm B}T)$ is seen only in a limited region, as shown by the dotted lines. The result shows that Δ is temperature dependent in a wide temperature range from $T_{\rm MI}$ to ∼3 K. This behavior is in sharp contrast to conventional charge order or Mott insulating phases, in which $\Delta(T)$ becomes almost constant for $T/T_{\rm MI} < 0.7$.[33–37)] The magnetic field dependences of the in-plane resistance at 1.6 and 7 K, with the magnetic field applied along the c-axis, are shown in Fig. 29. The resistance monotonically decreases with increasing magnetic field and then shows a rapid decrease at the M–I transition. The M–I transition is associated with a hysteresis. The transition field $H_{\rm MI}$ depends on the field angle; the $H_{\rm MI}$ value for $H \parallel b^*$ is higher than that for $H \parallel c$.

The $R(H)$ curves were measured at various field directions and the anisotropy of $H_{\rm MI}$ was obtained (Fig. 30). Here, we define $H_{\rm MI}$ at the criterion R = 4 Ω , which corresponds to approximately ten times the R value in the PM phase. Because of the hysteresis of the transition, $H_{\rm MI}$ values are obtained from up- and down-sweeps at each angle. Note that the $H_{\rm MI}$ values are slightly sample-dependent, e.g., $H_{\rm MI}$ of #3 for $H \parallel b^*$ is smaller than that of #4.

Figure 31 shows the resistance at low fields for H in the b^*–c plane. We successfully observed a small dip at ∼1.2 T for $\theta = 55°$, which is associated with hysteresis. As the field is tilted from this angle, the dip is suppressed and no dip is evident at $\theta = 90°$. Since the magnetic torque measurements show that the spin-flop transition occurs at 1.2 T for $\theta \approx 55°$,[53,55)] the

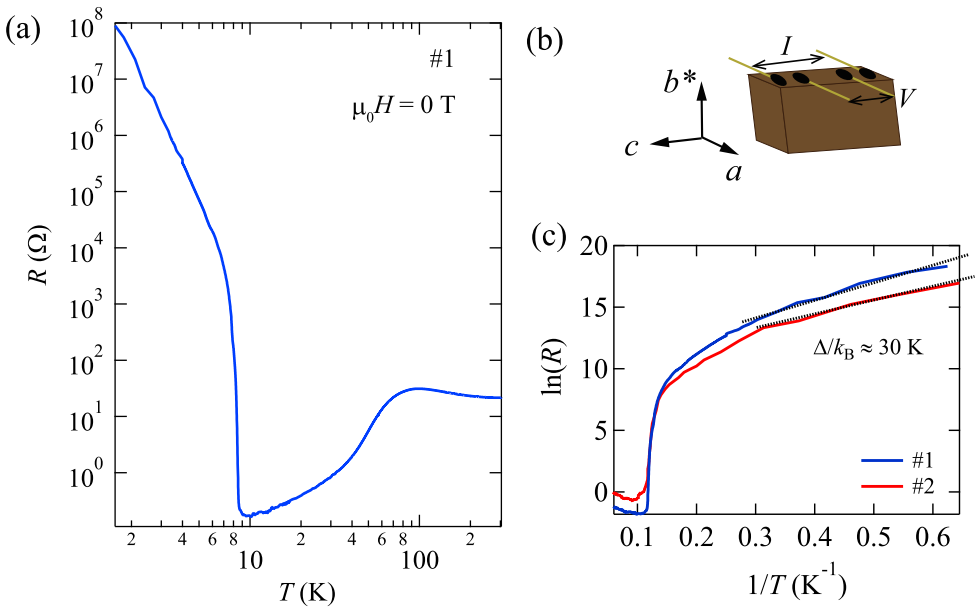

Figure 28: (a) Temperature dependence of the in-plane resistance R at a low bias voltage for λ-(BETS)$_2$FeCl$_4$. (c) Arrhenius plot. The dotted lines show $\Delta/k_B \approx 30$ K.

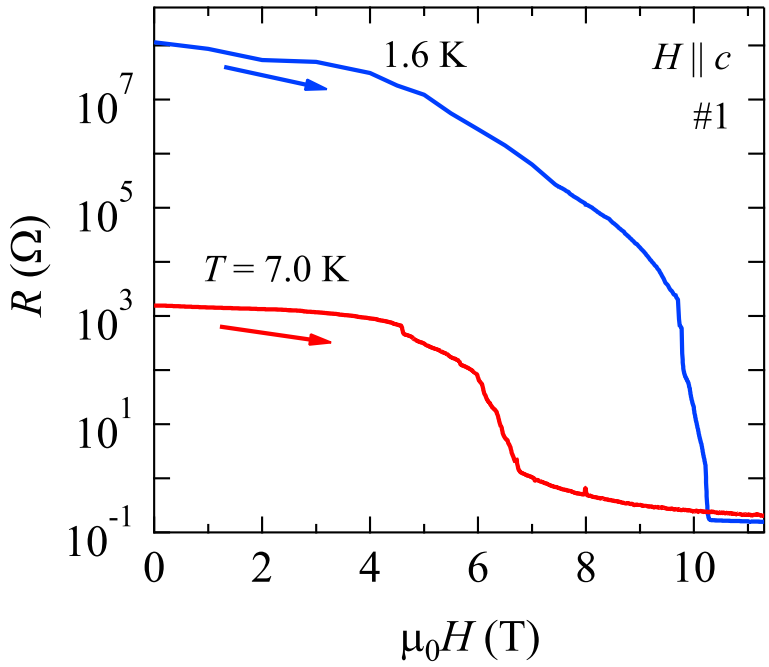

Figure 29: Magnetic field dependence of the in-plane resistance in the whole field region for λ-(BETS)$_2$FeCl$_4$.

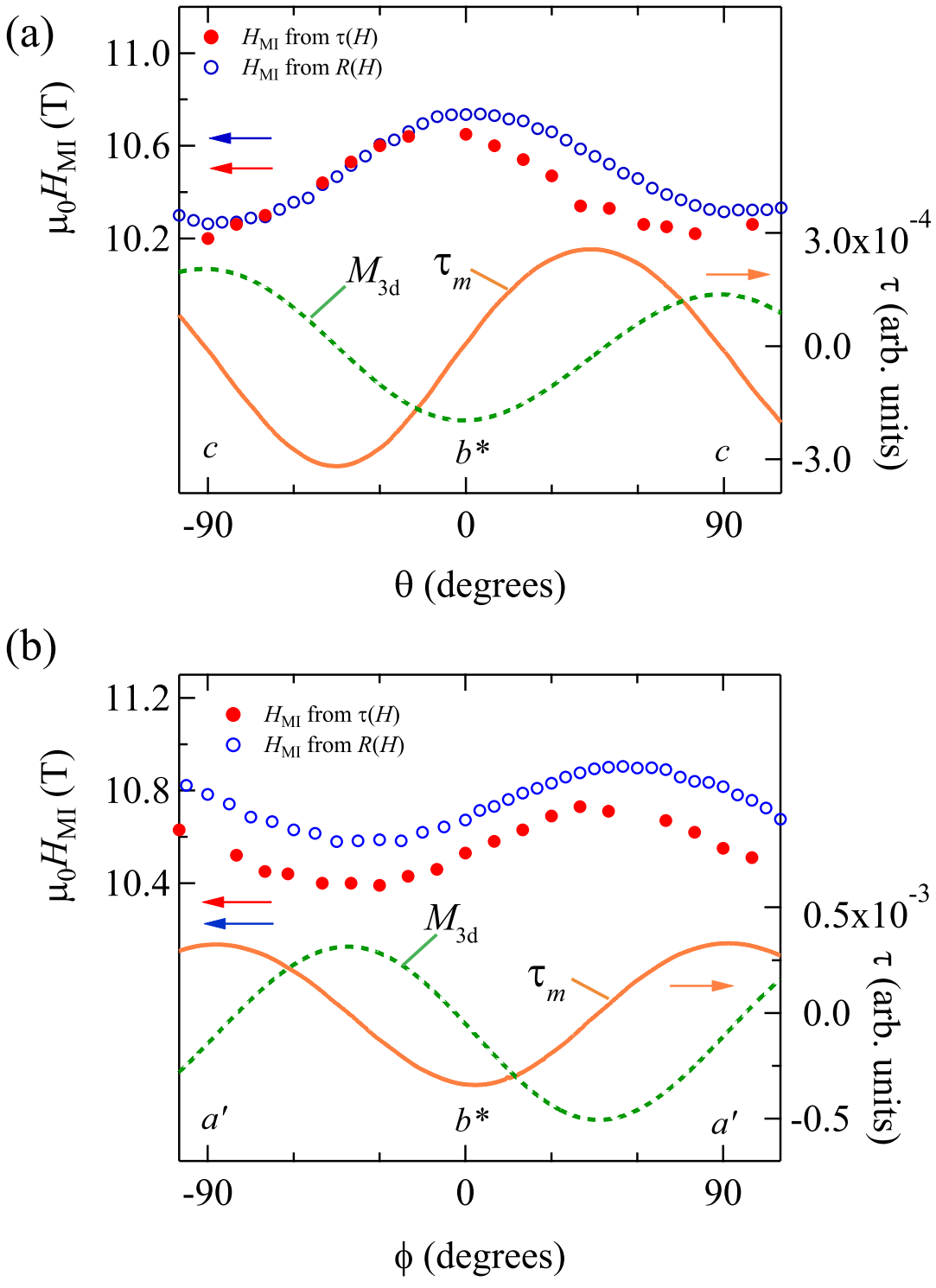

Figure 30: Angular dependence of H_{MI} of λ-$(BETS)_2FeCl_4$ for H in (a) b^*–c and (b) a'–b^* planes.

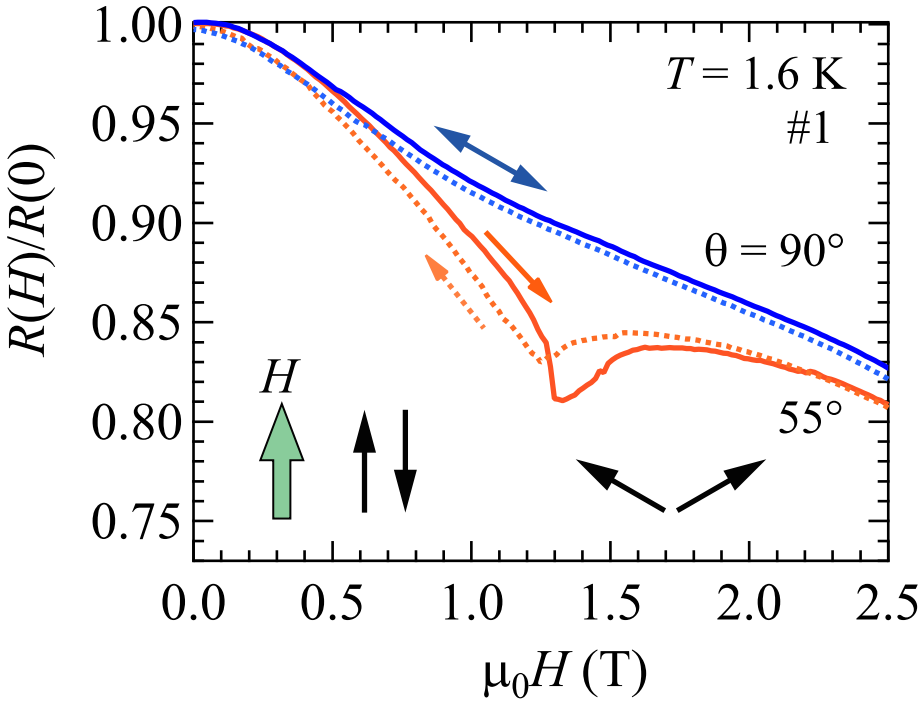

Figure 31: Magnetic field dependence of the normalized resistance at 1.6 K.

small dip can be ascribed to the spin-flop transition.

1.1.2 I–V characteristics

The I–V characteristics at different temperatures are shown in Fig. 32. At high temperatures above 4.4 K, the I–V characteristics are linear in the whole voltage region. At lower temperatures, the I–V characteristics are almost linear up to ∼0.2 V and then show slightly upward curvature at higher voltages. At 1.6 K, for instance, we see the power-law behavior $I = V^{\alpha}$ for $V > 0.3$ V. The exponent α at high voltages increases from 1 to ∼3 with decreasing temperature. The I–V characteristics in magnetic fields at 1.6 K are shown in Fig. 33.

In low magnetic fields of up to ∼6 T, the I–V characteristics are almost linear up to ∼0.2 V and then show upward curvature at higher voltages. The power-law behavior is seen above ∼0.3 V. Above ∼7 T, the I–V characteristics are linear in the whole voltage region. The nonlinear I–V characteristics for λ-$(BETS)_2FeCl_4$ were first reported by Toyota *et al.*[47] They measured the I–V curves up to $E = 100$ V/cm at 4.2 K, which is ∼30 times that in our case, and found negative differential resistance behavior. In the low-electric-field region, power-law-like behavior is seen. The negative differential resistance was discussed in terms of carrier decondensation, although the microscopic origin is an open question. Measurements at higher voltages were also attempted but kinks were found in the I–V curves, showing contact damage. At such high voltages, hysteresis was often observed in the I–V curves, suggesting that the Joule heating of

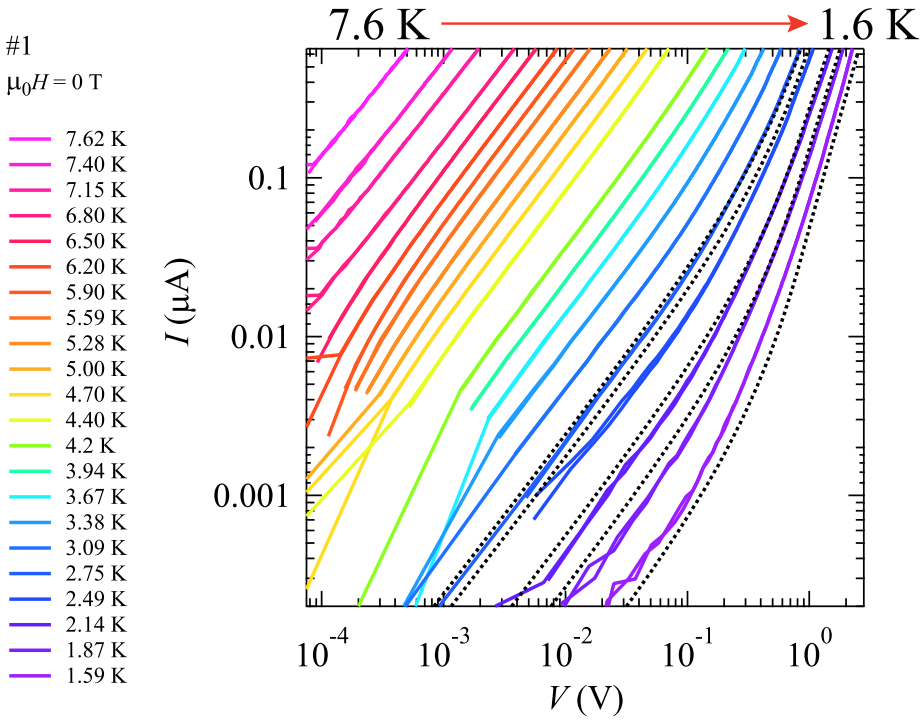

Figure 32: I–V characteristics at various temperatures. The dotted curves show the calculated results for 1.6 K $\leq T \leq$ 2.7 K.

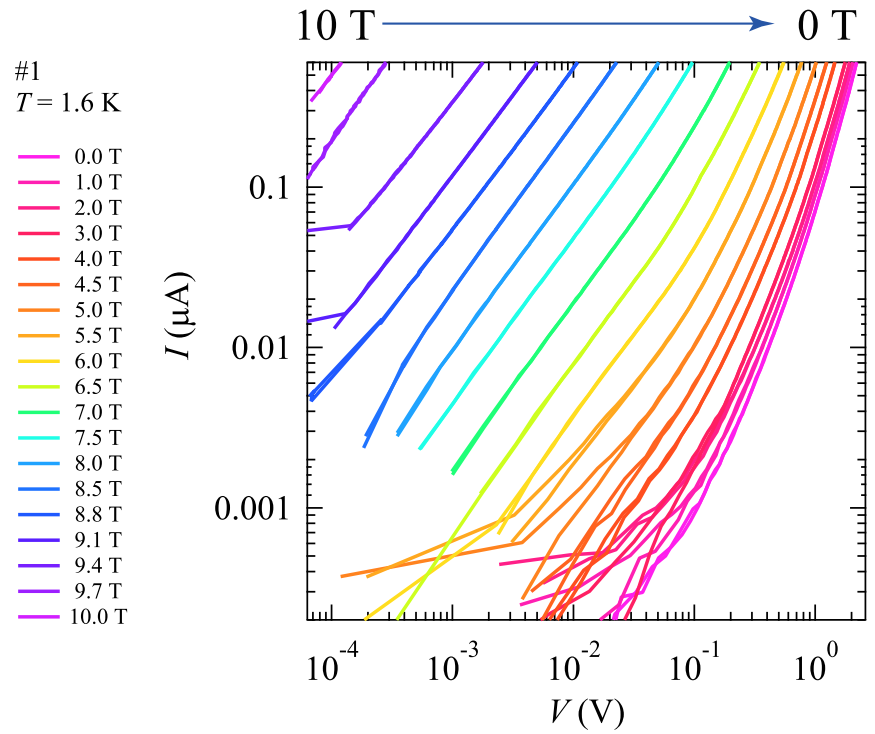

Figure 33: I–V characteristics at various magnetic fields.

the sample is a serious problem. Therefore, our discussion focuses on the data in the voltage region shown in Figs. 32 and 33.

1.1.3 Dielectric constants

Figures 34(a) and (b) show the frequency dependence of the dielectric constants at various temperatures for the electric field E parallel ($\varepsilon_{\rm in}$) and perpendicular ($\varepsilon_{\rm out}$) to the conducting plane, respectively. We see large anisotropy of the dielectric constants between the in-plane and out-of-plane electric fields. Both $\varepsilon_{\rm in}$ and $\varepsilon_{\rm out}$ decrease with increasing frequency and show a $1/f^2$ dependence in the low-frequency region. The extrinsic effect arising from contact resistance and capacitance becomes evident at low frequencies in dielectric constant measurements[36] when the work function of the metal contact is larger than that of the semiconducting sample.[41] Under realistic conditions, the total capacitance is dominated by the contact capacitance, following $1/f^2$ dependence at low frequencies. Therefore, the residual part, which is almost flat at higher frequencies ($f > 100$ Hz), should be intrinsic (from the bulk sample). Above 100 Hz, $\varepsilon_{\rm in}$ is 10 times larger than $\varepsilon_{\rm out}$. Both $\varepsilon_{\rm in}$ and $\varepsilon_{\rm out}$ decrease with decreasing temperature. A similar temperature dependence is observed at 100 kHz.[42]

Figure 35 shows the magnetic field dependence of $\varepsilon_{\rm in}$ and $\varepsilon_{\rm out}$ at 1 kHz and 1.6 K. Both $\varepsilon_{\rm in}$ and $\varepsilon_{\rm out}$ gradually increase with increasing magnetic field and then tend to diverge near 8 T. Above 8 T, reliable data are not obtained because of the low impedance. The field dependence of $\varepsilon_{\rm in}$ has already been measured at 1 kHz above 2.5 K[31] and shows a similar gradual increase.

In dielectric constant measurements, a sample with a layered structure such as λ-$(BETS)_2FeCl_4$ can be modeled as simple electronic circuits with two different capacitors: a parallel circuit and a series circuit for in-plane and out-of-plane measurements, respectively.[36] Assuming that the dielectric constant of the BETS layer ($\varepsilon_{\rm BETS}$) is much larger than that of the $FeCl_4$ layer ($\varepsilon_{\rm FeCl}$), we obtain the relations $\varepsilon_{\rm BETS} \approx \varepsilon_{\rm in}(d_{\rm BETS} + d_{\rm FeCl})/d_{\rm BETS}$ and $\varepsilon_{\rm FeCl} \approx \varepsilon_{\rm out} d_{\rm FeCl}/(d_{\rm BETS} + d_{\rm FeCl})$. Here, $d_{\rm BETS} = \sim$1 nm and $d_{\rm FeCl} = \sim$0.5 nm are the thicknesses of the BETS and $FeCl_4$ layers, respectively. At 1.5 K, we have $\varepsilon_{\rm BETS}/\varepsilon_0 \approx 1.54 \times 10^3$ and $\varepsilon_{\rm FeCl}/\varepsilon_0 \approx 32.8$ at 1 kHz for $\mu_0 H = 0$ T.

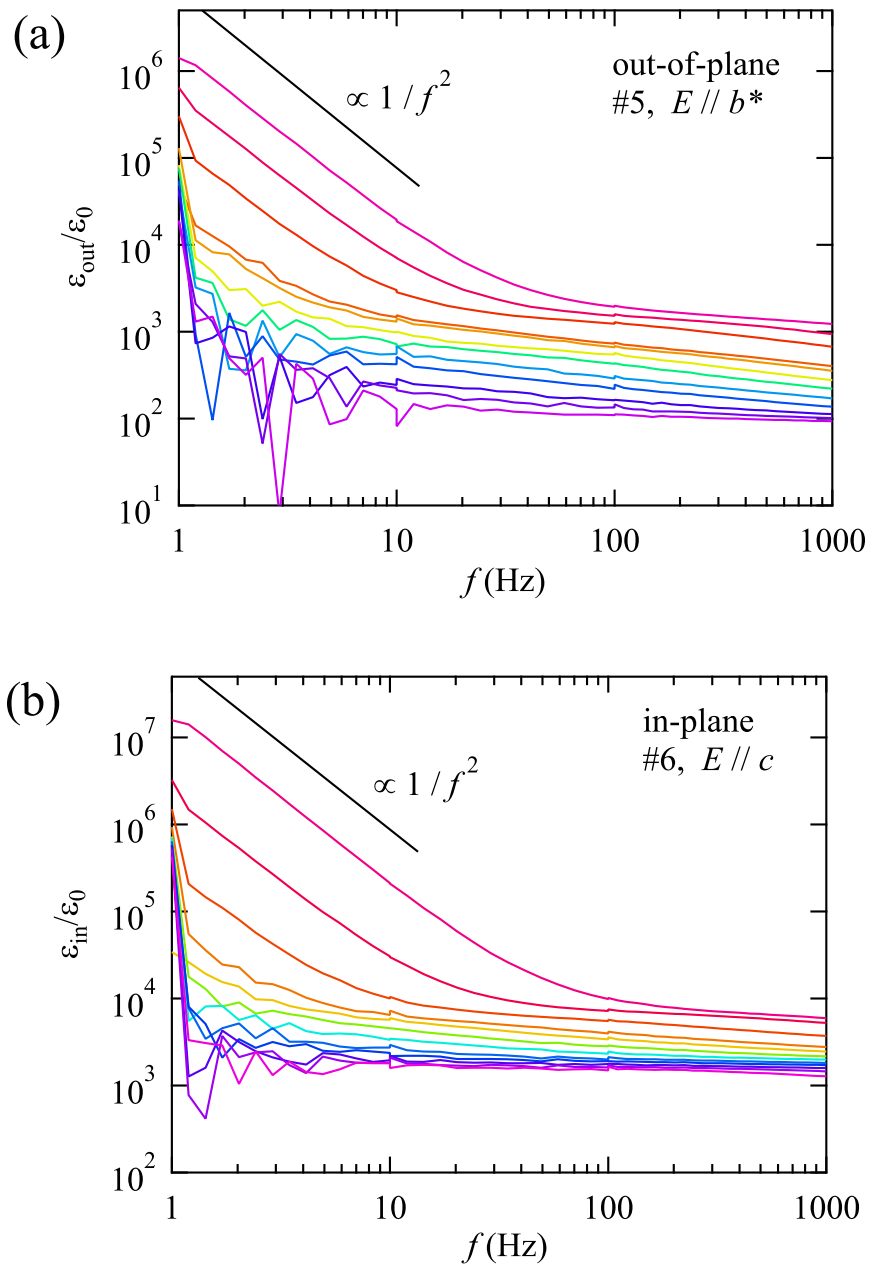

Figure 34: Dielectric constants as a function of frequency at various temperatures in the (a) in-plane and (b) out-of-plane electric fields.

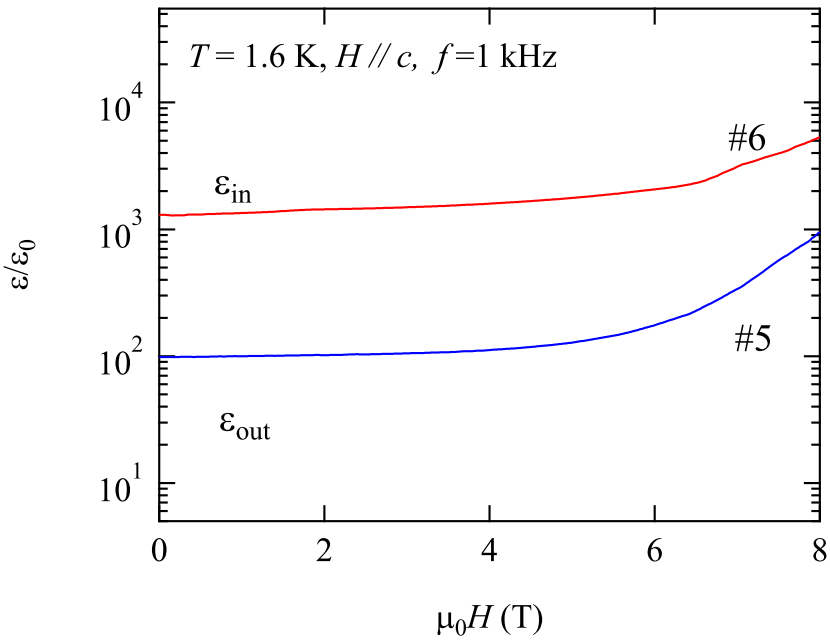

Figure 35: Magnetic field dependence of the in-plane and out-of-plane dielectric constants at 1 kHz for $T = 1.6$ K.

1.2 Magnetic torque

Figures 36 and 37 shows the magnetic field dependence of the magnetic torque curves $\tau_m(H)$ of the Fe salt at 1.6 K. The magnetic field angles θ and ϕ are defined in Figs. 36(b) 37(b), respectively. For $\theta_{\rm SF} = 70°$ (Fig. 36), a very sharp structure appears at 1.2 T ($H_{\rm SF}$), due to the spin-flop transition. As the field increases, the torque signal increases and tends to saturate above ∼10 T. As the field is tilted from the angle $\theta_{\rm SF}$, the sharp structure is spread out. The spin-flop transition is clearly observed in the range of $65° < \theta < 85°$. For H in the a'-b^* plane (Fig. 37), only a broad feature is seen at ∼2 T. The overall behavior is consistent with that found in the previous reports.[53,55] In both field rotations, we note a step-like structure with a small hysteresis at ∼10 T, which is caused by the M–I transition. The derivative curves of the torque near 10 T are presented in Figs. 36(b) and 37(b). Here, we can define the M–I transition ($H_{\rm MI}$) as the peak field of the derivative curves.

Figure 38 shows the magnetic field dependence of the magnetic torque τ_m at various temperatures when the field is applied along the easy axis ($\theta = 70°$). At ∼1.2 T, a sharp structure is seen, which is ascribed to the spin-flop transition.[20,55,63] This structure reduces with increasing temperature. Above $H_{\rm SF}$, in the canted AF (CAF) phase, the magnetic torque increases with increasing field and a step-like structure with a small hysteresis is observed at ∼10 T and 1.6 K, which is caused by the AFI–PM transition.[55,63] As temperature increases, the AFI–PM transition field ($H_{\rm MI}$) decreases with the suppression of the step. The $H_{\rm MI}$ field can be defined as the peak field of the derivative torque curve, $d\tau_m/dH$.[63]

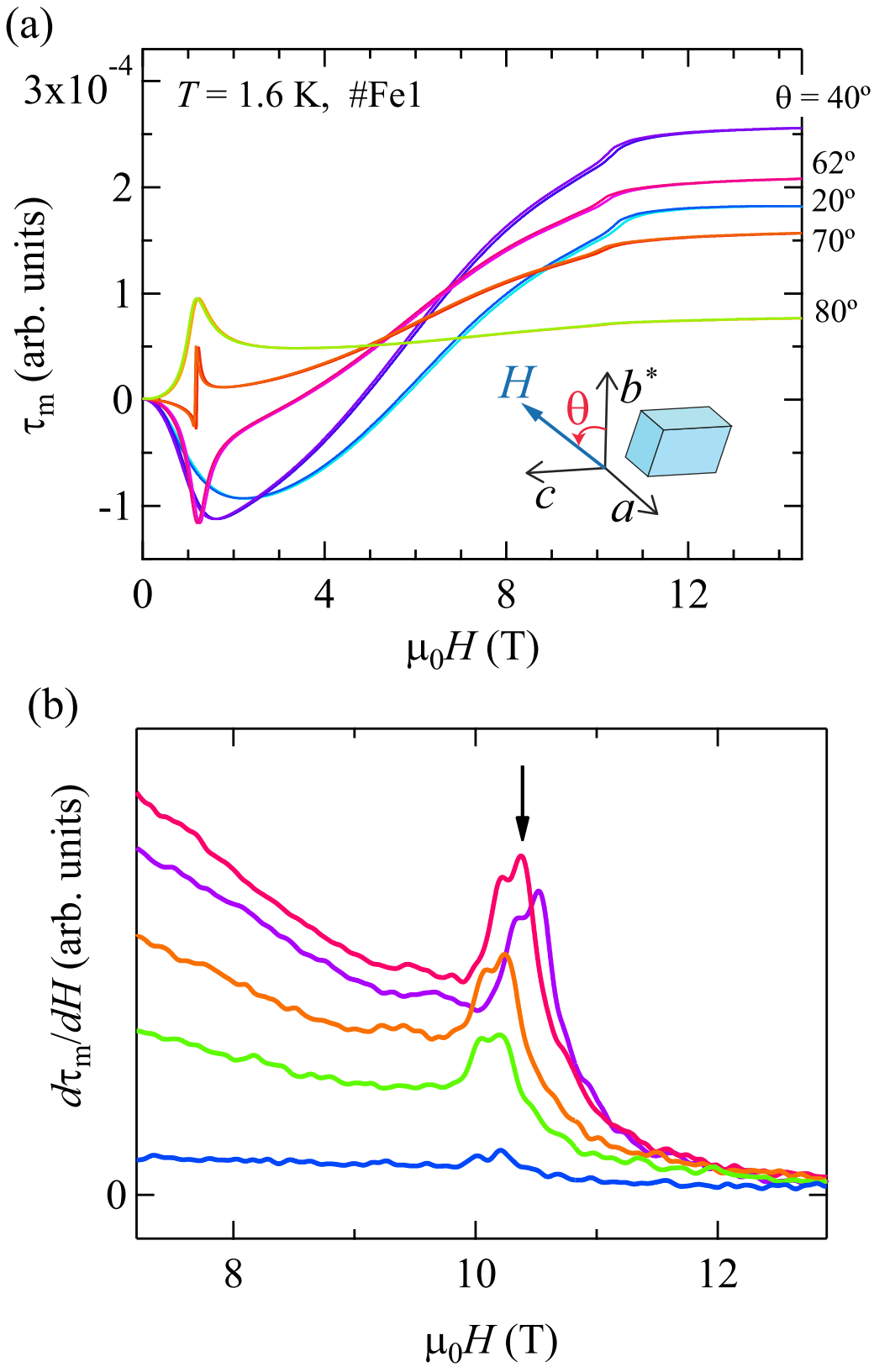

Figure 36: (a) Magnetic field dependence of the magnetic torque of λ-$(BETS)_2FeCl_4$ for H in the b^*–c plane. (b) Derivative curves of $\tau_m(H)$. The arrows indicate the peaks formed due to the AFI–PM transitions.

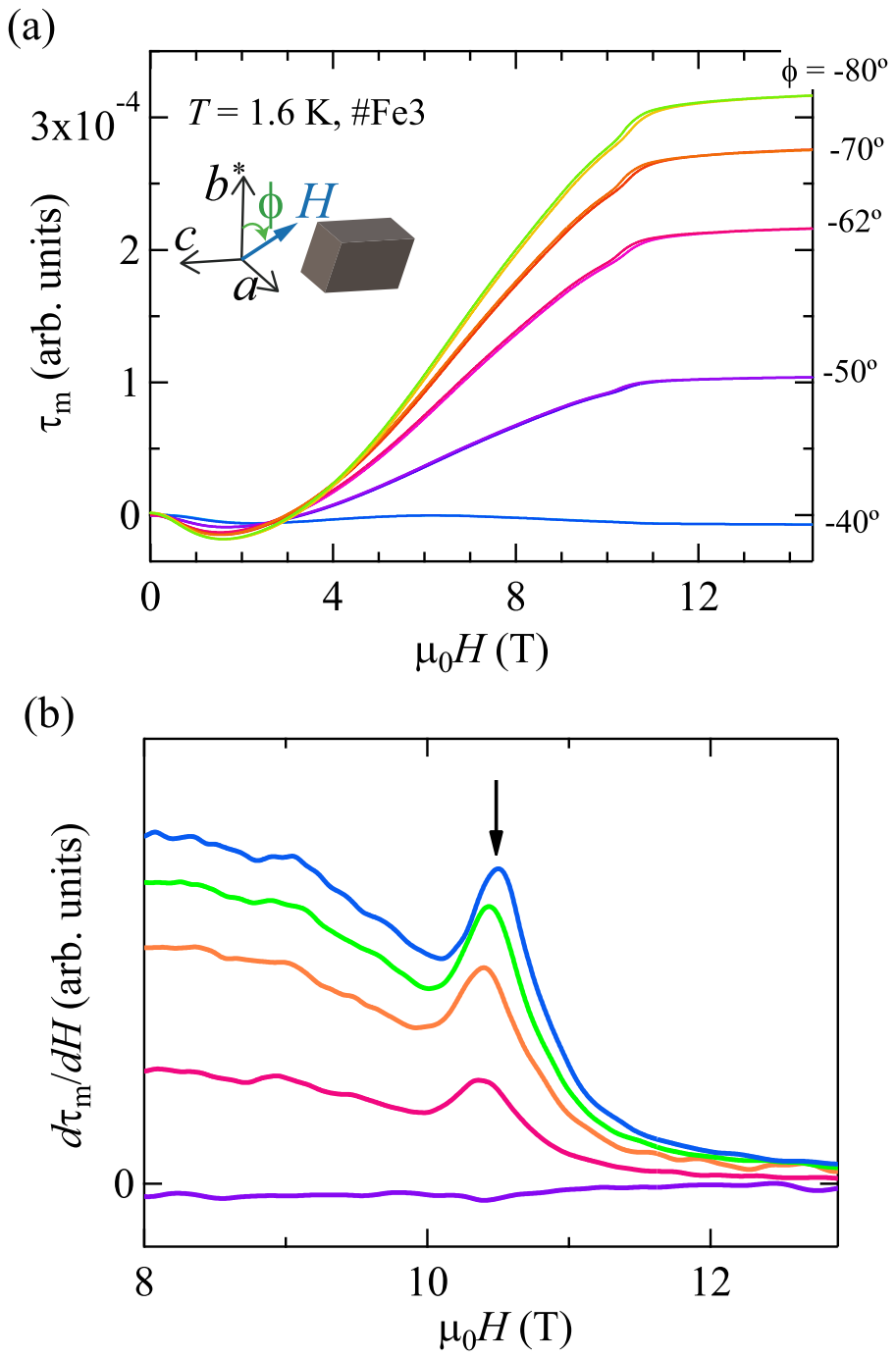

Figure 37: (a) Magnetic field dependence of the magnetic torque of λ-$(BETS)_2FeCl_4$ for H in the a'–b^* plane. (b) Derivative curves of $\tau_m(H)$. The arrows indicate the peaks formed due to the AFI–PM transitions.

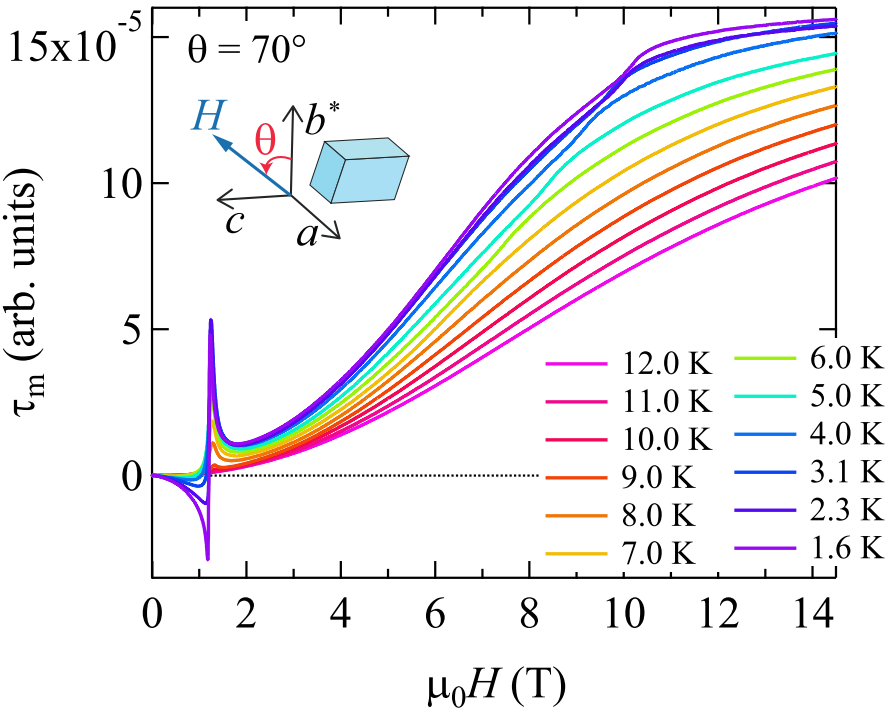

Figure 38: Magnetic field dependence of the magnetic torque in λ-$(BETS)_2FeCl_4$ at various temperatures.

Figure 30(a) shows the angular dependence of H_{MI} for H in the b^*–c plane; a sinusoidal dependence is observed. The solid curve indicates the torque data at 1.6 K and 14 T. The dashed curve schematically indicates the magnetization of the 3d spins (M_{3d}) expected from the torque. For comparison, H_{MI} determined by the resistance measurements[48] at ∼1.6 K is also plotted. Both results are consistent with each other; the H_{MI} curve has a maximum for $H \parallel b^*$. The torque curve measured at 14 T is also shown in the right scale, which will be discussed later. For H in the b^*–c plane, we present similar plots in Fig. 30(b). We see the same anisotropy of H_{MI} between the torque and resistance measurements. The slight difference in the values is probably because of the sample dependence.

Figures 39(a) and 39(b) show the angular dependence of the magnetic torque for H in the b^*–c and a'–b^* planes, respectively. The paramagnetic torque curve at 14 T should follow the $\sin(2\theta)$ dependence (dashed curve), but we see a deviation from it in the positive signal region, as presented in Fig. 39(a). The deviation is caused by the nonlinear behavior of the piezoresistor, which is more evident in the positive region than in the negative one. The nonlinearity amounts to ∼ 20% at 45°. Since the torque signal is linear for small torque signals, the discussion below is not affected by the nonlinear behavior.

For H in the b^*–c plane [Fig. 39(a)], as the field decreases, the curves are distorted from the sinusoidal dependence and a sharp change due to the spin-flop transition is observed at θ_{SF} (= 70°) for $\mu_0 H$ = 1.2 T. Here, we define two angles θ_0^p and θ_0^n, where $\tau(\theta)$ crosses the zero

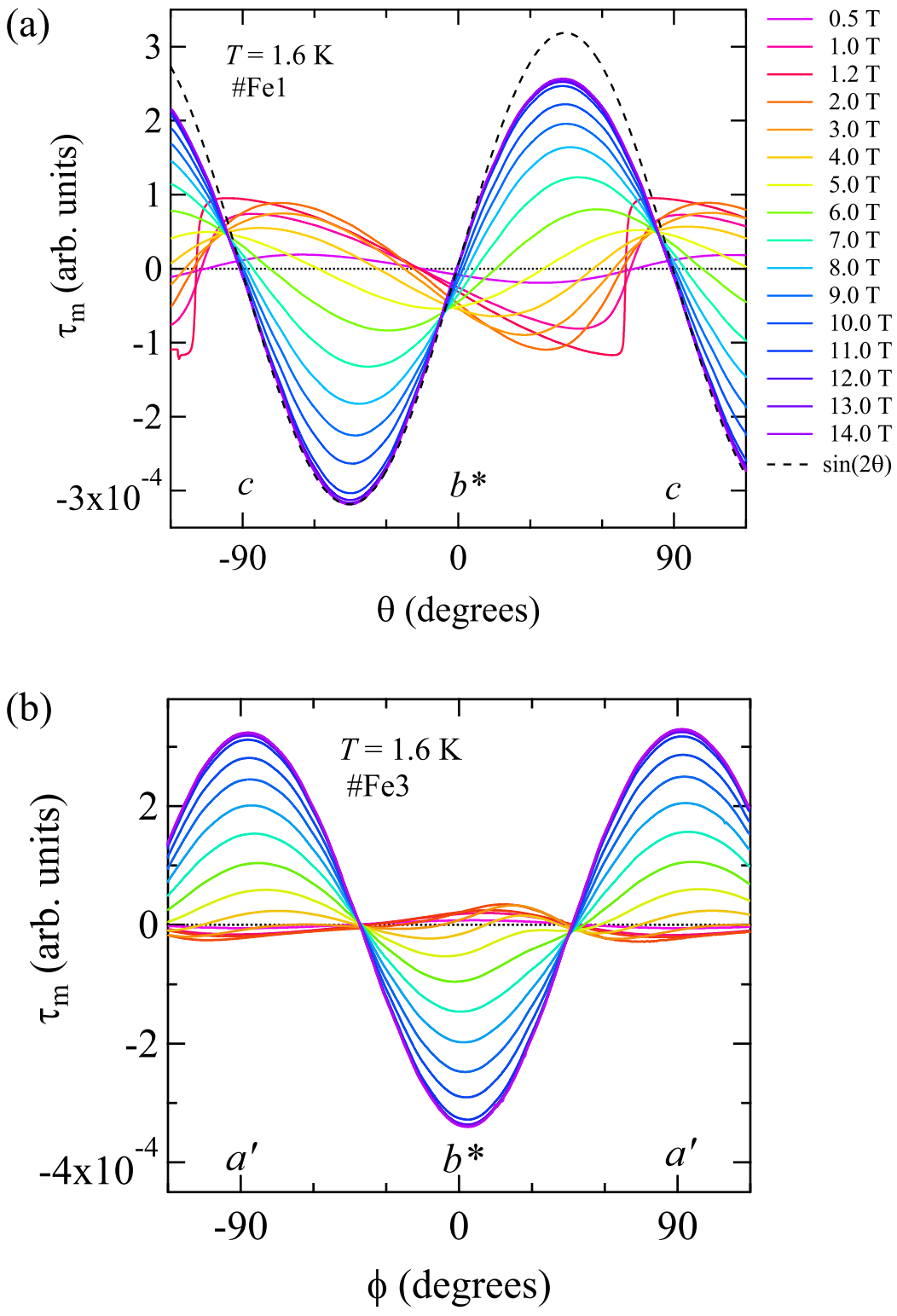

Figure 39: Angler dependence of the magnetic torque of λ-$(BETS)_2FeCl_4$ for H in the (a) b^*–c plane and (b) a'–b^* plane.

line with positive and negative slopes, respectively. A significant feature is that both $\theta_0^{\rm p}$ and $\theta_0^{\rm n}$ change considerably with decreasing field. A similar sharp change in the torque at the spin-flop angle $\theta_{\rm SF}$ is also observed for a π–d system, κ-(BDH-TTP)$_2$FeBr$_4$.[56] However, large field dependence of the zero-crossing angles has been not observed in other π–d systems.[56,58,65] For H in the a'–b^* plane [Fig. 39(b)], as the field decreases, we see a distortion from the sinusoidal dependence but no sharp feature.

For comparison, we measured the torque curves $\tau_m(\theta)$ for the nonmagnetic isostructural salt, the Ga salt [Figs. 40(a) and 40(b)]. At low temperatures, this salt shows superconductivity when the field is applied parallel to the a'–c plane. The sharp features for $\theta = \pm 90^\circ$ and $\phi = \pm 90^\circ$ arise from the superconducting transition.[59] In both rotations, we see a sinusoidal background, resulting from the conducting π spins. The important feature is that the zero-crossing angles $\theta_0^{\rm n} = 55^\circ$ and $\phi_0^{\rm n} = 15^\circ$ are independent of both temperature and field.

Figures 41(a) and 41(b) present the field dependence of the zero-crossing angles $\theta_0^{\rm p}$, $\theta_0^{\rm n}$, $\phi_0^{\rm p}$ and $\phi_0^{\rm n}$ at 1.6 K, respectively. In this plot, the error of the angle will be $\pm 5^\circ$, which is mainly due to the misalignment of the sample. For the Fe salt, $\theta_0^{\rm p}$ is $\sim 70^\circ$ at 0.5 T and gradually decreases with increasing field [Fig. 41(a)]. At $\sim$4 T, we see a rapid change and then again a gradual decrease, which is consistent with the previous report.[60] Above $H_{\rm MI}$, $\theta_0^{\rm p}$ is independent of the field. A similar behavior is seen for $\theta_0^{\rm n}$. By contrast, $\phi_0^{\rm p}$ ($\sim 45^\circ$) and $\phi_0^{\rm n}$ ($\sim -40^\circ$) seem almost field-independent above 4 T but show anomalous behavior at $\sim$4 T [Fig. 41(b)]. The zero-crossing angles for the Ga salt are independent of the field within the experimental error. We cannot define $\theta_0^{\rm p}$ and $\phi_0^{\rm p}$ at 1.6 K and 10 T because of the large superconductivity signal. These results will be discussed later.

Figure 42 shows the torque curves $\tau_m(\theta)$ at various temperatures for the Fe salt. At $T > T_{\rm MI}$, we observe sinusoidal curves. As temperature decreases, the sinusoidal curve is distorted and a sharp change at $\theta_{\rm SF} = 70^\circ$ due to the spin-flop transition becomes evident. Similarly, we define the zero-crossing angles $\theta_0^{\rm p}$ and $\theta_0^{\rm n}$ and plot the temperature dependence in Fig. 43. At 12 K, we note $\theta_0^{\rm p} \approx 0^\circ$ and $\theta_0^{\rm n} \approx -90^\circ$, which are consistent with the data in the high-field PM phase [Fig. 41(a)]. Near $T_{\rm MI}$, the zero-crossing angles markedly change.

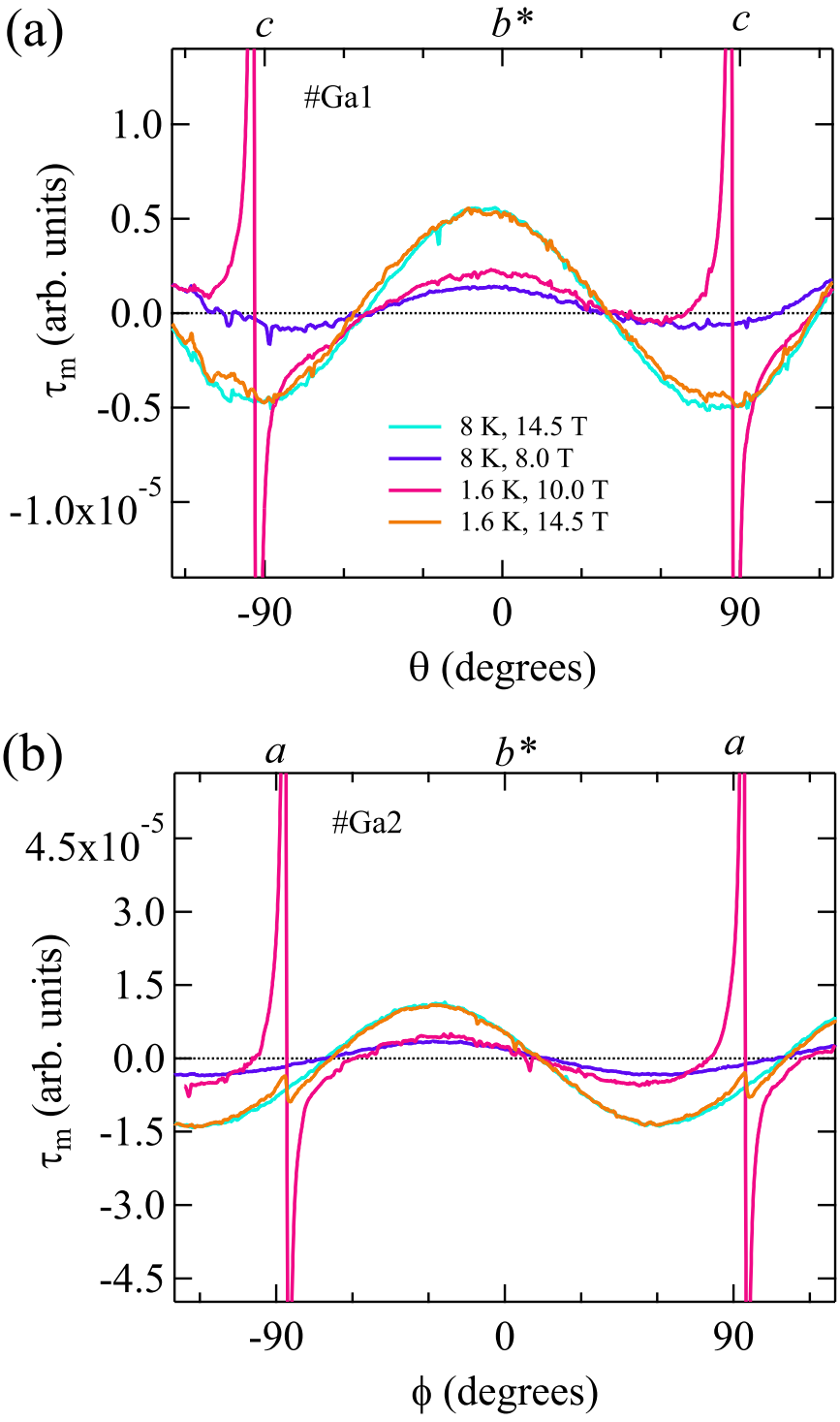

Figure 40: Angular dependence of the magnetic torque of λ-$(BETS)_2GaCl_4$ for H in the (a) b^*–c and (b) a'–b^* planes. The zero-crossing angles $\theta_0^{\rm p}$ and $\theta_0^{\rm n}$ and $\phi_0^{\rm p}$ and $\phi_0^{\rm n}$ are indicated by arrows in (a) and (b), respectively.

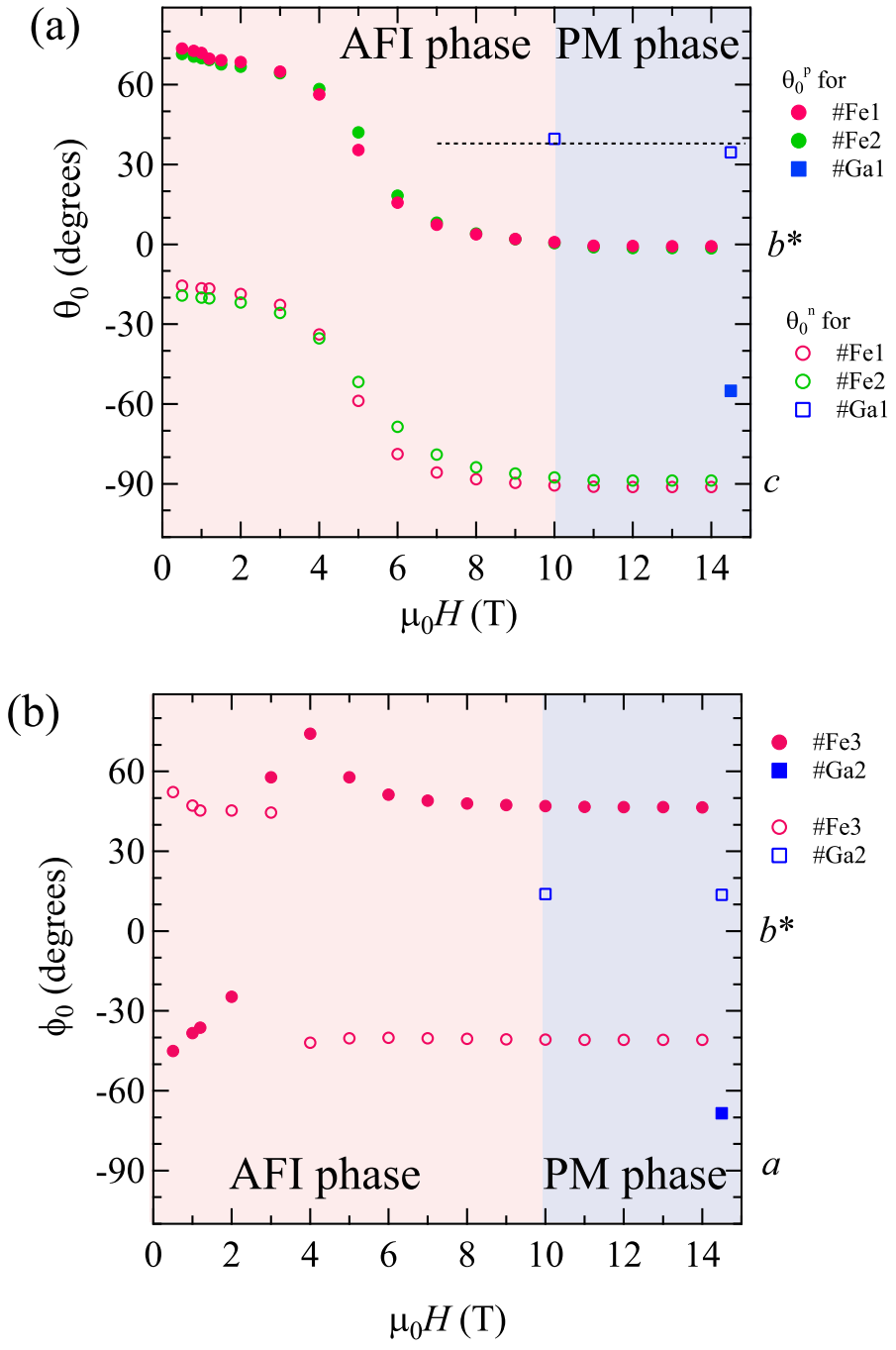

Figure 41: Field dependence of zero-crossing angles (a) θ_0^{p} and θ_0^{n} and (b) ϕ_0^{p} and ϕ_0^{n} at 1.6 K for both salts.

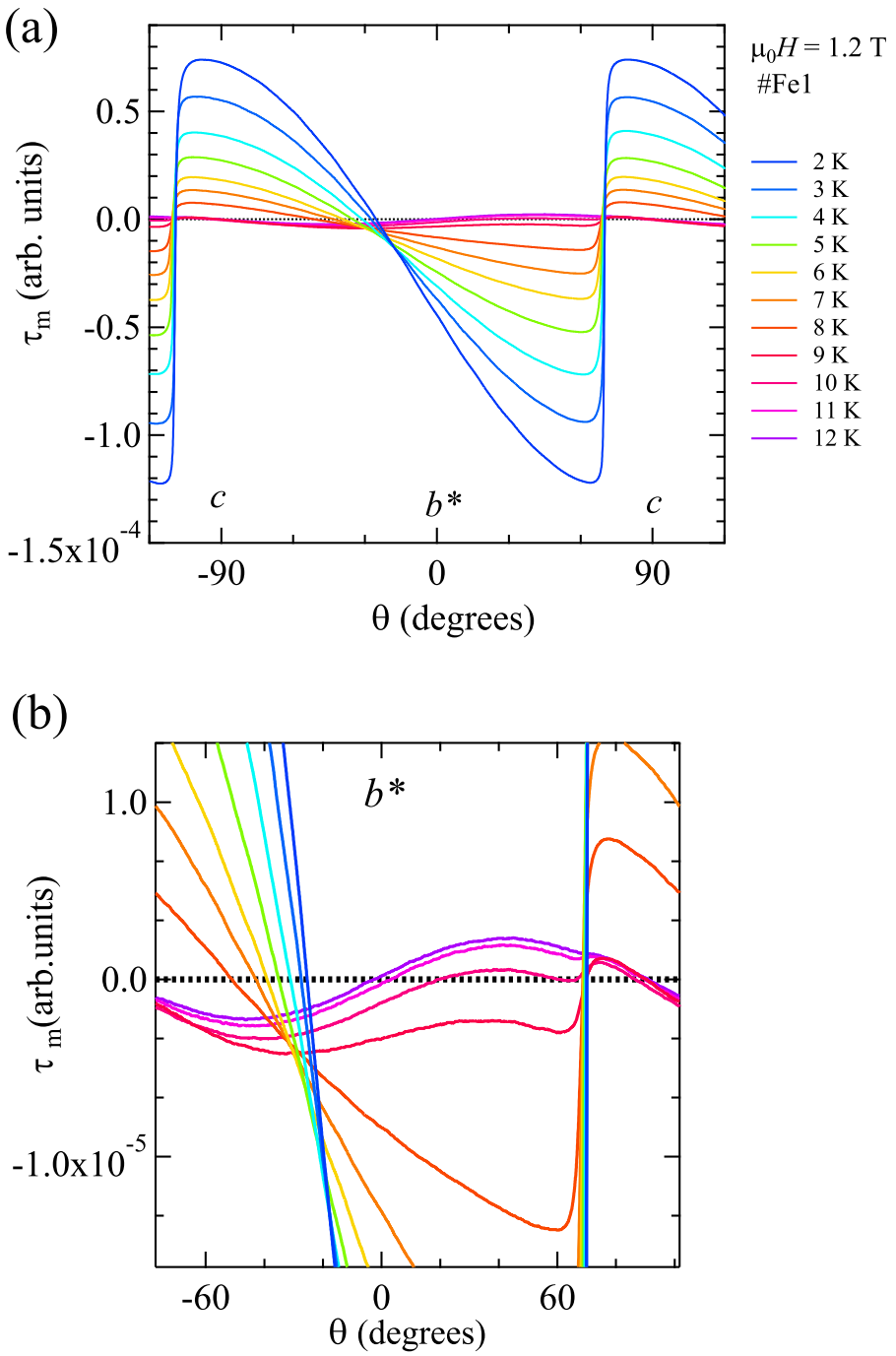

Figure 42: Angular dependence of the magnetic torque of λ-$(BETS)_2FeCl_4$ for H in the b^*–c plane.

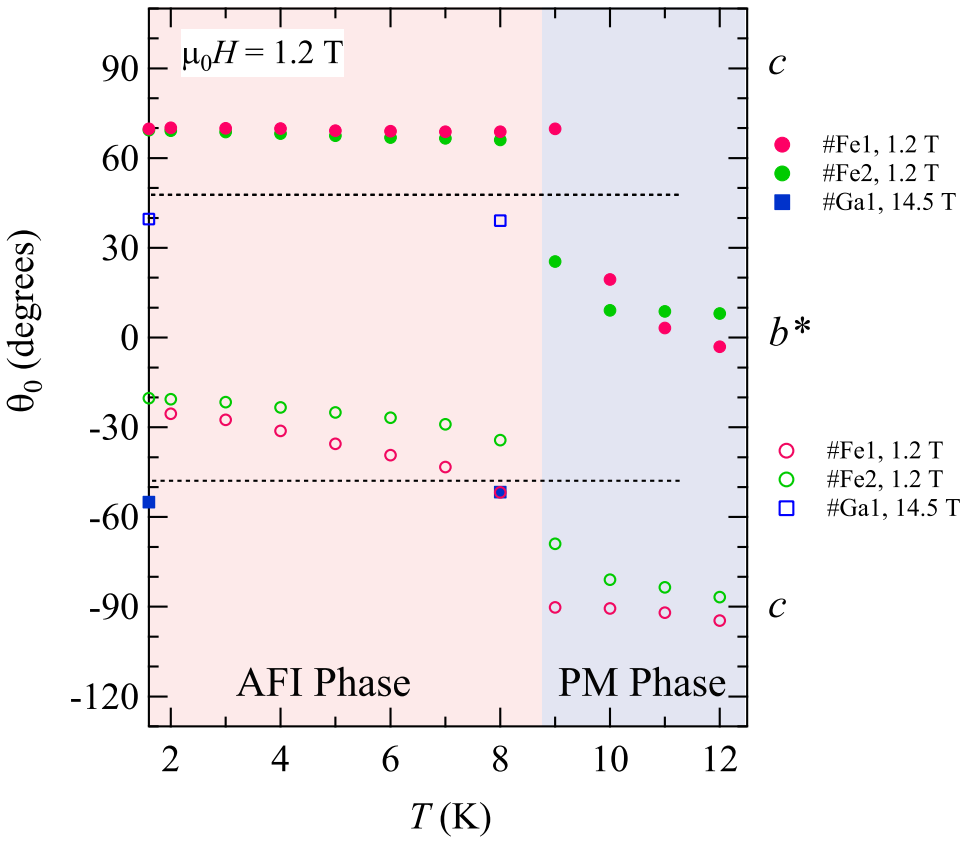

Figure 43: Temperature dependence of zero-crossing angles θ_0^{p} and θ_0^{n} for both salts.

1.3 Magnetocaloric effect

Figure 44(a) shows the field dependence of the MCE $\Delta T(H)$ of the λ-$(BETS)_2FeCl_4$ at the bath temperature $T_{\rm bath} = 1.5$ K. The magnetic field is applied parallel to the c-axis. When the magnetic field increases (up sweep), the MCE is negative ($\Delta T < 0$) up to $\sim$1 T and then becomes positive in the wide-field region up to $\sim$10 T. Around $\sim$5 T, a broad dip in the MCE is observed. At $\sim$10 T, the MCE shows a sharp dip, and then gradually decreases with increasing field.

For the down sweep, we observe an almost symmetric ΔT curve to the up sweep curve. The dip at $\sim$10 T shows a significant hysteresis, suggesting a first order phase transition. As the temperature increases [Fig. 44(b)], the dip at $\sim$10 T shifts to a low field, whereas the dip at $\sim$1 T does not shift. An interesting point is that the broad dip field ($H_{\rm dip}$), indicated by an arrow, is almost temperature-independent but the dip is reduced with increasing temperature.

In Fig. 45, we present the magnetic phase diagram, where the $H_{\rm MI}$, $H_{\rm dip}$ and $H_{\rm SF}$ obtained from the MCE and torque measurements are plotted. The $H_{\rm MI}$ and $H_{\rm SF}$ values are consistent with previous reports.[1,7,15,20,21,55,66]

Figures 46(a) and 46(b) show the field dependence of the magnetic torque and the MCE for the up sweep at various field directions θ, respectively. In the magnetic torque [Fig. 46(a)], the spin-flop transition (sharp feature) at 1.2 T is evident for $\theta = 70°$, which corresponds to the magnetic easy axis.[20,55,63] In the MCE [Fig. 46(b)], a small sharp peak (arrow) immediately after the rather broad dip is observed at 1.2 T. Comparing with the torque data, we can assign the small sharp peak to the spin-flop transition. This sharp peak is most evident for $\theta = 80°$. The accuracy of the sample setting is within $\sim \pm 5°$.

Figures 47(a) and 47(b) show relaxation curves of ΔT when the up sweep is stopped at 0.5 T (in the AFI phase) and 11.5 T (in the PM phase), respectively. The dotted curves are the results fitted with the equation $\Delta T = \Delta T_0 \exp(-t/\tau)$. The relaxation times are estimated as $\tau = 6.3$ s at 0.5 T and $\tau = 1.8$ s at 11.5 T. The relaxation of ΔT is measured at various fields and then τ is plotted as a function of field in Fig. 47(c). In the whole field range, τ has a tendency to decrease with increasing field. At $H_{\rm MI}$, we observe significant enhancement of τ.

Figure 48 shows the magnetic field dependence of the MCE at the easy axis for three different sweep rates v_H. The absolute value of ΔT linearly increases with increasing rate (inset) in the whole field region except at $H_{\rm SF}$ and $H_{\rm MI}$, which shows that ΔT arises mainly from the second term of Eq. (41). At $H_{\rm SF}$ and $H_{\rm MI}$, the ΔT values are not proportional to v_H. The results show that the latent heats, which are independent of v_H, also contribute to the MCE at these transitions.

When the second term in Eq. (41) is dominant, the magnetic entropy is approximately written as

$$S_m(H) \approx -\frac{\kappa_{\rm T}}{T v_H} \int_0^H \Delta T(H)\, dH + S_m(H=0) \tag{42}$$

The S_m curves calculated from the ΔT curves in Fig. 44(b) and specific heat data[66] are

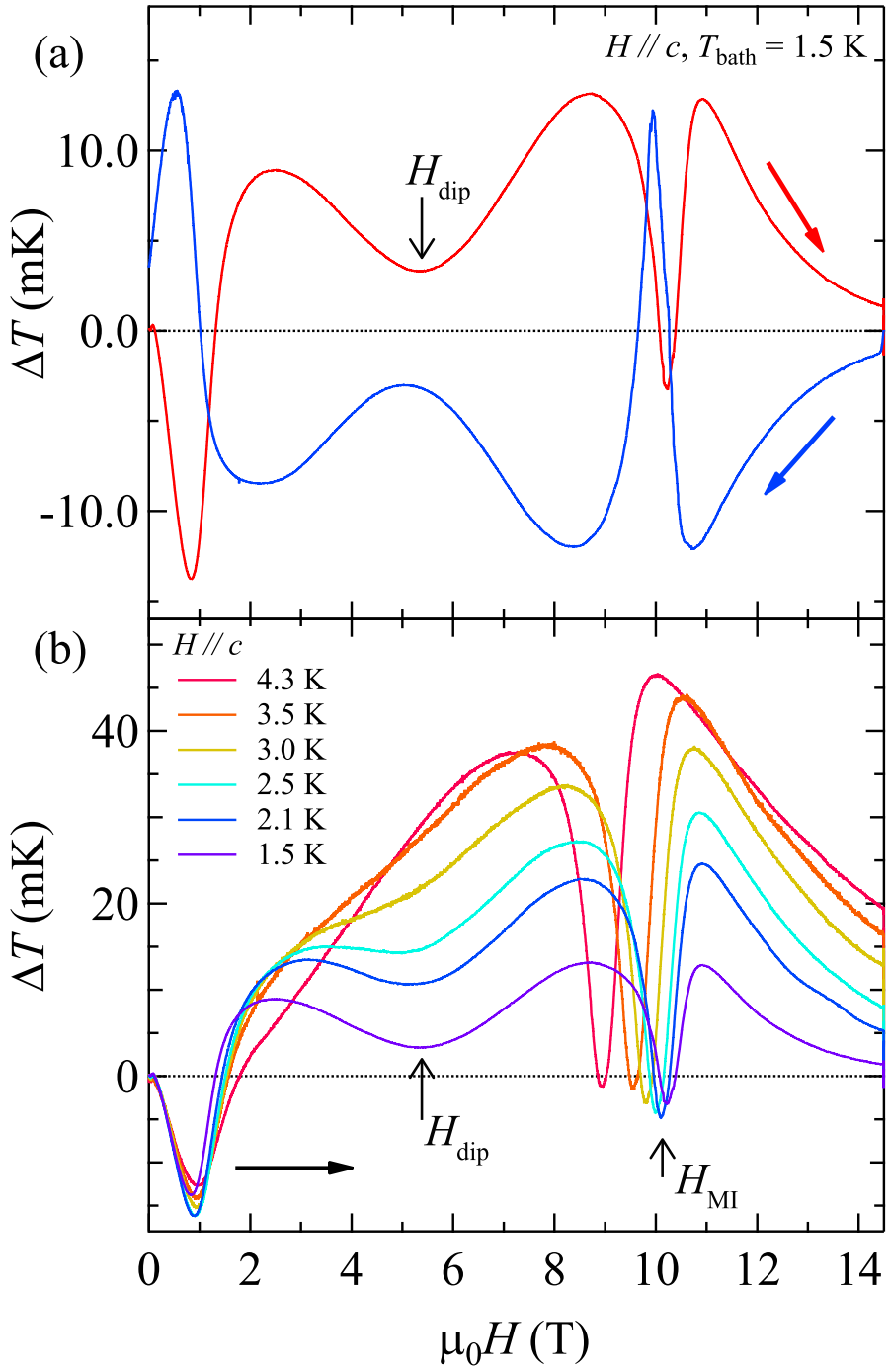

Figure 44: Magnetic field dependence of ΔT in λ-$(BETS)_2FeCl_4$ (a) for up and down sweeps at 1.5 K, and (b) for up sweep at various temperatures.

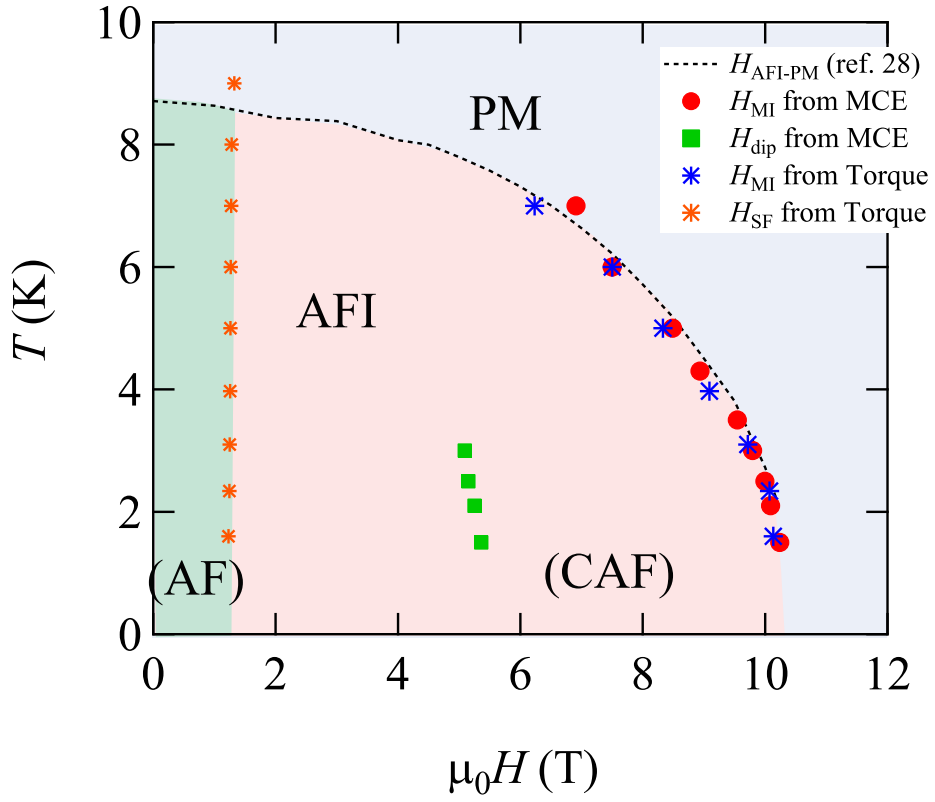

Figure 45: Magnetic phase diagram of λ-$(BETS)_2FeCl_4$ for $H \parallel c$ by the MCE (red circles) and for $\theta = 70°$ by magnetic torque (blue stars). Dashed line shows the AFI–PM phase transition field obtained from the specific heat study.

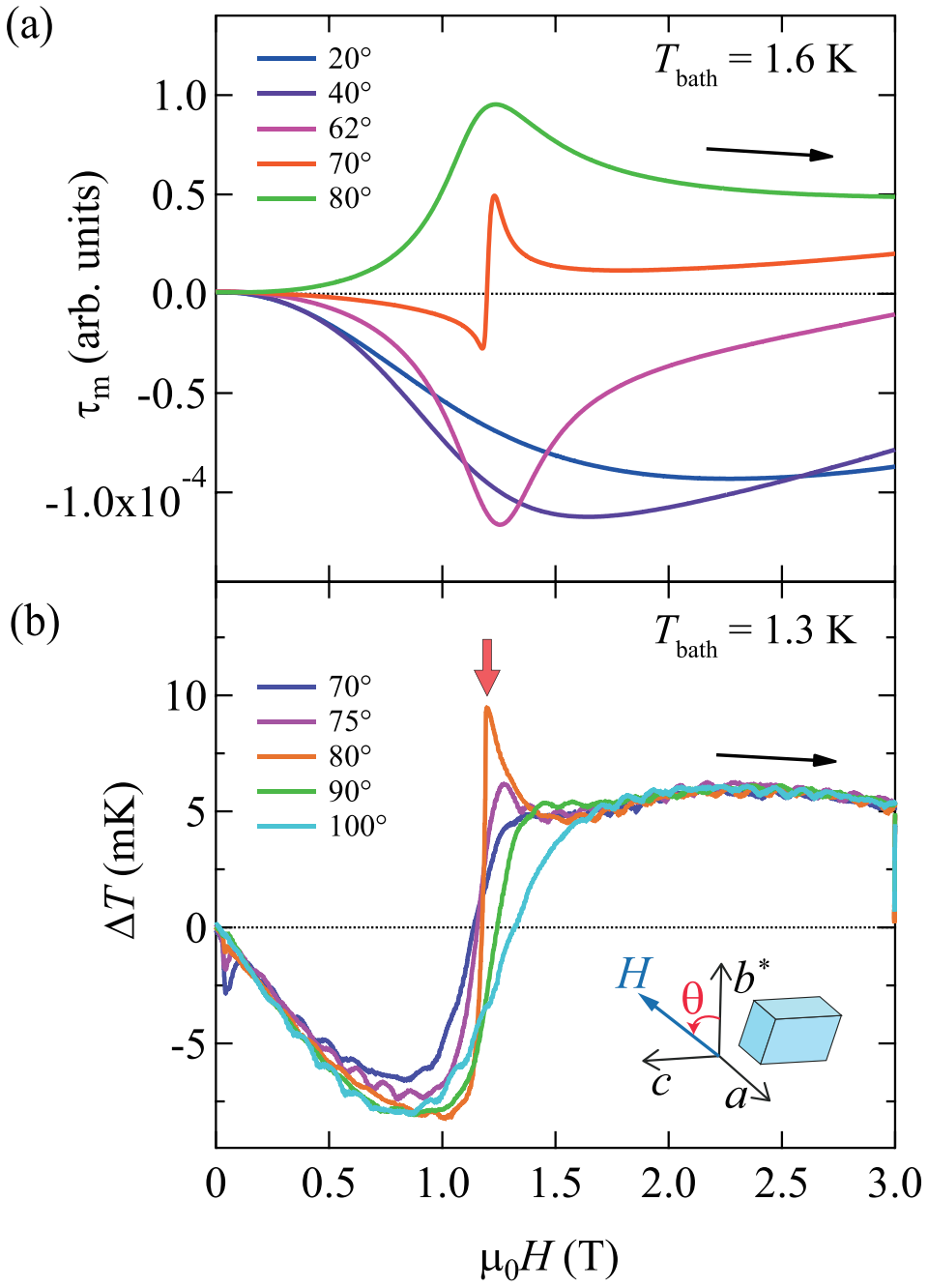

Figure 46: Magnetic field dependences of (a) magnetic torque τ_m[63] and (b) MCE $\Delta T(H)$ of λ-$(BETS)_2FeCl_4$ for up sweep at various field angles.

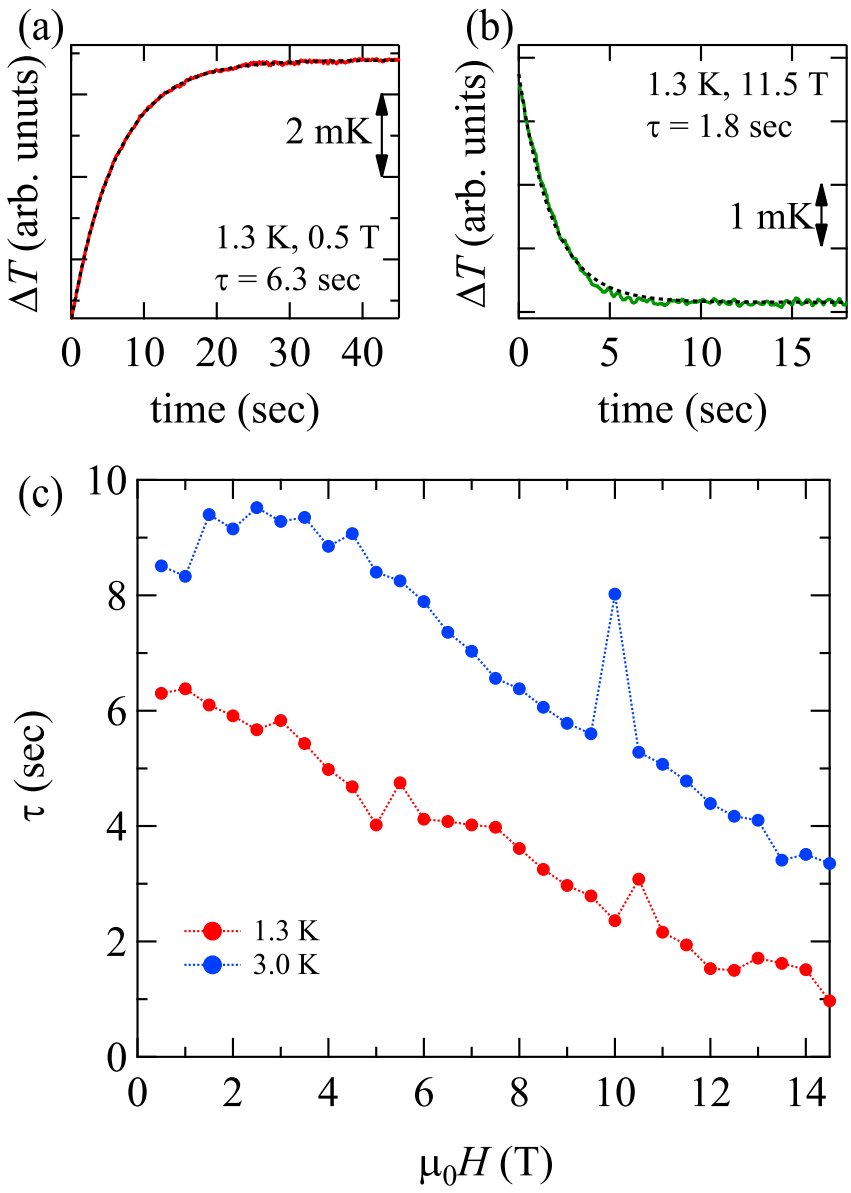

Figure 47: (a) and (b) show relaxation curves of ΔT with fitted results at 0.5 T (AFI phase) and 11.5 T (PM phase), respectively. The relaxation times τ as a function of field are plotted in (c). Significant enhancement at ∼10 T shows the AFI–PM transition.

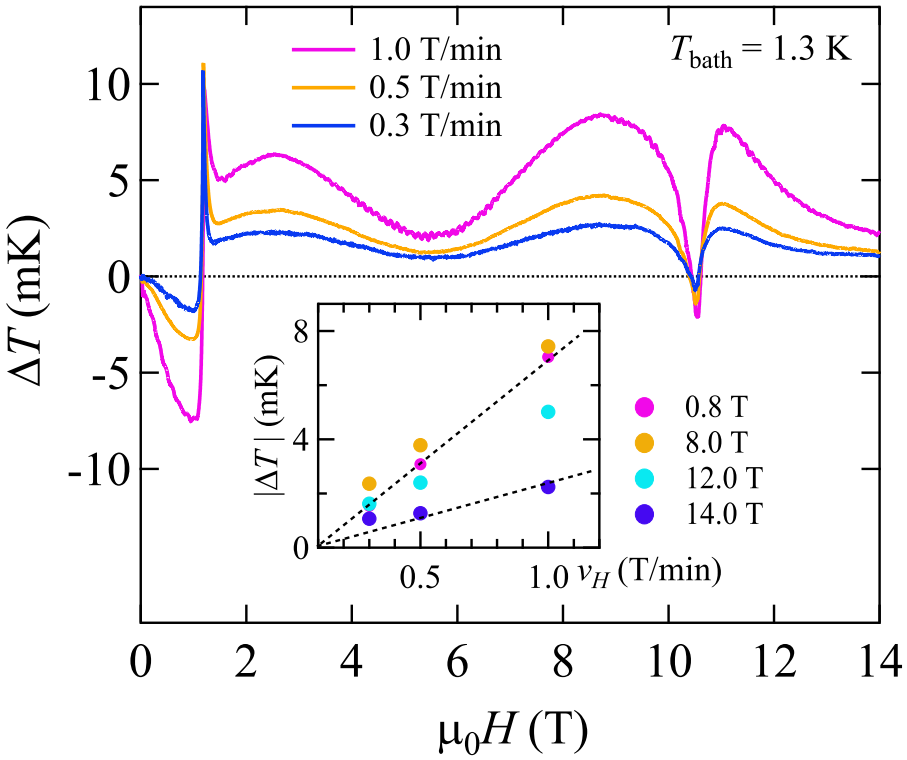

Figure 48: Magnetic field dependence of ΔT for $\theta = 70°$ and $T = 1.3$ K at various magnetic field sweep rates v_H.

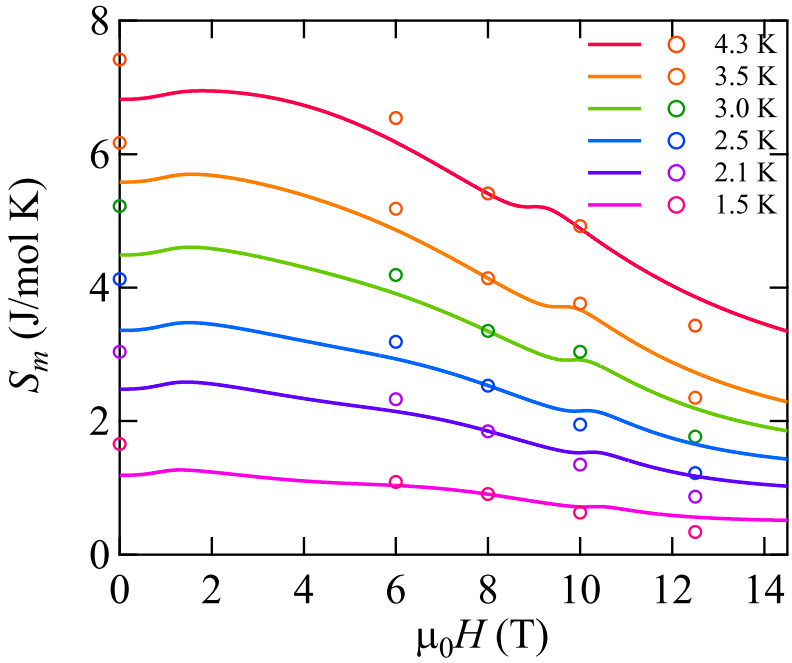

Figure 49: Magnetic entropy S_m calculated from the experimental ΔT curves.

presented in Fig. 49. The zero-field entropy $S_m(H = 0)$ is the unknown parameter. For simplicity, the $S_m\,(H)$ curves are shifted such that $S_m(8\ \mathrm{T})$ coincides with that obtained from the specific heat data.[66] The field dependence is in reasonable agreement with each other. The result shows that the second term in Eq. (41) contributes predominantly to the MCE. Each $S_m(H)$ curve has a broad maximum at ∼1.5 T, which decreases with increasing field.

A small sharp peak at ∼1.2 T due to the spin-flop transition is observed [Fig. 46(b)] in contrast to the sharp large dip arising from the AFI–PM transition. At H_{SF}, the positive peak $\Delta T > 0$ for the up sweep shows a negative entropy jump $\Delta S_m < 0$. Since the magnetization should have a positive jump $\Delta M > 0$ at H_{SF}, we obtain $dH_{\mathrm{SF}}/dT > 0$ from the Clausius–Clapeyron equation, $\Delta S_m/\Delta M = -dH_{\mathrm{SF}}/dT$. From Fig. 45, we note that H_{SF} slightly increases with increasing temperature; dH_{SF}/dT has a small positive value at low temperatures. The relation $dH_{\mathrm{SF}}/dT > 0$ is a common feature for AF systems.

For comparison, the field dependence of the MCE $\Delta T\,(H)$ of the κ-$(\mathrm{BETS})_2\mathrm{FeBr}_4$ at various temperatures for $H \parallel a$ is presented in Fig. 50(a). In κ-$(\mathrm{BETS})_2\mathrm{FeBr}_4$, the $3d$ spins ($S = 5/2$) of the Fe ions show an AF transition at $T_{\mathrm{N}} = 2.5$ K [Fig. 50(a), inset].[65] In contrast to λ-$(\mathrm{BETS})_2\mathrm{FeCl}_4$, the π electrons remain in a metallic state below T_{N} and show superconductivity at 1.5 K (T_{c}). The π–d interaction $J_{\pi d} \sim 5.16$ K is about one-third of that in λ-$(\mathrm{BETS})_2\mathrm{FeCl}_4$.[6] For $H \parallel a$, the $3d$ spins show a metamagnetic transition at 1.5 T (H_{M}). As the magnetic field increases, ΔT shows a sharp dip at H_{M}, which is observed up to 2.6 K. After the dip, the ΔT curve exhibits a hump and then gradually approaches zero with increasing field. The behavior

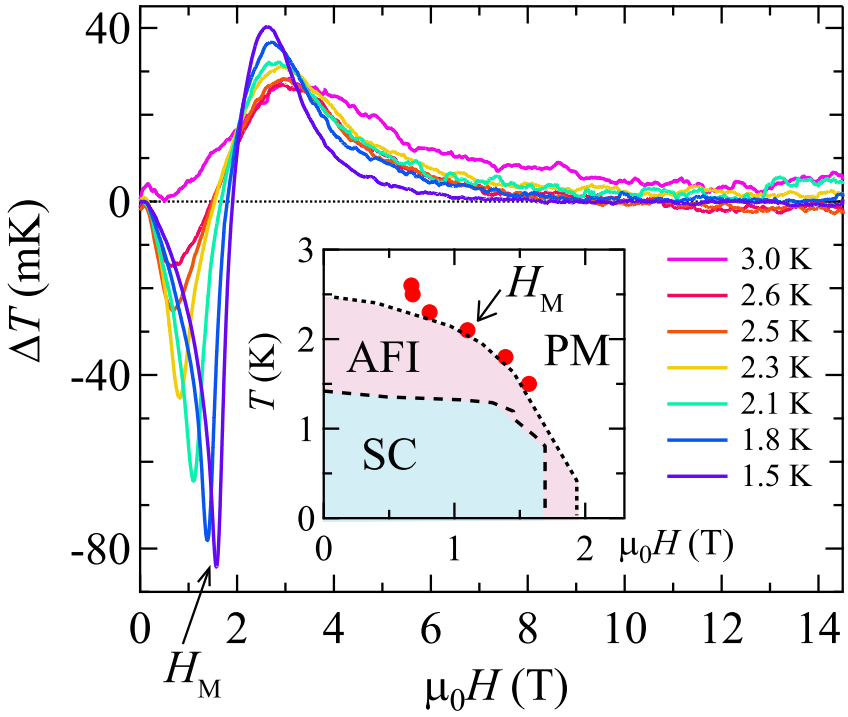

Figure 50: Field dependence of ΔT of κ-$(BETS)_2FeBr_4$ at various temperatures.

will be discussed later.

Chapter 2

Discussion

2.1 Charge transport model

A charge transport model was first proposed by Y. Takahide *et al.* to explain the nonlinear I–V characteristics in charge-ordered and Mott insulating phases.[33] The conductivity in this model is based on the electric-field (E)-dependent potential barrier $\Delta(E)$ between the thermally excited electron and hole [Fig. 51(a)]. The total conductivity is given by $J/E = \sigma_0 \exp[-\Delta(E)/2k_{\rm B}T]$, where J is the current density. For λ-$(BETS)_2FeCl_4$, the transfer integral t is highly anisotropic: the in-plane t is considerably larger than the out-of-plane t. Therefore, the excited electron–hole pairs remain in the same layer. In the AFI phase of λ-$(BETS)_2FeCl_4$, since $\varepsilon_{\rm BETS} \gg \varepsilon_{\rm FeCl}$, the electric fluxes between the thermally excited hole and electron are confined in each layer. Then, the attractive Coulomb potential $\varphi(r)$ between the electron and hole with a distance r has a 2D form,

$$\varphi(r) = -\frac{2e}{4\pi\varepsilon_{\rm BETS} d_{\rm BETS}} \left[\ln\left(\frac{r}{2\sqrt{d_{\rm BETS} d_{\rm FeCl} \eta}} \right) + C \right], \tag{43}$$

for $d_{\rm BETS} \ll r \ll \sqrt{d_{\rm BETS} d_{\rm FeCl} \eta}$, where $\eta = \varepsilon_{\rm BETS}/\varepsilon_{\rm FeCl}$ and C is the Euler constant.[43] Thus, the Coulomb potential is written as $U_0 \ln(r/a)$, where r is shorter than the cutoff length $\lambda = \sqrt{d_{\rm BETS} d_{\rm FeCl} \eta}$. Here, a is the minimum length scale, which we take as the size of the BETS molecule ($\sim$0.5 nm). The Coulomb potential reaches the 3D form $1/r$ at a longer distance. For simplicity, we take a constant Coulomb potential $\varphi(E) = U_0 \ln(\lambda/a)$ for $r > \lambda$ in the following simulation [Fig. 51(b)]. The activation energy $\Delta(E)$ in the electric field E is given by the maximum value of the $\varphi(E)$ curve, $\Delta(E) = U_0 \ln(U_0/eEa) - U_0$ for $U_0/e\lambda \leq E$ and $\Delta(E) = U_0 \ln(\lambda/a) - eE\lambda$ for $U_0/e\lambda > E$. Under the experimental condition ($U_0/ea \gg E$) of this study, nonlinear I–V characteristics, which follow the power law at high electric fields, $U_0/e\lambda \leq E$, $J \propto E^{\alpha} (\alpha = U_0/2k_{\rm B}T + 1)$, are obtained . In the low-electric-field region, $U_0/e\lambda \gg E$, $\Delta(E)$ is almost independent of E, $\Delta \approx U_0 \ln(\lambda/a)$. Therefore, a linear I–V curve is obtained. The activation energy $\Delta/k_{\rm B} \approx 30$ K is determined from the Arrhenius plot [Fig. 28(c)].

The dotted curves in Fig. 32 show the I–V characteristics calculated by the above model

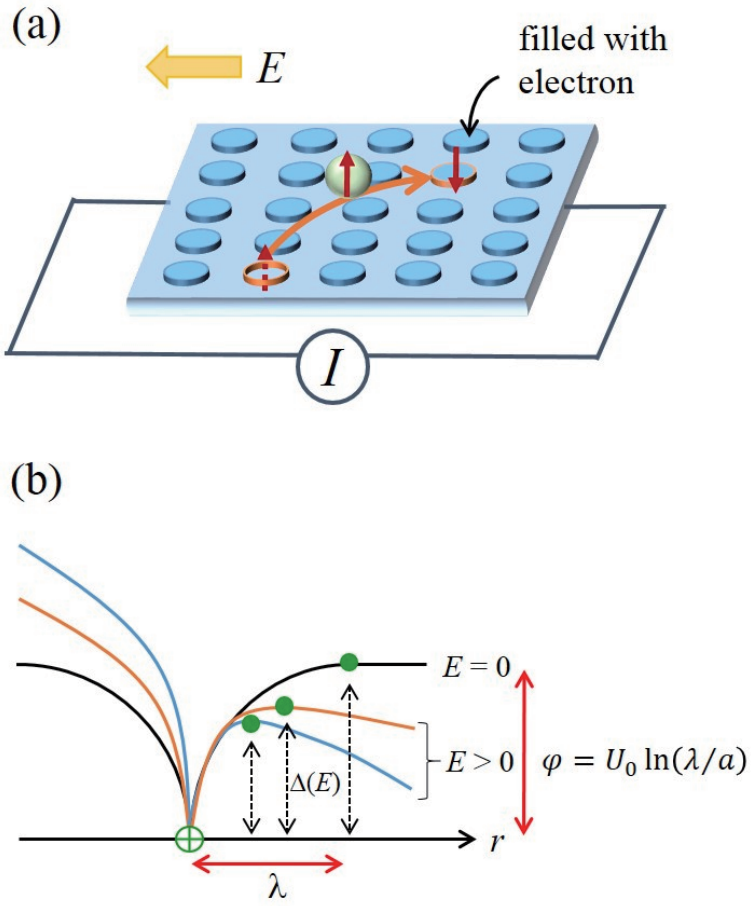

Figure 51: (a) Schematic illustration of the charge excitation in the AFI phase. (b) Coulomb potential curves between the thermally excited electron and hole at zero and finite electric fields.

for 1.6 K $\leq T \leq$ 2.75 K. The calculations include only one parameter $\lambda \approx 100$ nm. Note that the experimental results are well reproduced. The reasonably good agreement shows that the charge transport in the AFI phase of λ-$(BETS)_2FeCl_4$ can be characterized by the energy gap Δ determined by the Coulomb potential between the excited electron and hole. This energy gap is completely different from that of semiconductors, where Δ is given by the band gap. This model is valid only when Δ is constant. The results in Fig. 28 show that Δ changes above 3 K, implying that the dielectric constant and λ change with temperature. Such a change may be related to the anomalous behavior of the dielectric constant[15] and charge disproportionation.[30]

Here, we compare the parameters obtained from the analyses of the I–V characteristics with those for θ-$(BEDT\text{-}TTF)_2CsZn(SCN)_4$.[33,37] As shown in Table I, the Δ/k_B values are comparable to each other. However, the power-law exponent α at the base temperature shows a larger difference. From the relation $\Delta \approx U_0 \ln(\lambda/a)$, the larger λ of λ-$(BETS)_2FeCl_4$ gives a smaller U_0. Therefore, we obtain a smaller α because $\alpha \propto U_0$.

From the ε_{BETS} and ε_{FeCl} values at 1.6 K for $f = 1$ kHz, we obtain the cutoff length $\lambda \approx 6$

Table 5: Parameters obtained from the analyses of the I–V characteristics.

Material	λ-$(BETS)_2FeCl_4$	θ-$(BEDT\text{-}TTF)_2CsZn(SCN)_4$[33,37]
T_{MI} (K)	8.5	20
Δ/k_B (K)	30	24
α (at base temperature)	~3	~8
λ (nm)	100	23

nm, which is shorter than the experimental result ($\lambda \approx 100$ nm) obtained from the I–V curve calculations. Similar differences have been found in other bulk crystals[33–37] and are explained in terms of certain inhomogeneities of the samples. To obtain the I–V characteristics, the electrical contacts are made in a small region (~ 20 μm) on the flat surface of the crystal, but the dielectric constant is measured for the bulk crystal (~ 200 μm). Therefore, the dielectric constant could be more affected by microcracks, which may be induced during cooling. These cracks will strongly reduce the in-plane capacitance, which leads to the underestimation of λ.

2.2 Spin-flop transition

As shown in Fig. 31, a dip in the resistance is observed at the spin-flop transition. A resistance anomaly at the spin-flop (or metamagnetic) transition has been reported in various π–d systems. In $(EDT\text{-}DSDTFVSDS)_2FeBr_4$, the resistance is semiconducting below 30 K[44,45] and shows a dip at the spin-flop transition field ($H_{SF} = 1.8$ T) in the AF phase of the Fe 3d spins ($T_N = 3.3$ K). In $(DIETSe)_2FeCl_4$, the π electrons show an incommensurate spin-density-wave transition[46] at 10 K under a pressure of 3.5 kbar. A small dip in the resistance is observed at H_{SF} (= 1.5 T) in the AF phase of the Fe 3d spins ($T_N = 4$ K). For κ-$(BDH\text{-}TTP)_2X$, where X = $FeBr_4$ and $FeCl_4$, the resistances show steep decreases (not dips) at H_{SF} (= 2 T) and at the metamagnetic transition field ($H_M = 0.15$ T), respectively, in the AF phases of the Fe 3d spins.[9] For all these salts, the changes in resistance at H_{SF} or H_M are explained by the magnetic scattering between the π and 3d spins via the π–d interaction. Among the above salts, the dip behavior in $(EDT\text{-}DSDTFVSDS)_2FeBr_4$ is similar to that shown in Fig. 31; a small dip is superimposed on the negative magnetoresistance. However, the crucial difference from the above π-d systems is that the π spins are antiferromagnetically ordered but the 3d spins are not for λ-$(BETS)_2FeCl_4$.

On the basis of the electron–hole excitation model described above, we could qualitatively explain the dip at H_{SF}. The spin state has not been taken into account in the above model. However, in the AFI phase, an up (down)-spin electron must be excited to a down (up)-spin site [Fig. 51(a)]. This means that the number of possible excited states (doubly occupied sites) is half of the total number of sites. Even for $H > H_{SF}$, the situation is the same. Since the π spin exchange interaction ($J_{\pi\pi} \approx 450$ K[6]) is much larger than the Zeeman energy, the neighboring π spins are almost antiparallel to each other for $H > H_{SF}$ (inset of Fig. 31). For $H \approx H_{SF}$, on

the other hand, the spin state will be fluctuating greatly between the two states. This situation will effectively increase the number of possible excited states, which leads to a resistance dip at $H_{\rm SF}$.

2.3 Angular dependence of $H_{\rm MI}$ transition field

In the PM phase, the localized $3d$ spins are strongly polarized but the π spins are hardly polarized. Therefore, the free energy in the PM phase is approximately given by $F_{\rm PM}(H) = F_{\rm PM}(0) - M_{3d}H$, where $F_{\rm PM}(0)$ corresponds to the free energy of the π spins and M_{3d} is the magnetization of the $3d$ spins, $\langle M_{3d}\rangle = {\rm g}\mu_{\rm B}\langle S\rangle$. Therefore, the PM phase becomes stable with increasing field. If the Zeeman term $M_{3d}H$ has a predominant effect in the M-I transition, the anisotropy of $H_{\rm MI}$ is determined by that of the g-factor of the $3d$ spins. Therefore, $H_{\rm MI}$ will have sinusoidal dependence as a function of the angle, as shown in Fig. 30.

The M–I transition field $H_{\rm MI}(H)$ is maximum for $H \parallel b^*(\theta = 0^\circ)$ in the b^*–c plane [Fig. 30(a)], but the $\tau(\theta)$ curve in the PM phase has the maximum at $\theta \approx 45^\circ$. In the PM phase, the magnetization arises predominantly from the $3d$ spins since the π spins are hardly polarized by the field (almost field-independent).

Assuming the g-factor of the $3d$ spin,

$$ {\rm g}(\theta) = {\rm g}_{\parallel}{\rm cos}^2(\theta - \theta_0) + {\rm g}_{\perp}{\rm sin}^2(\theta - \theta_0), \tag{44} $$

we obtain the magnetization

$$ M_{3d}(\theta) = M_{\parallel}{\rm cos}^2(\theta - \theta_0) + M_{\perp}{\rm sin}^2(\theta - \theta_0), \tag{45} $$

where $M_{\parallel} = N{\rm g}_{\parallel}\mu_{\rm B}S$, $M_{\perp} = N{\rm g}_{\perp}\mu_{\rm B}S$, and N is the spin number. The torque in the PM phase arises mainly from the $3d$ spins, which is written as

$$ \tau_m(\theta) = -\frac{\partial F_{\rm PM}}{\partial \theta} \approx -(M_{\parallel} - M_{\perp})\,{\rm sin}[2(\theta - \theta_0)]. \tag{46} $$

The above relations show that the $M_{3d}(\theta)$ curves are shifted from $\tau(\theta)$ by 45°, as schematically indicated by the dashed curves in Figs. 30(a) and 30(b).

An important feature is that $H_{\rm MI}$ is minimum when $M_{3d}$is maximum in both field rotations. This inverse relationship will provide valuable information in the full understanding of the AFI–PM transition.

2.4 Magnetic torque

The $\tau(\theta)$ curves of the antiferromagnetically coupled $3d$ spins have been investigated in the π–d systems κ-(BETS)$_2$FeBr$_4$[65] and κ-(BDH-TTP)$_2$X (X = FeCl$_4$ and FeBr$_4$).[56] For these salts, since the π spins are in a metallic state, the torque is dominated by the localized $3d$ spins. In the AF phase of the $3d$ spins, the torque vanishes (τ_m= 0) at the principal axis of the magnetization

(magnetic easy axis) but shows a sharp change around the easy axis when the field is close to the spin-flop or metamagnetic transition field. The magnetic easy axis, which is generally determined by the crystal symmetry and the dipole interaction between the localized spins, is independent of both temperature and field. The spin-flop transition field $H_{\rm SF}$ is determined by $H_{\rm SF} = (S/\mu_{\rm B})\sqrt{(D(J-D)}$, where J and D are the exchange interaction and the uniaxial anisotropy parameter of the ligand field, respectively. In λ-$(BETS)_2FeCl_4$, the J value of the π spins is expected to be large ($J_\pi \approx 600$ K) from the molecular orbital calculations,[6] so D is small ($\sim$4 mK) from $\mu_0 H_{\rm MI} = 1.2$ T. Such a small D value will be reasonable in molecular conductors because the spin–orbit coupling is generally very small for molecular orbitals. As the field increases, the sharp change at the easy axis is suppressed and the $\tau_m(\theta)$ curve becomes sinusoidal in the PM phase. In this process, the magnitude of the torque largely changes, but we observe $\tau_m = 0$ at the same angle. This behavior is well understood by the simulation in a simple AF spin structure.[56]

As shown in Fig. 43, however, both $\theta_0^{\rm p}$ and $\theta_0^{\rm n}$ steeply change at $T_{\rm MI}$. Similarly, large $\theta_0^{\rm p}$ and $\theta_0^{\rm n}$ changes as a function of field are observed. As Figs. 30(a) and 41(a) show, $\theta_0^{\rm n}$ at 14 T is about $-90°$, which corresponds to the easy axis of the Fe $3d$ moments. $\theta_0^{\rm n}$ rapidly increases with decreasing field and reaches $-20°$ at 0.5 T. This angle corresponds to the hard axis because a sharp change due to the spin-flop transition is observed at 70° (easy axis) at 1.2 T. A similar large change is observed for $\theta_0^{\rm p}$. For the Ga salt, the torque curve maintains the sinusoidal dependence in the entire temperature and field regions (except the superconducting transition) without changes in the zero-crossing angle. These results clearly show a characteristic magnetic transition of the spin state in the Fe salt, where the π–d interaction plays an essential role. In the PM phase, the torque is dominated by the $3d$ spins. If the $3d$ spins show an AF order but the π spins are paramagnetic in the AFI phase, large changes in $\theta_0^{\rm p}$ and $\theta_0^{\rm n}$ will not be observed. Although a structural change is observed by X-ray measurements below $T_{\rm MI}$,[30] it is unreasonable that the easy axis of the $3d$ spins markedly changes at $T_{\rm MI}$. Therefore, it is concluded that the π spins show an AF order, but the $3d$ spins remain paramagnetic in the AFI phase, as suggested by the specific heat measurements.[32,66]

In Figs. 36 and 37, the torque is almost field-independent above $\sim$10 T, which indicates that the $3d$ spins are saturated by the field. This behavior is consistent with the small AF coupling between the $3d$ spins $J_d = 0.64$ K.[6] As the field decreases, the paramagnetic $3d$ moment M_{3d} decreases, approximately following $M_{3d} \propto H$. Thus, the torque decreases steeply with decreasing field, $\tau \propto H^2$. By contrast, the π spins are hardly polarized along the external field in the AF phase because $J_\pi \approx 600$ K. This suggests that the torque of the π spins is small but enhanced only near $H_{\rm SF}$, as shown in the simulations.[56] Therefore, the torque signal will be dominated by the π spins at low fields, although the π spin number $S = 1/2$ is smaller than the $3d$ spin number $S = 5/2$. In the PM phase, the metallic π spins contribute little to the torque, which is dominated by the $3d$ spins.

Since the magnetic principal axes of the π and $3d$ spins can be different, the zero-crossing angles will change with field and temperature. This concept qualitatively explains the results

shown in Figs. 41 and 43. At $T_{\rm MI}$, a marked change in the zero-crossing angles in Fig. 43 will be reasonable because the field is close to $H_{\rm SF}$. In Fig. 41(a), $\theta_0^{\rm p}$ and $\theta_0^{\rm n}$ moderately change at $H_{\rm MI}$ since the 3d spins are almost fully polarized near $H_{\rm MI}$. As the field decreases, the 3d spin torque decreases and the π spin torque becomes dominant toward $H_{\rm SF}$, which is recognized as crossover behavior. In contrast to $\theta_0^{\rm p}$ and $\theta_0^{\rm n}$, $\phi_0^{\rm p}$ and $\phi_0^{\rm n}$ are almost constant above 4 T, but the anomalous behavior is seen at $\sim$4 T [Fig. 41(b)]. The result will be mainly caused by the sign of the signal below 4 T, suggesting a similar crossover from the 3d- to π- spin-dominant regions.

Here, we note that the zero-crossing angles for the Ga salt are different from those for the Fe salt at low fields in the AFI phase, although the torque is dominated by the π spins in both salts. The principal axes of magnetization, corresponding to the zero-crossing angles, are generally determined by the crystal symmetry, which reflects the charge distribution around the spin. NMR studies[62] indicate a charge disproportionation in the BETS layer in a wide temperature range for both salts. The amplitude of the disproportionation for the Fe salt is about twice that for the Ga salt, which could lead to different zero-crossing angles for both salts. In addition, the 3d spin produces large internal field H_π on the π spins via $J_{\pi d}$ in the Fe salt. The field H_π is not necessarily parallel to the external field, which changes the zero-crossing angles. Recent specific heat measurements suggest that the internal field of the 3d spins becomes inhomogeneous above $\sim$4 T.[66] The microwave absorption increases considerably above $\sim$4 T.[15] These anomalies may also be related to the change in the zero-crossing angles in Figs. 41 and 43.

2.5 Magnetocaloric effect

When the second term is dominant in Eq. (41), the magnetic entropy is approximately written as,

$$S_m\left(H\right) \approx -\frac{\kappa}{T v_H} \int_0^H \Delta T\left(H\right) dH + S_m\left(H=0\right) \tag{47}$$

In the MCE measurements, $S_m(H=0)$ is unknown. For simplicity, the $S_m\left(H\right)$ curves in Fig. 49 are shifted so that the entropy coincides with that obtained from the specific heat at 8 T. The field dependences agree reasonably with each other. Each $S_m(H)$ curve shows a broad maximum at $\sim$2 T and then decrease with increasing field. A hump observed at $H_{\rm MI}$ is due to the M–I transition. We note that the S_m approaches to zero with increasing field at 1.5 K, which indicates that the 3d spins are aligned along the field almost completely.

In contrast to the sharp large dip arising from the AFI–PM transition, we observe a small sharp peak at $\sim$1.2 T due to the spin-flop transition. At $H_{\rm SF}$, we observe the positive peak $\Delta T > 0$ for the up sweep, showing a negative entropy jump $\Delta S_m < 0$. Since the magnetization should have a positive jump $\Delta M > 0$ at $H_{\rm SF}$, we obtain $dH_{\rm SF}/dT > 0$ from the Clausius–Clapeyron equation,

$$\frac{\Delta S}{\Delta M} = \frac{dH_{\rm SF}}{dT}. \tag{48}$$

We see the $dH_{\rm SF}/dT > 0$ behavior slightly in Fig. 45. The relation $dH_{\rm SF}/dT > 0$ is a common feature for AF systems.

For a typical AF metal κ-(BETS)$_2$FeBr$_4$, the MCE in Fig. 50 is understood as follows. The magnetic entropy of κ-(BETS)$_2$FeBr$_4$ is predominantly determined by the localized $3d$ spins in the entire temperature and field regions because the π electrons remain in the metallic state. At $H_{\rm M}$, the $3d$ spins suddenly change from the AF phase (low entropy phase) to the PM phase (high entropy phase), $\Delta S > 0$, which leads to a negative dip in the ΔT curve. The magnetization should have a positive jump $\Delta M > 0$ at $H_{\rm M}$ and we see $dH_{\rm M}/dT < 0$ (inset of Fig. 50), consistent with the Clausius–Clapeyron equation.

In the PM phase above $H_{\rm M}$, the $3d$ spins are gradually aligned along the field with increasing field; the entropy decreases with increasing field ($\Delta T > 0$) and finally $\Delta T \to 0$. In the molecular field approximation, the magnetization in the paramagnetic state is given by

$$< M >= S B_J\left(x'\right) N, \tag{49}$$

$$B_J\left(x'\right) = \frac{2J+1}{2J}\coth\left(\frac{2J+1}{2J}\right) + \frac{1}{2J}\coth\left(\frac{1}{2J}\right), \tag{50}$$

$$x' = \frac{g\mu_{\rm B}S}{k_{\rm B}T}\left(H - H_{\rm int}\right) = \frac{g\mu_{\rm B}S}{k_{\rm B}T}\left(H - Jz < S >\right), \tag{51}$$

$$\frac{d < M >}{dT} = \frac{dS_m}{dH}. \tag{52}$$

Here, J is the antiferromagnetic interaction between the $3d$ spins and z is the number of the nearest neighbor sites ($z = 2$).

The simulated S_m and $-dS_m/dH$ curves are presented in Fig. 53. The peak of the $-dS_m/dH$ curve is suppressed and shifts to a high field as the temperature increases. The MCE curves above $H_{\rm M}$ seem reasonably reproduced by the simulation.

The ΔT curves λ-(BETS)$_2$FeCl$_4$ (Fig. 44) are much more complicated than those of κ-(BETS)$_2$FeBr$_4$. The specific heat studies in λ-(BETS)$_2$FeCl$_4$ show that the π spins are ordered in the AFI phase, which create an internal field at the $3d$ spin sites via the π–d interaction $J_{\pi d}$. Although the direction of $H_{\rm int}$ is an unknown parameter, we could expect the magnetic entropy of the $3d$ spins to monotonically decrease with increasing field, following Eq. (41). Therefore, the ΔT curve arising from the $3d$ spins will only have a broad maximum somewhere, as shown in Fig. 54(a). In the PM phase, only the $3d$ spins predominantly contribute to the entropy. We expect ΔT to monotonically decrease down to zero with increasing field. The behavior will be similar to the result above H_M for κ-(BETS)$_2$FeBr$_4$.

The π spins first show the spin-flop transition ($\Delta S < 0$) at 1.2 T, where a sharp peak appears in the ΔT curve [Fig. 54(b)]. Thereafter, the entropy of the π spins gradually decreases. At $H_{\rm MI}$, the spin entropy would show a discontinuous increase because of the first order phase

transition, which leads to a sharp dip in the ΔT curve. In the PM phase, the entropy of the π spins depends little on the fields; $\Delta T \approx 0$.

The total ΔT curve is approximately given by the sum of the two curves. At high temperatures above 3 K, the MCE can be qualitatively explained by the abovementioned concept. However, we can not explain the broad dip at 5 T, which is evident only at low temperatures.

At ∼5 T, an anomalous behavior has been reported in various measurements. The saturated value of the bias-dependent polarization with frequency $F = 44$ GHz steeply increases above 5T at 4.2 K.[31] The dielectric constant with $F = 1$ KHz increases above 5 T at 1.6 K.[48] The nonlinear I–V characteristics are strongly suppressed above 7 T at 1.6 K.[48] These results show that the π electron charges are strongly fluctuated in the BETS layers above 5 T. On the other hand, the microwave absorption with $F = 44$ GHz at 1.5 K is enhanced between 4.1 T and 5 T at low temperatures, and the width of the absorption signal shows an anomalous peak at ∼4.5 T.[15] These results show some change in a collective (not a single) spin excitation. Therefore, if all these anomalies arise from the same origin, it is very likely that both π electrons and spins are ordered in the AFI phase and show anomalous collective responses to external fields.

The specific heat measurements show that the internal field at the Fe site becomes inhomogeneous above 5 T.[66] In the magnetic torque measurements, a marked change in the anisotropy is observed at ∼5 T.[63] These results show certain change in the spin structure.[66] An interesting point is that the internal field at the π electron site created by the Fe $3d$ spins is estimated as ∼4.5 T.[66] Because the MCE directly reflects to the entropy of the spins and charges, the broad dip at 5 T should be closely related to the above collective excitations of the π charges and spins. The broad (not sharp) dip at 5 T in the MCE suggests a crossover rather than a phase transition.[63] Further investigation will be required to clarify the detailed mechanism of the anomalies at 5 T.

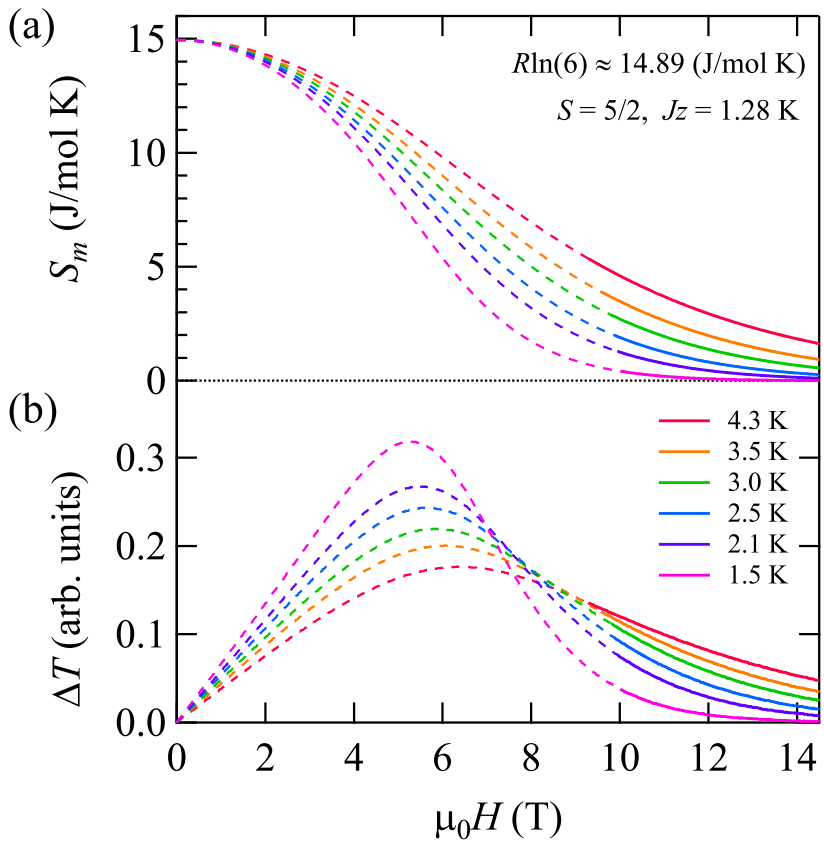

Figure 52: Simulated magnetic entropy of the paramagnetic 3d spins S_m and ΔT for $Jz = 1.28$ K.

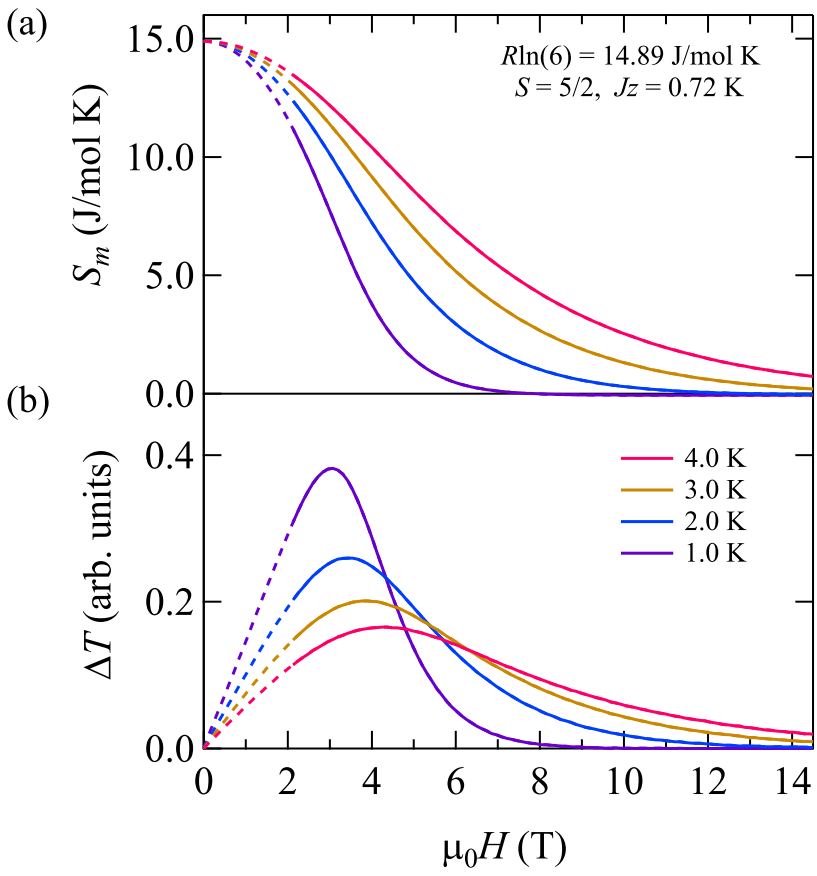

Figure 53: Simulated magnetic entropy of the paramagnetic $3d$ spins S_{m} and ΔT for $Jz = 0.72$ K.

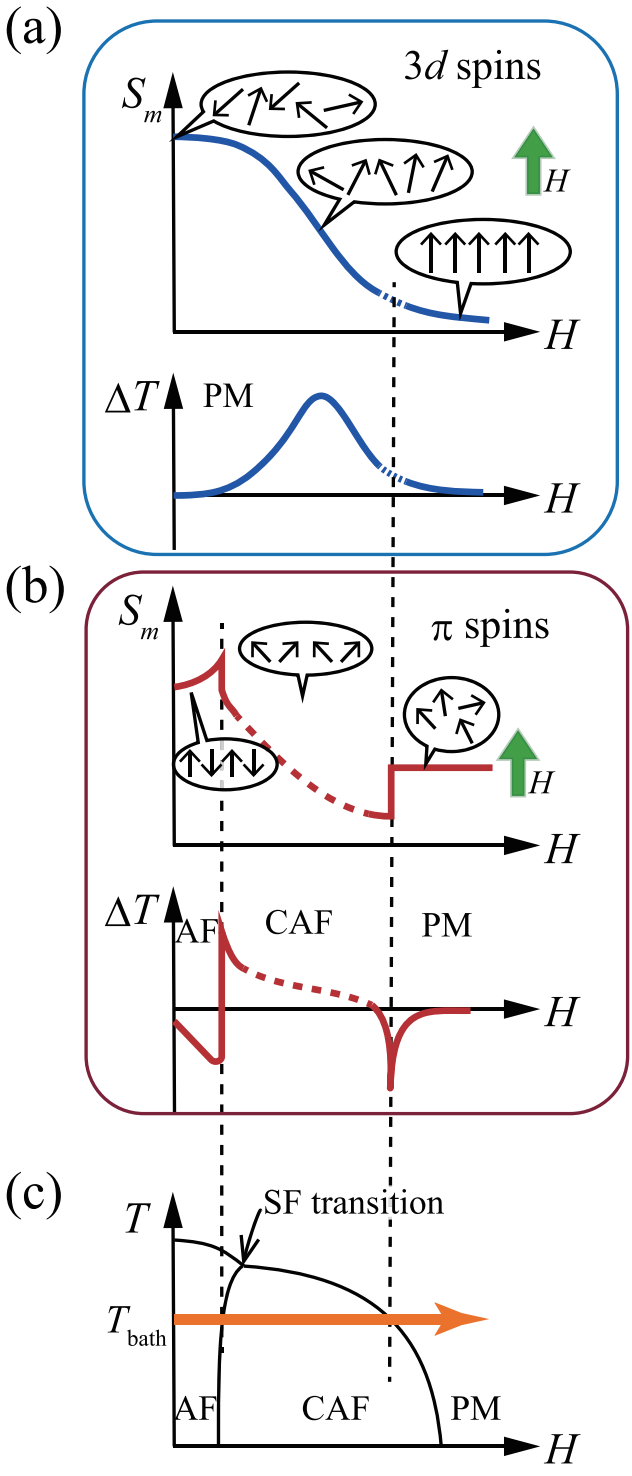

Figure 54: Schematic illustration of magnetic entropy and ΔT curves in (a) $3d$ and (b) π spins. (c) Temperature–magnetic field phase diagram for λ-$(BETS)_2FeCl_4$.

Chapter 3

Conclusion

The nonlinear I–V characteristics in the AFI phase of λ-$(BETS)_2FeCl_4$ are interpreted on the basis of the charge transport due to thermally excited electron–hole pairs in the 2D Coulomb potential. In the $R(H)$ curve, a small dip at 1.2 T can be ascribed to the spin-flop transition. This dip is likely caused by the spin-dependent excitation of the charges based on the model explained above. The dielectric constant at low frequencies is anisotropic; $\varepsilon_{\rm in}$ is 10 times larger than $\varepsilon_{\rm out}$. This anisotropy is consistent with the presence of the 2D Coulomb potential.

The $H_{\rm MI}$ values in the b^*–c and b^*–a' planes show a sinusoidal behavior as a function of the field angle. The sinusoidal angular dependence of $H_{\rm MI}(\theta)$ is determined from the $\tau_m(H)$ curves, which is consistent with that from the $R(H)$ curves. The phase factor of $H_{\rm MI}(\theta)$ differs from that of $\tau_m(\theta)$ in the PM phase by 45°, and $H_{\rm MI}$ is maximum when M_{3d} is minimum. This inverse relationship between $H_{\rm MI}$ and M_{3d} suggests that the Zeeman effect of the 3d spins of the Fe ions plays an essential role. The temperature and magnetic field dependences of the zero-crossing angles of the $\tau_m(\theta)$ curves show the AF order of the π spins but the paramagnetic state of the 3d spins in the AFI phase, which is consistent with the specific heat measurements.[32,66]

As the field increases, the MCE and magnetic torque consistently show the characteristic changes at the spin-flop and AFI–PM transitions. The overall field dependence of ΔT above 3 K is qualitatively interpreted on the assumption of the AF π spins and paramagnetic 3d spins at the Fe sites. However, we find that the broad dip in the ΔT curve appears at ∼5 T below ∼3 K, which is not explained by the above-stated concept. Since anomalies have been observed at ∼5 T in various magnetic and electric properties, the origin should be related to both charge and spin degrees of freedom. No sharp feature in the ΔT curve at ∼5 T shows a crossover rather than a phase transition.

Part IV

High magnetic field phase diagram in the organic layered superconductor β''-(BEDT-TTF)$_2$SF$_5$CH$_2$CF$_2$SO$_3$

Chapter 1

Experimental results

1.1 Magnetic torque measurements

Figure 55 shows the field dependence of the magnetic torque at various temperatures for β"-(BEDT-TTF)$_2$SF$_5$CH$_2$CF$_2$SO$_3$ (β"-SF$_5$ salt) when the magnetic field is almost parallel to the layers ($\theta = -0.1^\circ$). The torque per unit volume is defined as $\tau_m = \mu_0 \mathbf{M} \times \mathbf{H}$, where $\mathbf{M}$ is the magnetization. For highly 2D layered superconductors in nearly parallel magnetic fields, the torque is described as

$$\tau_m = -\mu_0 M_z H_x \ , \tag{53}$$

where the $x(z)$ direction is parallel (perpendicular) to the conduction layers. Thus, one can obtain the perpendicular magnetization M_z from τ_m / H_x where $H_x = H\cos(\theta)$. Each torque curve exhibits a hysteresis between the up and down sweeps of the magnetic field, where the irreversibility fields ($H_{\rm irr}$) can be defined (inset). The irreversible torque curve is caused by the strong pinning of the magnetic fluxes in the superconducting layers. The critical field $H_{\rm c2}$, which should be slightly larger than $H_{\rm irr}$, can not be determined without ambiguity because of the smooth variation above $H_{\rm irr}$. The $H_{\rm irr}$ value decreases with increasing temperature.

Figure 56(a) shows the torque curves at various field angles (θ) at 30 mK. The hysteresis is reduced and $H_{\rm irr}$ decreases as the field is tilted from the parallel direction.

In nearly perpendicular fields, we clearly see de Haas–van Alphen oscillations [Fig. 56(b)]. The result indicates clean limit superconductivity, which is required for the FFLO phase. The frequency of the oscillation ($F \approx 200$ T) is consistent with previous results.[89)]

Inset of Fig. 57 shows typical torque curves as a function of the field angle. The magnetic fluxes are pined in the superconducting layers, leading to a hysteresis between the different field rotations The average of the two rotation curves, indicated by the black curve, gives the $M_z(H_z)$ curve without the pinning effect. The main panel of Fig. 57 shows the averaged torque curves at various fields. The slope of the torque curve at $\theta = 0^\circ$ gives the diamagnetic susceptibility $-dM_z/dH_z$. As the field increases, the diamagnetic signal is reduced.

Figure 58 presents the perpendicular diamagnetic susceptibility $-dM_z/dH_z$ as a function of field at various temperatures, obtained from the angular dependence of the torque (Fig. 57).

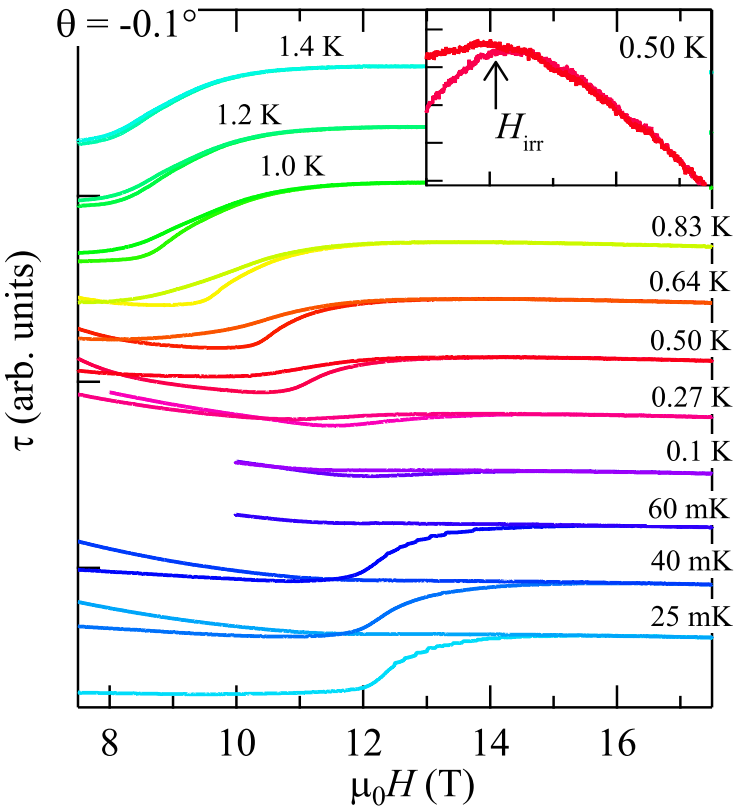

Figure 55: Magnetic field dependence of the magnetic torque at various temperatures. The irreversibility field ($H_{\rm irr}$) is defined in the inset.

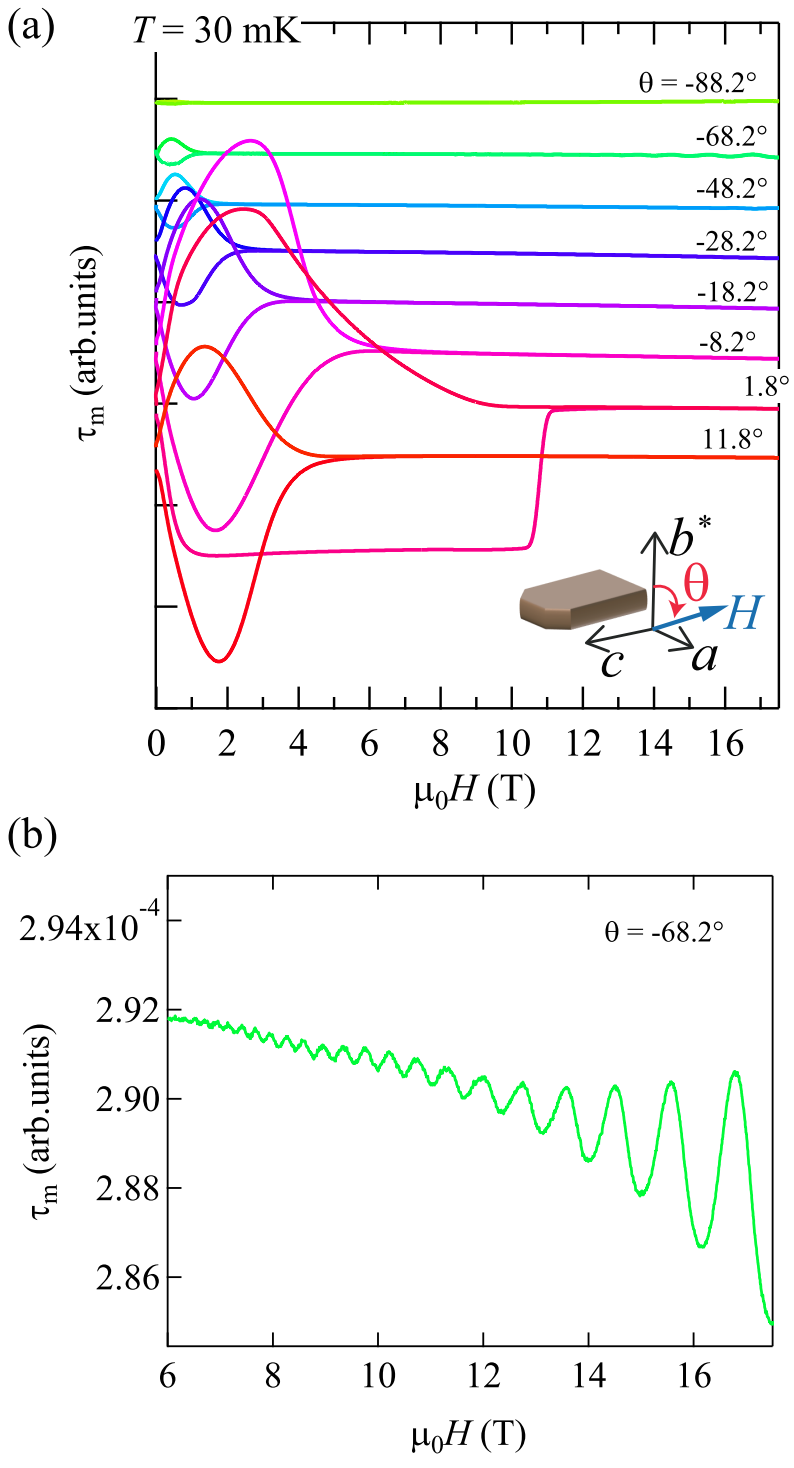

Figure 56: Magnetic field dependence of the magnetic torque at various field angles.

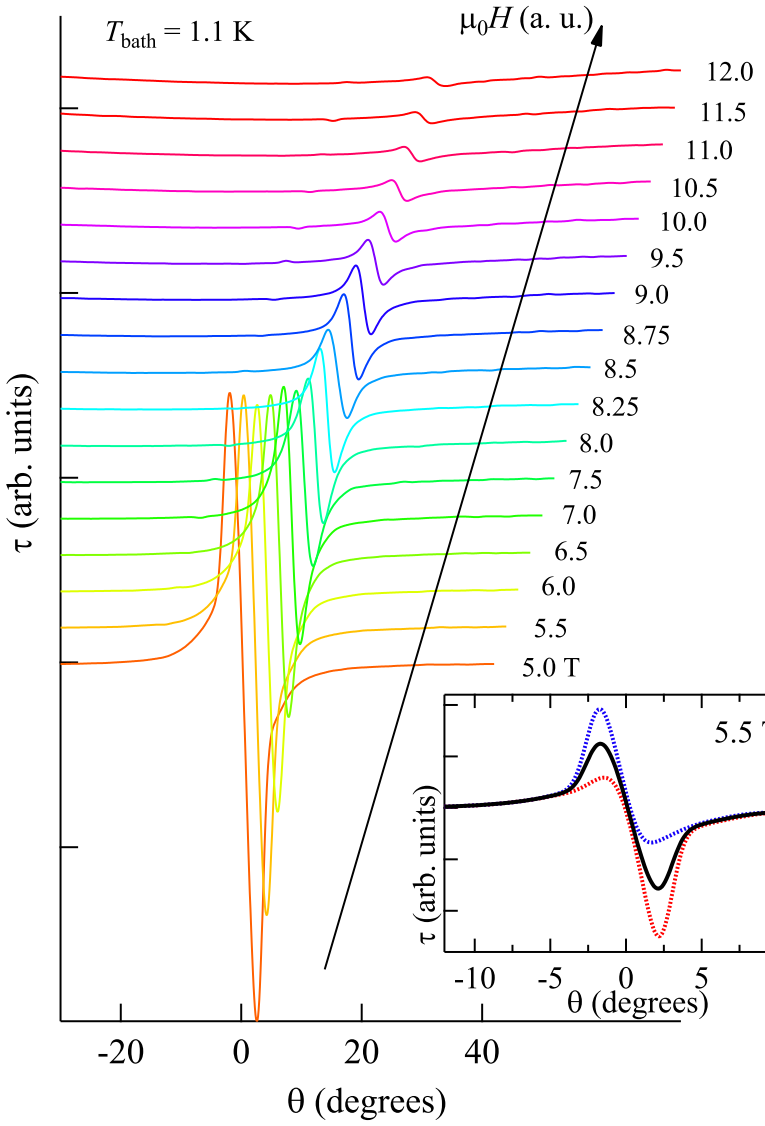

Figure 57: (a) Magnetic torque curves in various magnetic fields at 1.1 K. Inset shows the torque curves at 5.5 T. (b) The $-dM_z/dH_z$ value is obtained from the angular dependence of the torque curve. Arrows indicate the kink fields H_{kink}.

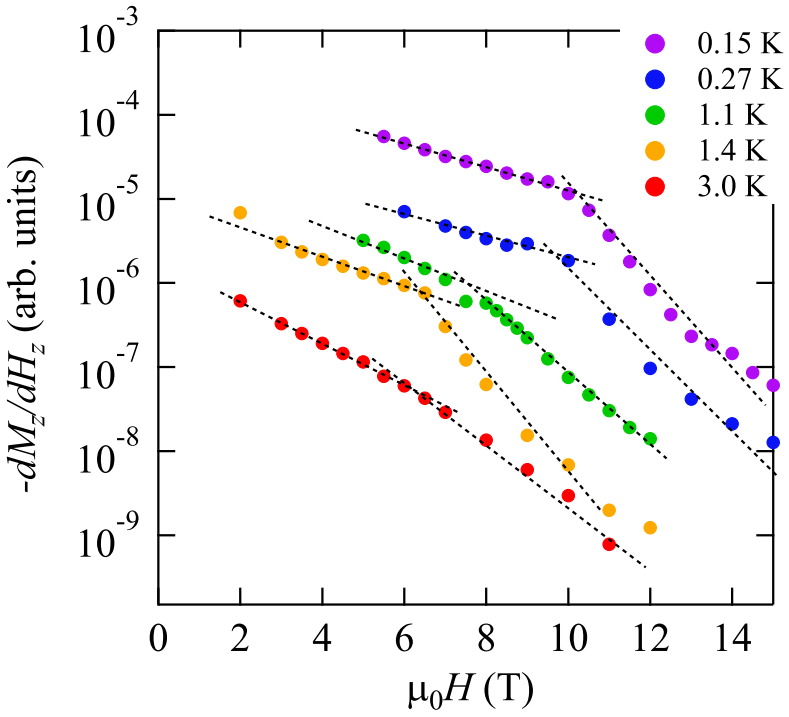

Figure 58: Perpendicular diamagnetic susceptibility $-dM_z/dH_z$ as a function of field at various temperatures.

The diamagnetic signals at all temperatures decrease with increasing field, which are associated with kinks indicated by arrows. The kink field $H_{\rm kink}$ is lower than $H_{\rm irr}$ for $T \leq 1.1$ K, which corresponds to the FFLO transition, as will be shown later.

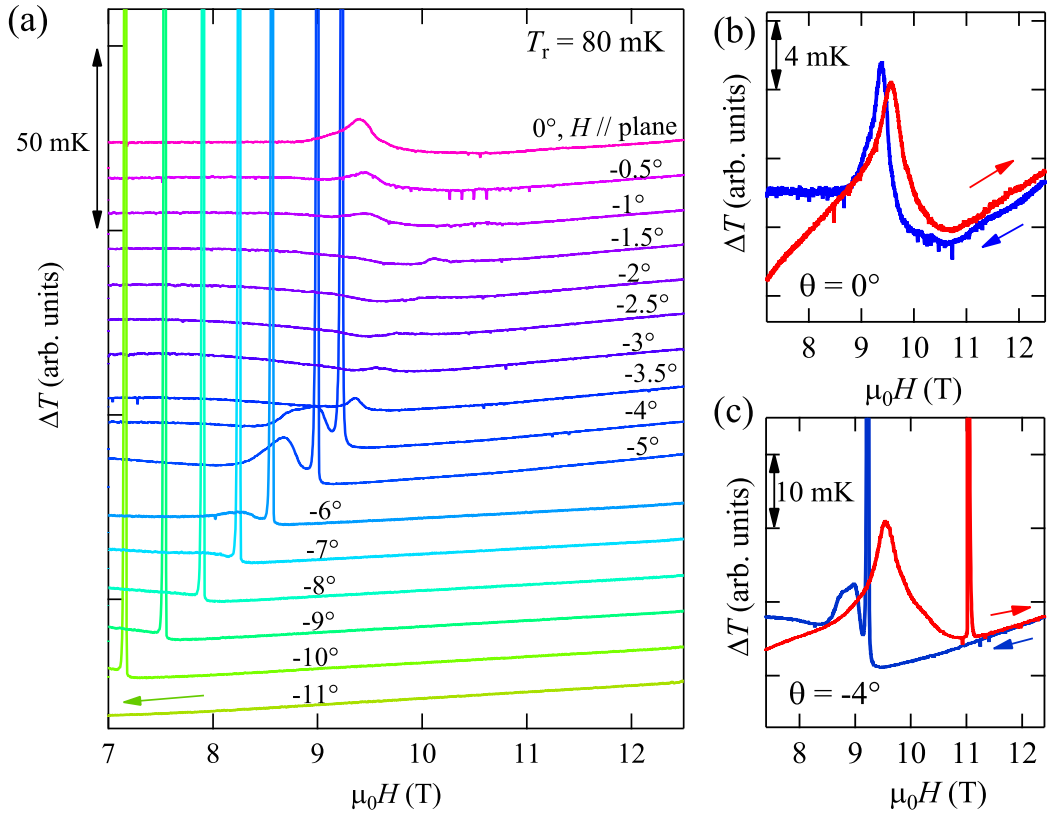

Figure 59: (a) MCE as a function of magnetic field at various field angles θ. Three series of peaks are observed. (b) A broad peak at $H_{\rm peak1}$ is observed only in a limited angle region. (c) The sharp and broad peaks, denoted by $H_{\rm peak2}$ and $H_{\rm peak3}$, respectively.

1.2 Magnetocaloric effect

Figure 59(a) shows the MCE in the down-sweep at various magnetic field angles θ for the reference temperature $T_{\rm r} = 80$ mK. The MCE ΔT is given by Eq. (41). The first term shows thermal relaxation with a time constant $\tau = C/\kappa$, where C and κ are the heat capacity of the sample and addenda, and the thermal conductance between the sample and heat bath, respectively.

In the ΔT curves, we note three series of peaks. Only in a limited angle region ($|\theta| \lesssim 1.5°$), a broad peak ($H_{\rm peak1}$) is observed at ~ 9.5 T, which is associated with small hysteresis between the up and down sweeps [Fig. 59(a)]. In general, ΔT changes the sign between the up and down sweeps due to the dH/dt term in Eq. (41). However, supercooling and superheating processes lead to positive ΔT for both sweeps, which is caused by the supercooling and superheating processes in a first-order phase transition.

Figure 60 depicts the schematic free energy curves of phases A and B as a function of field. The two curves cross at $H_{\rm c}$, where a first order phase transition occurs. If the second term

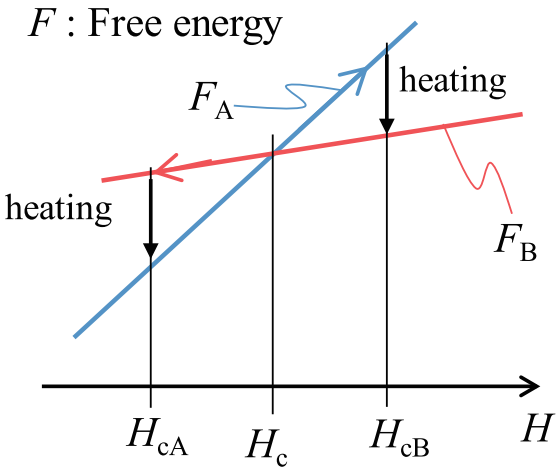

Figure 60: Schematic illustration of the free energy curves of two different phases.

in Eq. (41) is dominant, ΔT changes the sign between the up and down sweeps because of the dH/dt term. At a first order phase transition, supercooling and superheating occur for the down and up sweeps, respectively. These processes lead to a hysteresis between the up and down sweeps, resulting in the transitions at $H_{\rm cA}$ and $H_{\rm cB}$. If the supercooling and superheating effects are dominant, we observe positive MCE ($\Delta T > 0$) peaks at both $H_{\rm cA}$ and $H_{\rm cB}$.

As shown later, the peak at $H_{\rm peak1}$ is ascribed to the FFLO transition. Since the periodic nodal line structure is formed in the FFLO phase, the vortices will be reconfigured in the sample, which also causes heating for both sweeps.

When the field is tilted from the superconducting layers, we observe other two series of peaks associated with hysteresis, sharp and broad ones, which are denoted by $H_{\rm peak2}$ and $H_{\rm peak3}$, respectively [Fig. 59(c)]. Similarly, both the peaks are ascribed to first-order phase transitions. We note that $H_{\rm peak2}$ and $H_{\rm peak3}$ show rapid increases as $\theta \to 0°$. The broad peak is observed at a lower field than the sharp peak. As $\theta \to 0°$, the intensity is suppressed but still visible at $\theta \approx 0°$. The sharp peak at $H_{\rm peak2}$ suddenly vanishes at $\theta = -3.5°$. Similar angular dependence is observed at 1.7 K.

Figure 62 shows the ΔT curves at various temperatures for $\theta = -0.4°$. With increasing temperature, the peak field $H_{\rm peak2}$ gradually decreases and the intensity is suppressed. When the field is perpendicular to the layer, we observe successive sharp spikes (rapid heating) due to flux jumps below $H_{\rm c2}$ and quantum oscillations (QOs) in the high field normal state. The flux jumps are associated with precursor oscillations and overshoot cooling (61), which are clearly distinct from the peaks at $H_{\rm peak1}$, $H_{\rm peak2}$, and $H_{\rm peak3}$.

Figure 63(a) presents the angular dependence of $H_{\rm irr}$ from the torque, and $H_{\rm peak1}$, $H_{\rm peak2}$, and $H_{\rm peak3}$ obtained from the MCE measurements. The $H_{\rm irr}$ value rapidly increases as $\theta \to 0°$, corresponding to the cusp behavior of $H_{\rm c2}$.[94] The magnetic field–temperature phase diagram

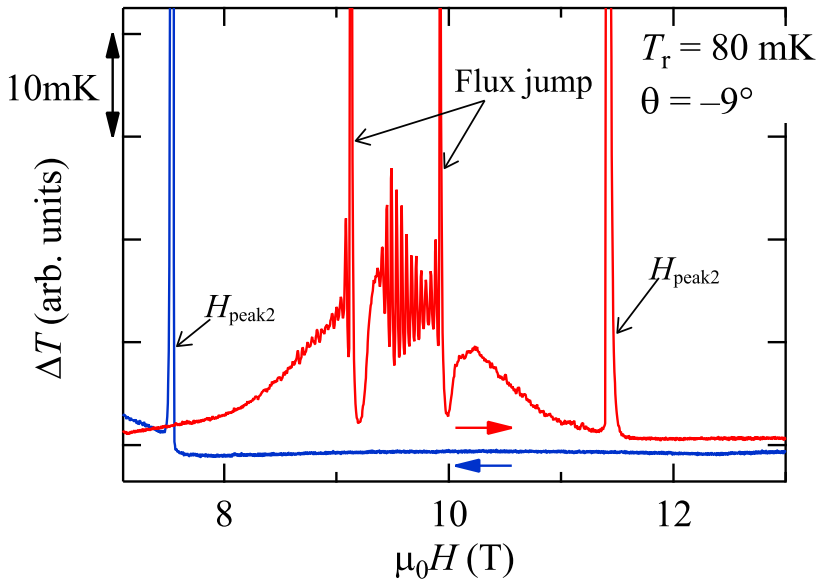

Figure 61: MCE as a function of the magnetic field at 80 mK for θ = -9°. Red and blue curves show the up and down sweeps, respectively.

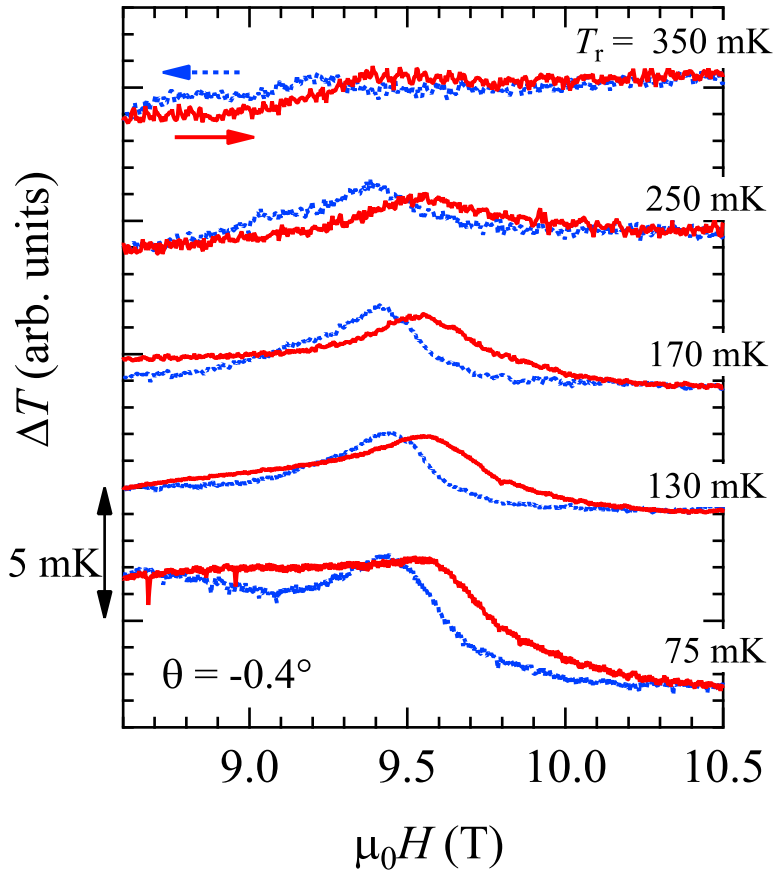

Figure 62: MCE as a function of the magnetic field at various temperatures.

is presented in Fig. 63(b), where $H_{\rm irr}$, $H_{\rm kink}$, and $H_{\rm peak1}$ are plotted. Below ∼0.7 K, $H_{\rm peak1}$ agrees with $H_{\rm kink}$, and both have a tendency to decrease with increasing temperature. $H_{\rm kink}$ rapidly decreases above ∼2 K, and then approximately coincides with $H_{\rm c2}$ above ∼2 K.[73] Since $H_{\rm irr}$ gives a lower limit of $H_{\rm c2}$, we can conclude that there exists a phase boundary in the superconducting phase.

The observation of $H_{\rm peak1}$ in a very limited angle region [Fig. 63(a)] is consistent with the scenario of the FFLO transition; the FFLO phase is strongly destabilized by the orbital effect. The field dependence of the RF response (RF change of a tunnel diode oscillator) shows an anomaly at ∼10.5 T for T = 0.45 K.[74] The ^{13}C NMR measurement shows a kink at ∼9.3 T in the relaxation rate for T = 0.13 K.[75] These features are interpreted as the FFLO phase transition, approximately consistent with the MCE peak at $H_{\rm peak1}$.

Figure 64(a) shows the MCE at 1 K for the field perpendicular to the conducting planes. We clearly see the QOs. Sign inversion of the ΔT curves are observed between the up and down sweeps, which is caused by the second term in Eq. (41). The Fourier transform spectrum of the oscillations is presented in Fig. 64(b) . We observe the fundamental oscillation with $F \approx 200$ T and its harmonics. The angular dependence of the quantum oscillation frequency is shown in Fig. 65, which is well fitted by $1/\cos\theta$. (Fig. 66) The $1/\cos\theta$ dependence clearly shows the presence of the 2D Fermi surface. These results are consistent with results of the de Haas–van Alphen effect in the magnetic torque measurements and previous reports.[89]

Figure 67 shows the field dependence of the MCE at 1.7 K for various field angles. Except for $\theta \approx 0°$, a sharp dip/peak is observed for the up/down sweep. The sign reversal between the two different field sweeps shows that the sharp signals arise not from the flux jumps but from the melting transition of the PVs.

In addition, the dip/peak in the up/down sweep clearly shows that the high field phase has high magnetic entropy. At 1.7 K, the MCE peak of the FFLO and JV melting transition can not be observed probably because these transitions broaden due to thermal fluctuations or the signals are below the noise level.

As in the case for $T_r = 80$ mK, t the PV melting transition suddenly vanishes for $|\theta| < 4°$, and a hysteresis is slightly observed.

At zero degree, we observe a small hysteresis up to 9.8 T (indicated by an arrow), which is defined as the irreversibility field ($H_{\rm irr}$). The $H_{\rm irr}$ value decreases as the field is tilted from the superconducting layers.

The angular dependence of the $H_{\rm irr}$ is shown in Fig. 68. We can expect that $H_{\rm irr}$ is slightly lower than $H_{\rm c2}$. Therefore, it will be reasonable to fit the angular dependence of $H_{\rm irr}$ with the anisotropic 3D model and the 2D model, which are, respectively, given by

$$\left[\frac{H_{\rm c2}(\theta)\cos(\theta)}{H_{\rm c2}^{\perp}}\right]^2 + \left[\frac{H_{\rm c2}(\theta)\sin(\theta)}{H_{\rm c2}^{\parallel}}\right]^2 = 1, \tag{54}$$

and

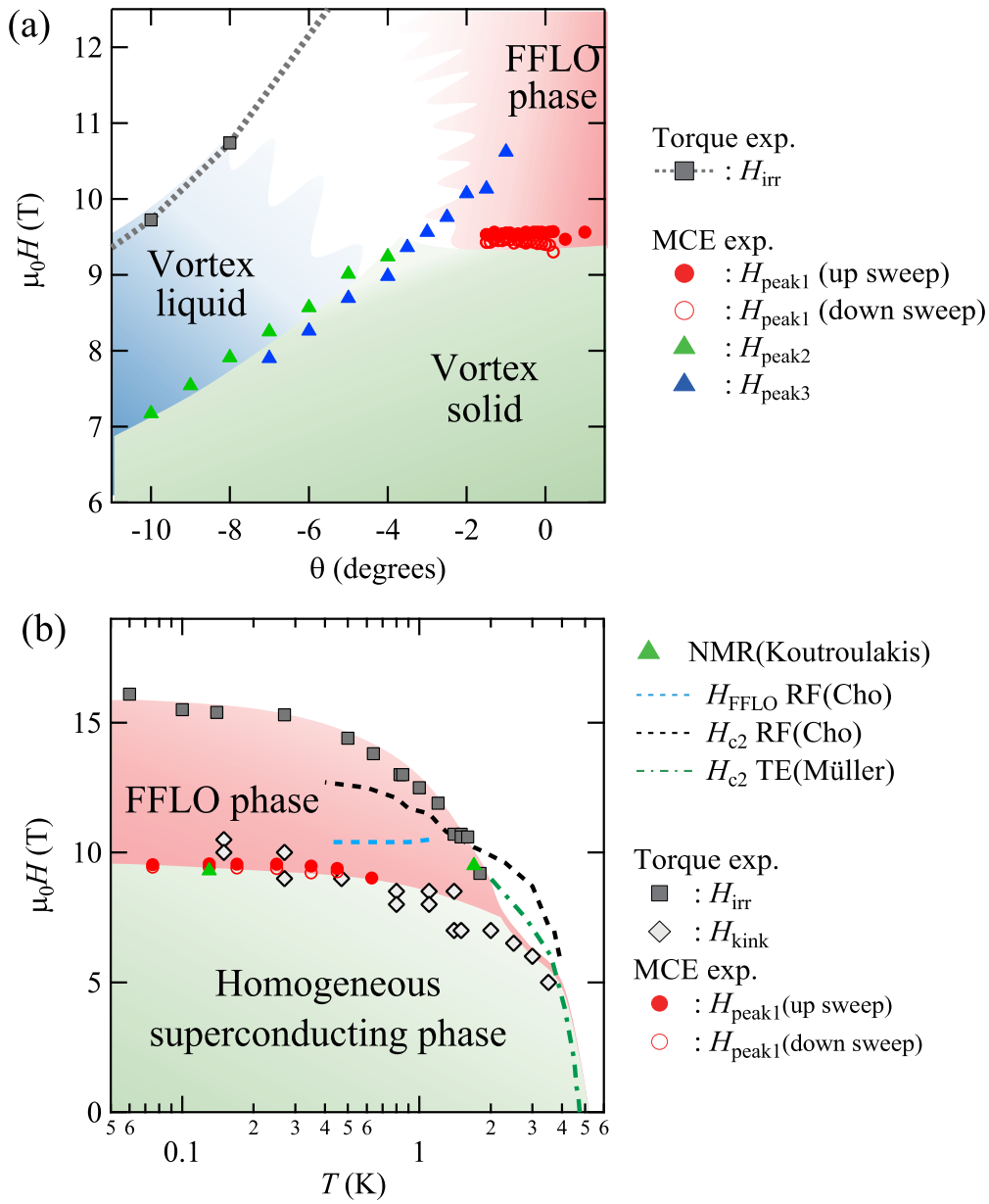

Figure 63: Magnetic phase diagram. (a) $H_{\rm irr}$, from the toque at 30 mK, and $H_{\rm peak1}$, $H_{\rm peak2}$, and $H_{\rm peak3}$ from the MCE at 80 mK are plotted as a function of the field angle. The irreversibility field $H_{\rm irr}$ rapidly increases as $\theta \to 0°$, showing a cusp behavior of H_{c2}. Below $H_{\rm irr}$, three MCE peaks at $H_{\rm peak1}$, $H_{\rm peak2}$, and $H_{\rm peak3}$ arise from the FFLO transition and melting transitions of the PVs and JVs, respectively. (b) $H_{\rm irr}$, $H_{\rm kink}$ and $H_{\rm peak1}$ are plotted as a function of temperature. Below 0.7 K, $H_{\rm peak1}$ agrees with $H_{\rm kink}$, and both have a tendency to decrease with increasing temperature. The FFLO phase boundary decreases with increasing temperature down to ∼8 T at ∼2 K, where a tricritical point is present. For comparison, $H_{\rm FFLO}$ and H_{c2} determined by RF response[74] and thermal-expansion measurements[73] are also plotted.

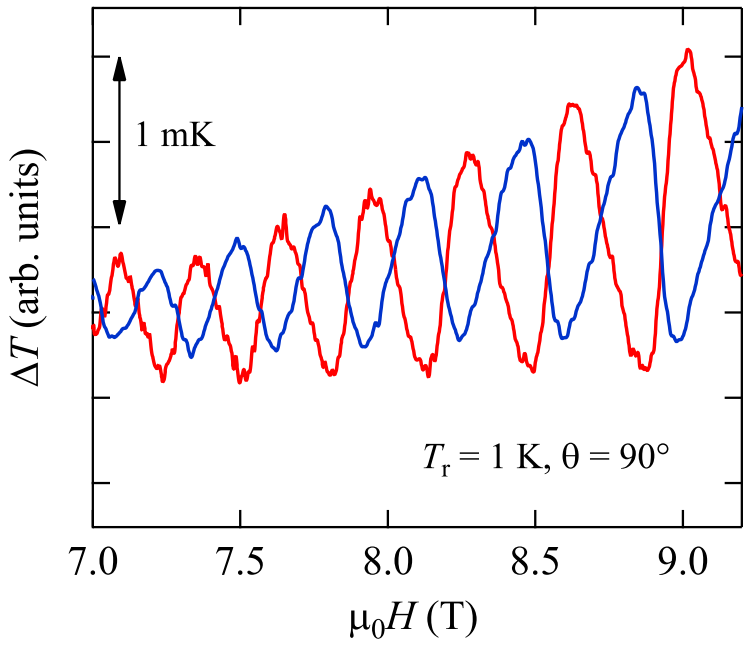

Figure 64: Quantum oscillations in the MCE for up (red) and down (blue) sweeps at $\theta = 90°$ for $T_r = 1$ K.

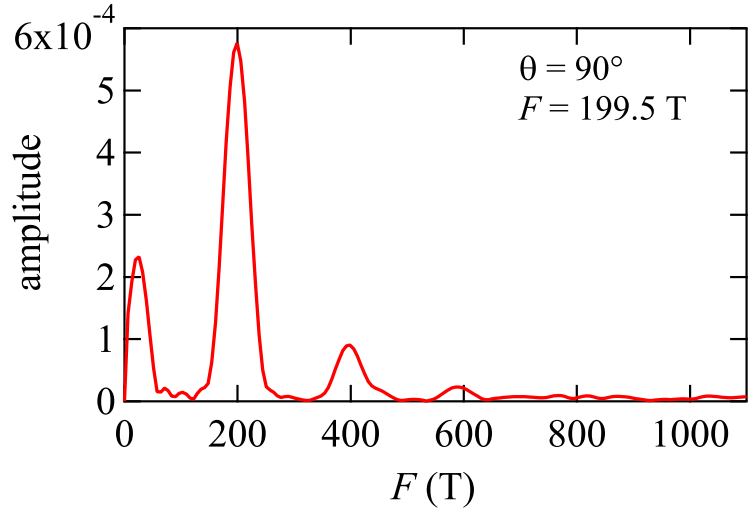

Figure 65: Fourier transform spectrum of the MCE oscillations.

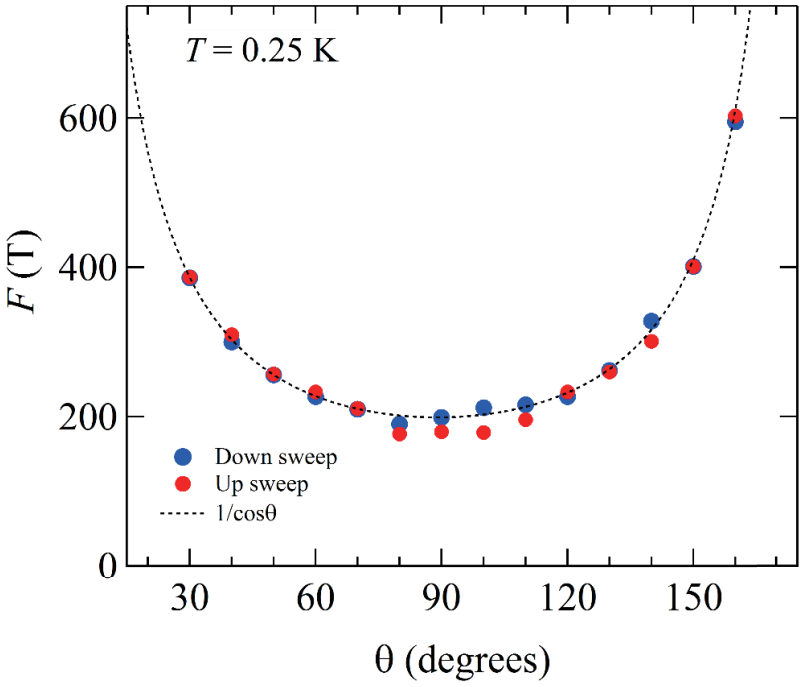

Figure 66: Angular dependence of Fourier transform spectrum.

$$\left|\frac{H_{c2}(\theta)\cos(\theta)}{H_{c2}^{\perp}}\right| + \left[\frac{H_{c2}(\theta)\sin(\theta)}{H_{c2}^{\parallel}}\right]^2 = 1. \tag{55}$$

The blue and red solid curves in Fig. 68 show the calculated results for 3D and 2D models, respectively. In the calculations, we assume $H_{c2}^{\perp} = 1.2$ T and $H_{c2}^{\parallel} = 8.3$ T, which reasonably explain the high angle data. We note that both the curves are significantly lower than that of the experimental data. The disagreement shows that there exists a mechanism increasing H_{c2} at low angels, which is likely due to the FFLO phase.

When the magnetic field exceeds the lower critical field H_{c1} of the type-II superconductors, vortices penetrate the superconducting layers. The Meissner shielding currents, which act on the vortices as a Lorentz force, push vortices into the sample deeper. On the other hand, vortices forming a vortex lattice in the vortex solid state are strongly pinned at defects and the sample edge. Thus, the vortices are formed near the sample surface and cause the field gradient near the sample edge associated with the surface currents. The field gradient induces the current density, and the viscous flow of vortices causes local heating. Then, vortices allow to penetrate the sample deeper, which leads to additional heating. This catastrophic behavior is known as a flux jump.

Figure 69 shows the MCE as a function of magnetic field applied perpendicular to the conducting layers at $T = 85$ mK. The magnetic field was swept at 0.1 T/min. As the field increases, the sample temperature rapidly increases, and then shows successive spikes as shown in the inset of Fig. 69, which are caused by the flux jumps in the vortex solid state. These

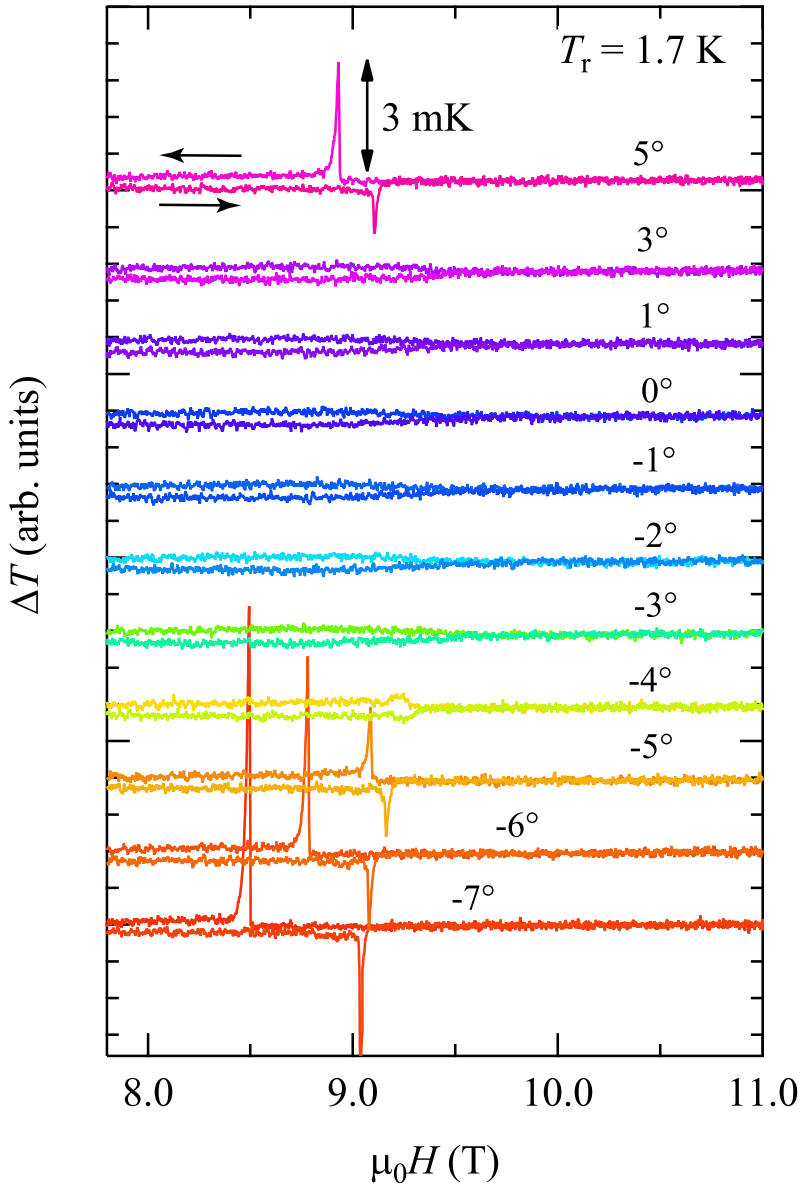

Figure 67: MCE as a function of the magnetic field at various field angles θ for T_r = 1.7 K.

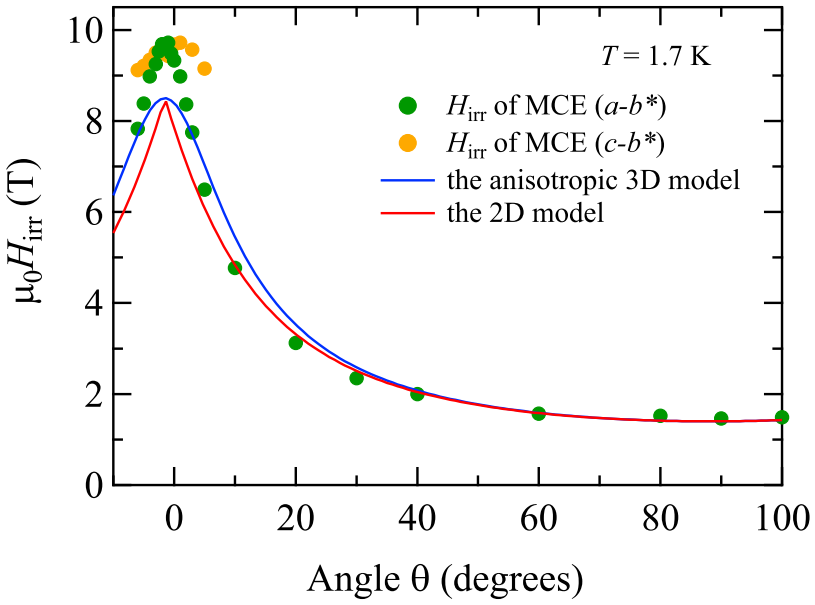

Figure 68: Angular dependence of $H_{\rm irr}$ in MCE at 1.7 K.

ΔT spikes are also observed in the organic superconductor κ-(BEDT-TTF)$_2$Cu(NCS)$_2$.[93] The abrupt cessation of ΔT jumps associated with these instabilities serve as an indication of melting of this quasi 2D vortex lattice phase.

Figure 70 shows the flux jumps measured at different bath temperatures. The temperature spikes arising from the flux jump become smaller as the field increases, and then stop at the melting field at each temperature. The temperature dependence of the melting field obtained from Fig. 70 is shown in Fig. 71.

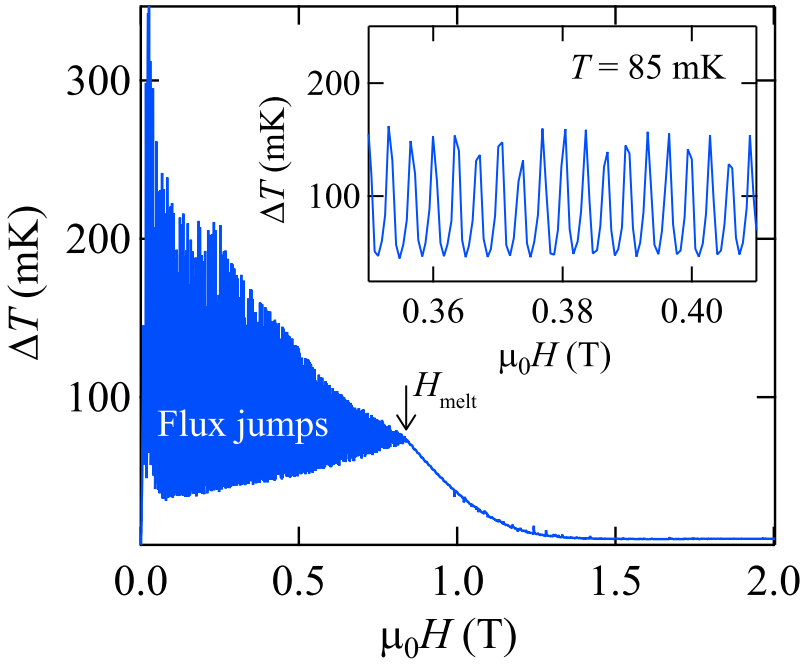

Figure 69: MCE as a function of magnetic field applied perpendicular to the conducting layers at $T = 85$ mK.

1.3 Resistance

Figure 72 shows the temperature dependence of the out-of-plane resistance at $\mu_0 H = 0$ T with a measuring current of $I = 500$ nA. The resistance monotonically decreases with decreasing temperature, and a superconducting phase transition is observed. The resistance onset is ∼5.7 K, and zero resistance occurs at 4.0 K.A This is consistent with the previous studies.[87,91)]

Figure 73(a) shows the field dependence of the out-of-plane resistance at 1.5 K for the magnetic field perpendicular to the conducting layers. The resistance rapidly increases above ∼0.3 T and a sharp maximum at 0.8 T and then a broad minimum at 2.5 T. After that, the resistance gradually increases with field. Above ∼6 T, QOs are clearly seen, which shows that the sample quality is sufficiently high, clean limit superconductivity. The Fourier transform spectrum of the QOs is shown in Fig. 73(b). One fundamental SdH frequency ($F \approx 200$ T) and its harmonic are observed, which is consistent with the previous report.[89)] The Dingle temperature ($T_{\rm D}$) obtained from the QOs is estimated to be ∼1.2 K.

Samples inevitably include impurities or lattice defects or both. When the electrons are scattered by these impurities or defects, the phase coherence of the cyclotron motion is broken, which leads to Landau level broadening. This broadening is given by $\sim \hbar/\tau$, where τ is the scattering time. The reduction in the quantum oscillation amplitude by the scattering, the so-called Dingle reduction factor, is written as $R_{\rm D} = \exp(-Kp\mu T_{\rm D}/H)$. Here, $T_{\rm D}$ is the Dingle temperature, μ is the effective mass ratio $\mu = m_c/m_e$, and $K = 2\pi^2 k_{\rm B} m_e/e\hbar \approx 14.7$. The

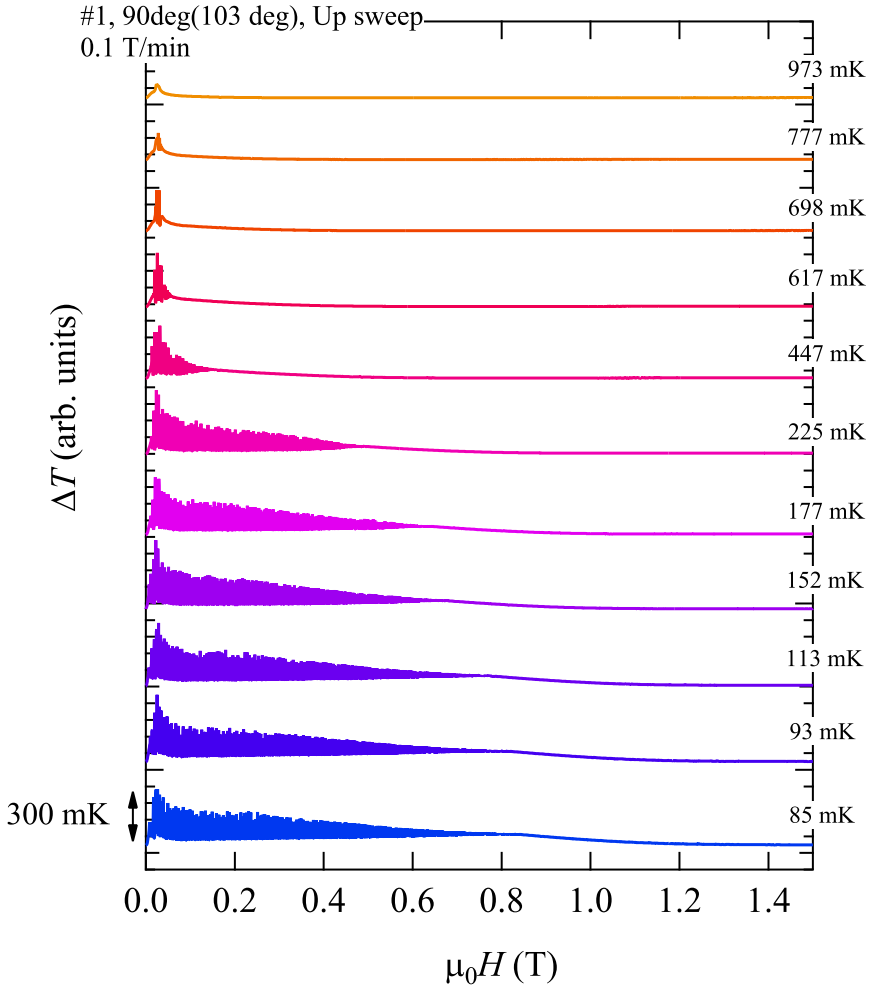

Figure 70: Flux jumps measured at different bath temperatures.

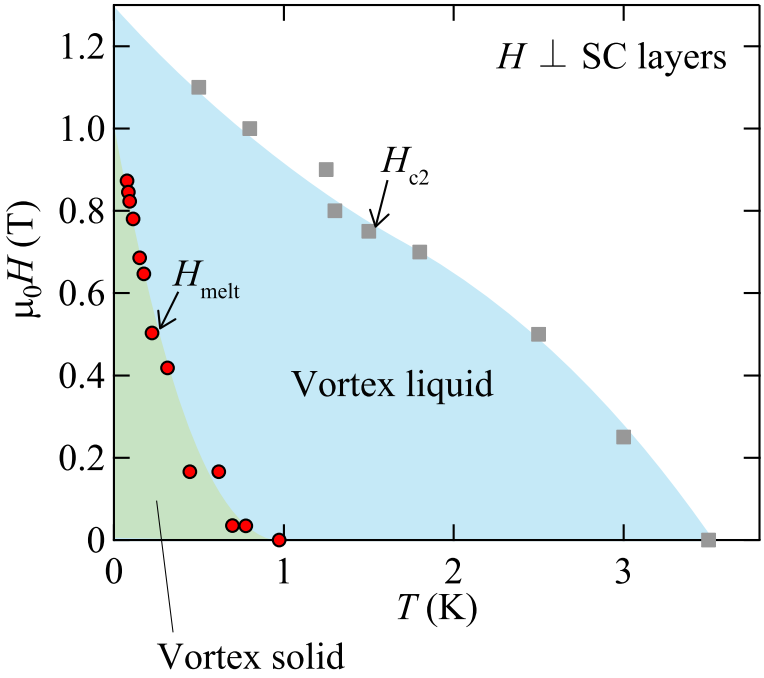

Figure 71: Temperature dependence of the melting field.

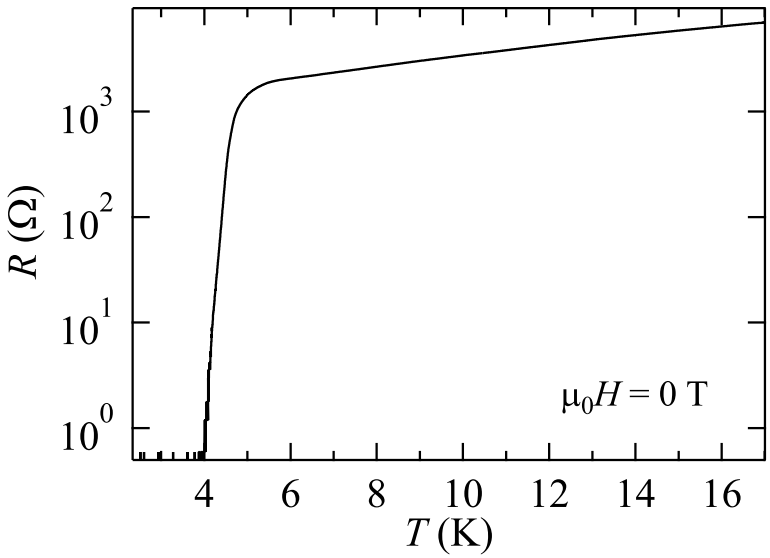

Figure 72: Temperature dependence of out-of-plane resistance at 0 T.

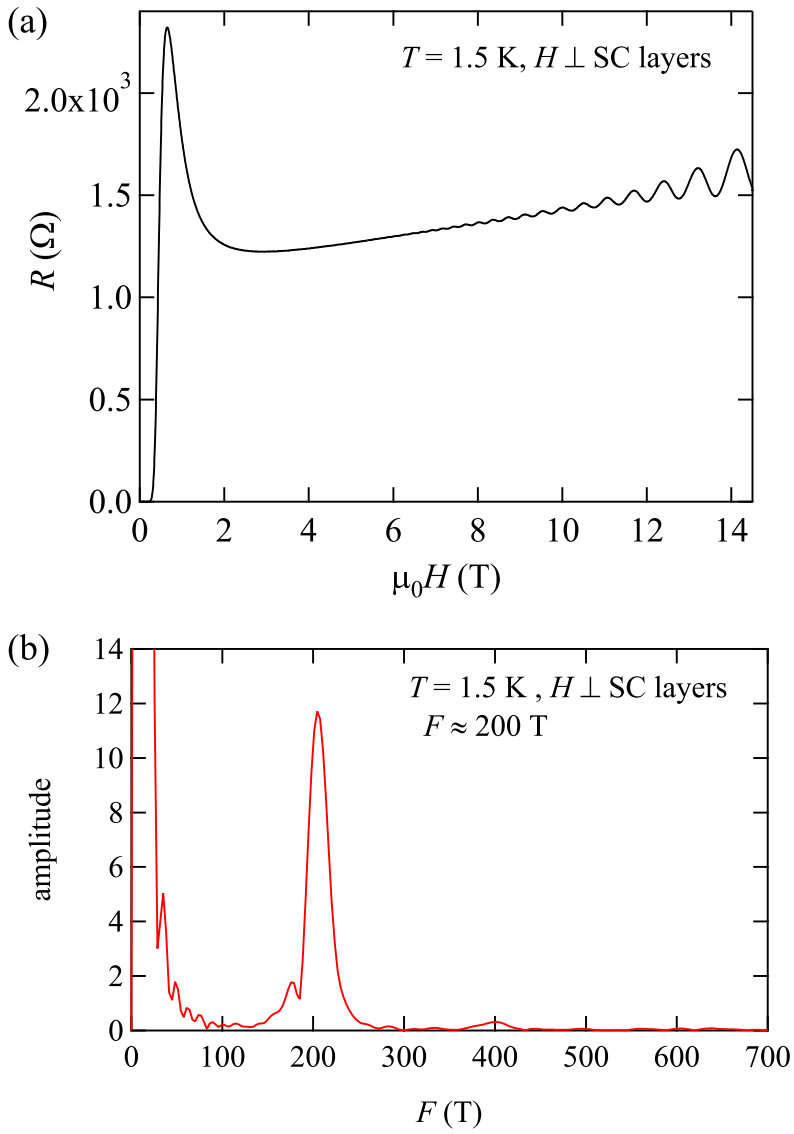

Figure 73: (a) Magnetic field dependence of out-of-plane resistance at $T = 1.5$ K. (b) Fourier transform spectrum of the resistance oscillations. The frequency ($F \approx 200$ T) is consistent with the torque and MCE data.

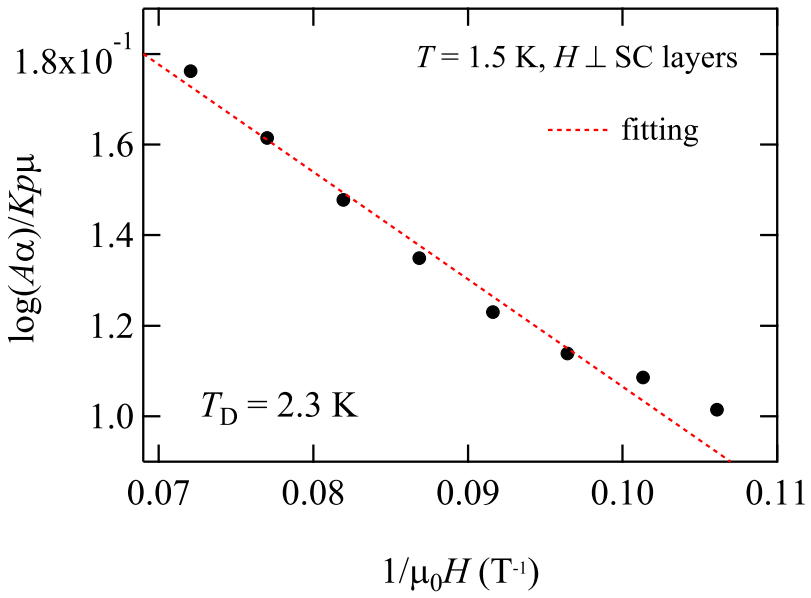

Figure 74: Dingle plots of the SdH oscillations with using Eq. (56).

Dingle temperature $T_{\rm D}$ is a measure of the sample quality, given by $T_{\rm D} = \hbar/2\pi^2 k_B \tau$. $T_{\rm D}$ is estimated by fitting the field dependence of the oscillation amplitude by the equation,

$$\ln\left[AH\sinh\left(\frac{Kp\mu T}{H}\right)\right] = \frac{Kp\mu T_D}{H} + A_0, \tag{56}$$

where A is the oscillation amplitude, and A_0 is a constant value. From the Dingle plot (Fig. 74) , we obtain $T_{\rm D} \approx 2.3$ K, which shows that the sample quality is sufficiently high.

Figure 75(a) shows the angular dependence of the resistance for various field rotations. The definitions of the angles are indicated in Fig. 75(d). This oscillatory behavior is ascribed to AMRO. The AMRO peaks appear when the averaged electronic group velocity along the interlayer direction vanishes with the tilting the field. For a simply corrugated cylindrical Fermi surface, the peaks periodically appear as a function of $\tan(\theta)$.

The periodicity of the AMRO peak $\delta(\phi)$ [Fig. 75(b)] as a function of $\tan\theta$ is given by $\delta(\phi) = \pi/dk_{\parallel}(\phi)$, where d is the interlayer spacing and the projection of the wave vector $k_{\parallel}(\phi)$ is

$$k_{\parallel}(\phi)^2 = \left[k_{\rm F}^{\rm min}\cos(\phi-\zeta)\right]^2 + \left[k_{\rm F}^{\rm max}\sin(\phi-\zeta)\right]^2 \ , \tag{57}$$

where $k_{\rm F}^{\rm min}$ ($k_{\rm F}^{\rm max}$) is the minimum (maximum) of the Fermi wave vector and ζ is the inclination of the minor axis from [010].

A polar plot of the positions of the resistance peak shows the gourd-shaped characteristic (dotted curve) [Fig. 75(c)]. The solid curve shows the result fitted using Eq. (57) with $k_{\rm F}^{\rm min}$ = 0.03 Å^{-1}, $k_{\rm F}^{\rm max}$ = 0.225 Å^{-1}, ζ = 15°. Assuming an ellipsoidal cross section of the Fermi surface, we obtain $\pi k_{\rm F}^{\rm min} k_{\rm F}^{\rm max} \approx 0.021$ Å^{-2}, which corresponds to ∼5.6% of the first Brillouin

zone. These results are consistent with the previous studies.[91)]

Figure 76 shows the field dependence of out-of-plane resistance at various temperatures. At 5 K, the resistance increases steeply at a very low field and then gradually increases with increasing field. As the temperature decreases, we observe an anomalous waving behavior. At 0.7 K, the resistance increases above 2 K, has a step-like behavior between 4 T and 10 T, and then steeply increases again. Since H_{c2} is ∼14 T at 0.7 K, the non-zero value of the resistance in the wide field region up to H_{c2} is likely caused by the vortex dynamics as will be discussed later.

Figure 77 shows the second derivative curves of the resistance. The characteristic structures clearly show that with increasing fields at 0.55 K, there is a broad dip at ∼2 T (H_1), above which the finite resistance appears. At ∼8 T (H_2) and ∼9.5 T (H_3), the second and third dips are observed, where we see the step like structure in the $R(H)$ curve. In the range ∼9.5–12.5 T, an oscillating behavior is observed. Above ∼12.5 T (H_4), no structure is found and the second derivative curve becomes flat. All the characteristic fields (H_1–H_3) decrease with increasing temperature. The dip at H_3 and oscillating behavior are observed only below ∼2.6 K. Above 3.2 K, we can not define H_2 and H_3. For comparison, the $H_{c2}(H_{irr})$ values obtained by the magnetic torque measurements are plotted.

The structure of the resistance below H_{c2} is likely related to vortex dynamics. The non-zero resistance and the origins of the structure are discussed later. Judging from these results, we define the following four phases I–IV. Region I: $H < H_1$; Region II: $H = H_1$–H_2; Region III: $H = H_2$–H_3; and Region IV: $H > H_3$. The phase diagram obtained from these results is shown in Fig. 78.

Figure 79 shows the field dependence of the $-d^2R/dH^2$ curve at various field angles for $T = 1.5$ K. At 15.2°, the $-d^2R/dH^2$ curve has a minimum and maximum at 1 T and 1.8 T, respectively. This behavior shows that the $R(H)$ curve gradually increases with field. As the field is tilted to the parallel direction, the curve broadens and small structures appear. At 0°, we see an additional dip at 2.5 T. From these data, a phase diagram shown in Fig. 80 is developed.

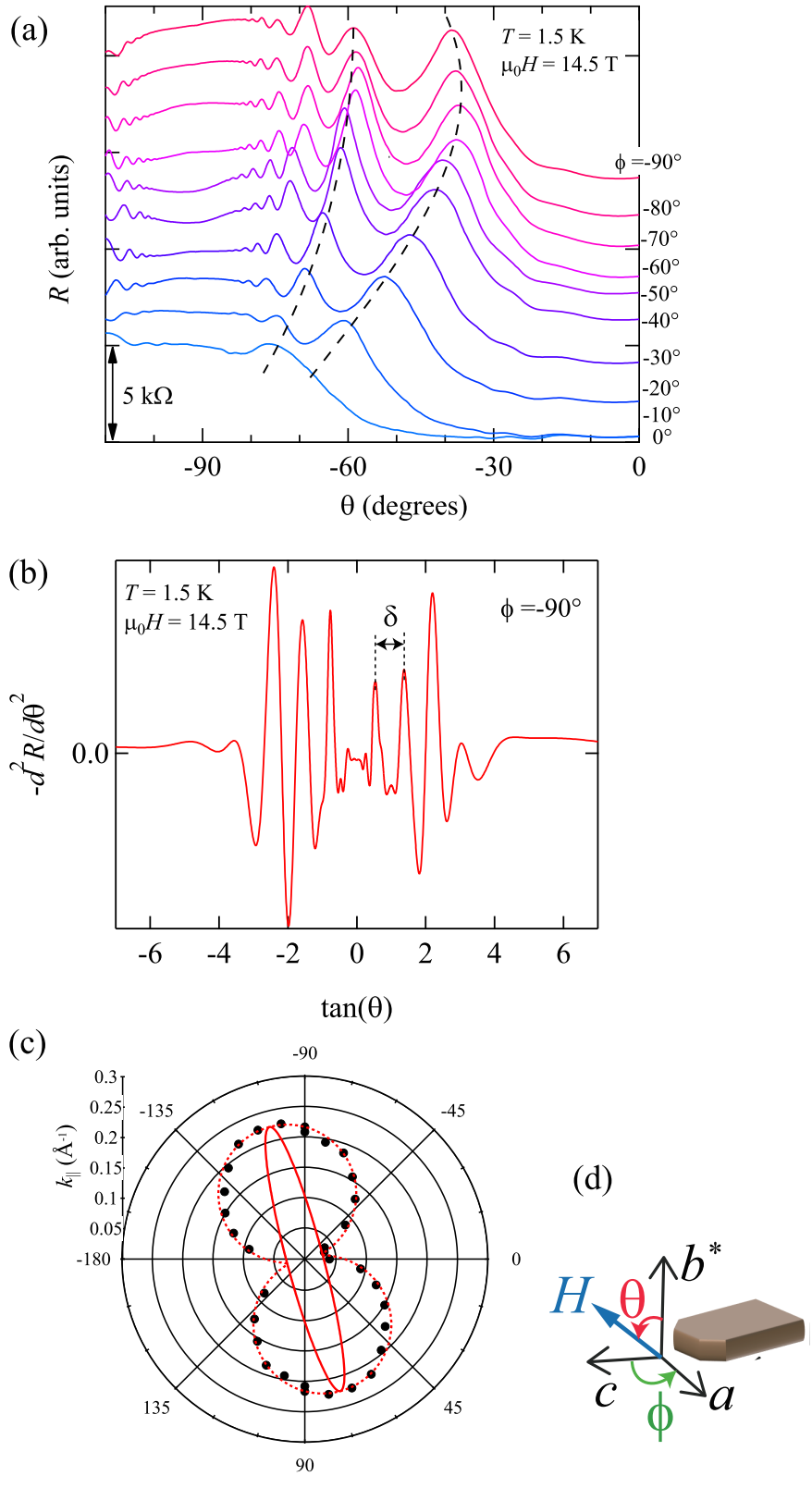

Figure 75: (a) Angular dependent magnetoresistance oscillations at 1.5 K and 14.5 T for various ϕ. (b) Definitions of the periodicity of the AMRO peak $\delta(\phi)$. (c) Polar plot of $k_{||}$ determined by $\delta(\phi)$. (d) Definitions of the angles.

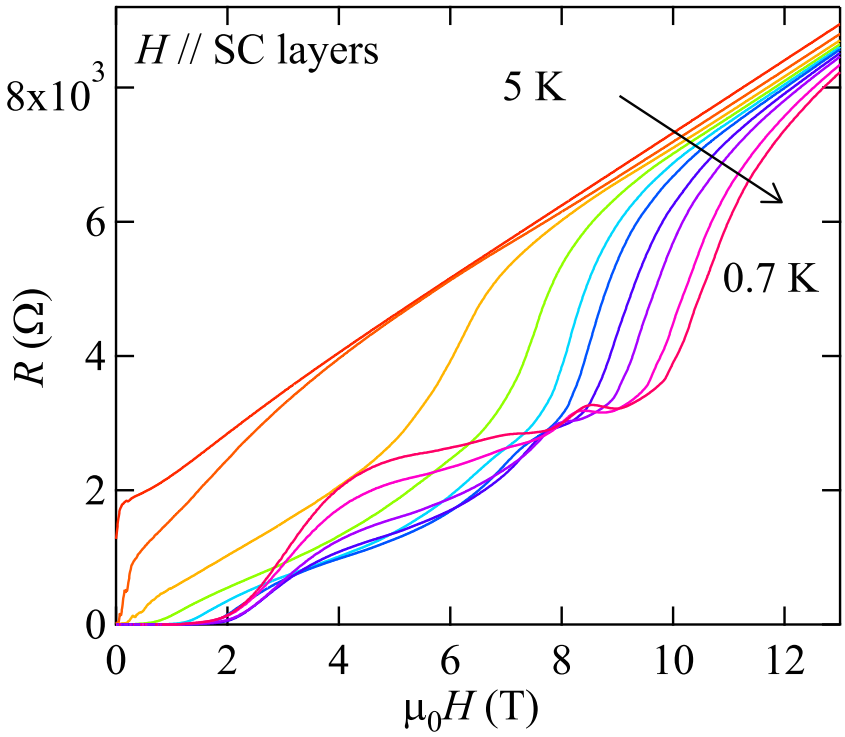

Figure 76: Magnetic field dependence of out-of-plane resistance at various temperature in β"-(BEDT-TTF)$_2$SF$_5$CH$_2$CF$_2$SO$_3$ for $\theta = 0°$ and $\phi = -90°$.

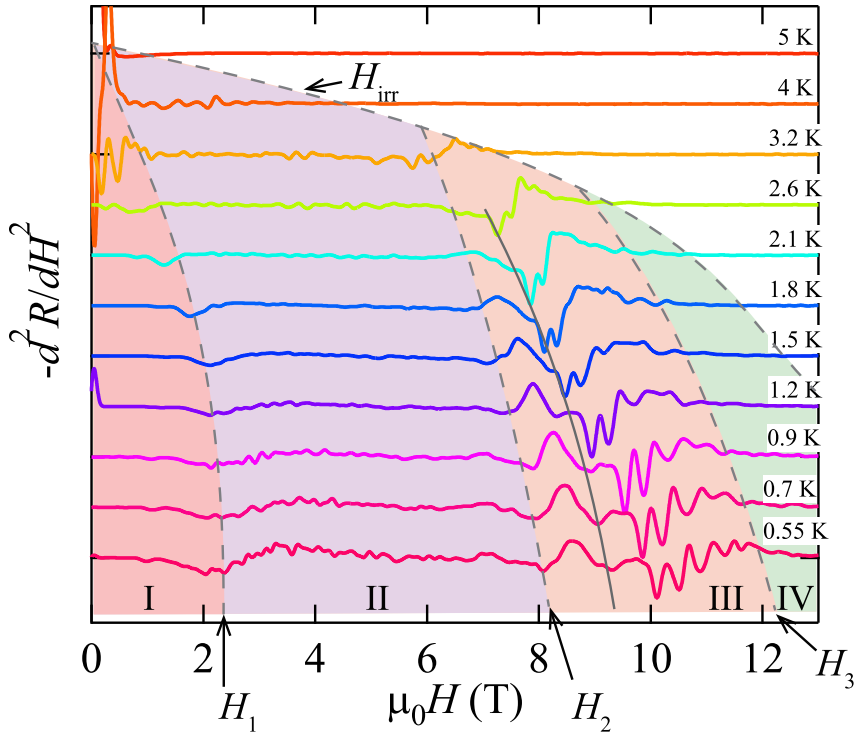

Figure 77: Second derivative curves of resistance at various temperature in β"-(BEDT-TTF)$_2$SF$_5$CH$_2$CF$_2$SO$_3$ for $\theta = 0°$ and $\phi = -90°$.

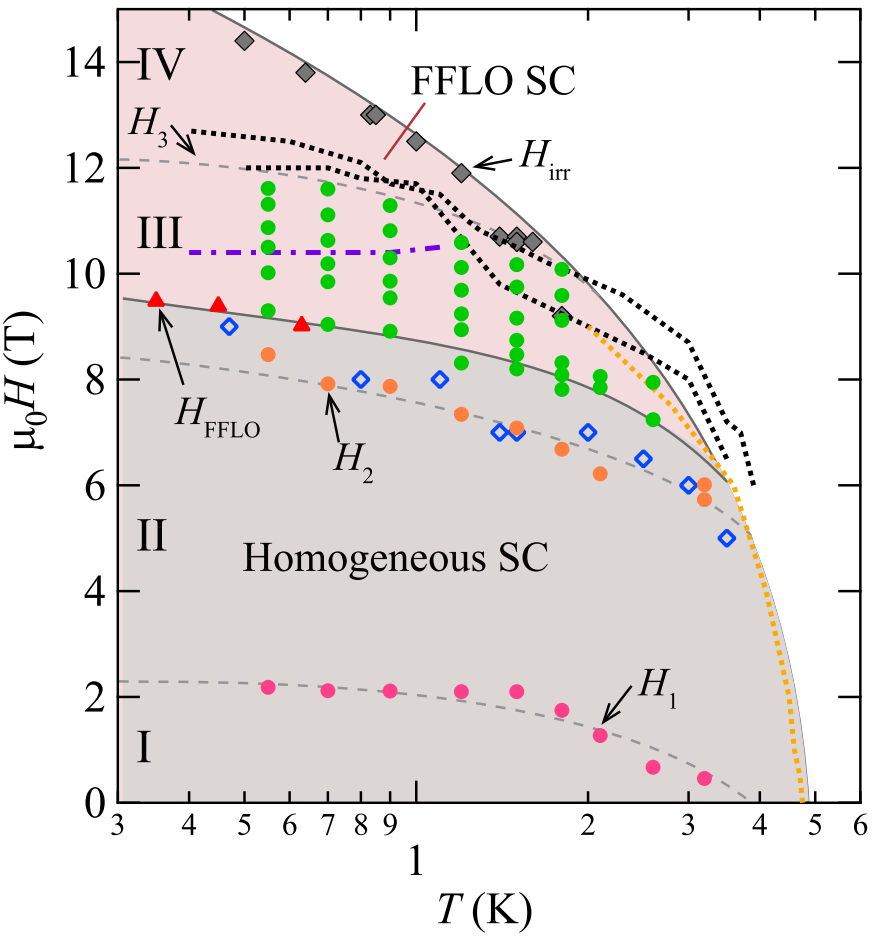

Figure 78: Temperature dependence of dips in $-d^2R/dH^2$ curves.

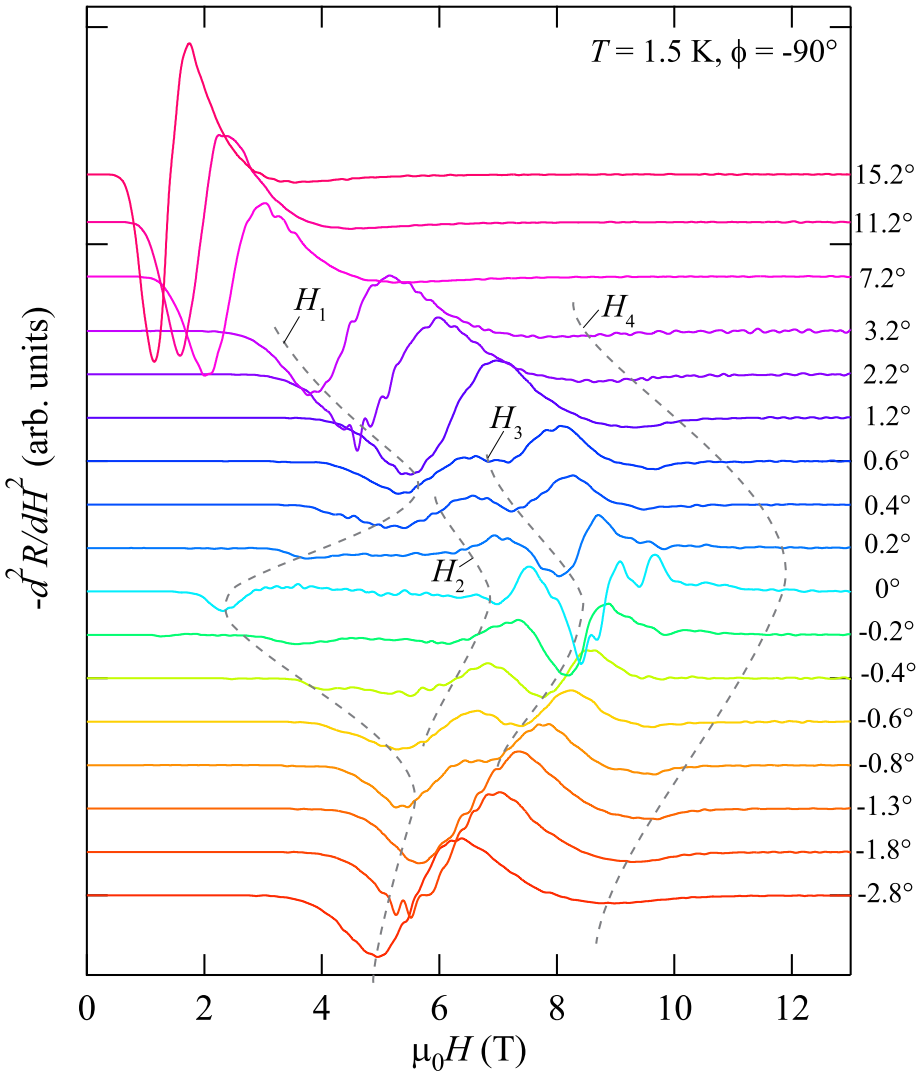

Figure 79: Second derivative curves of resistance at various angles θ at 1.5 K.

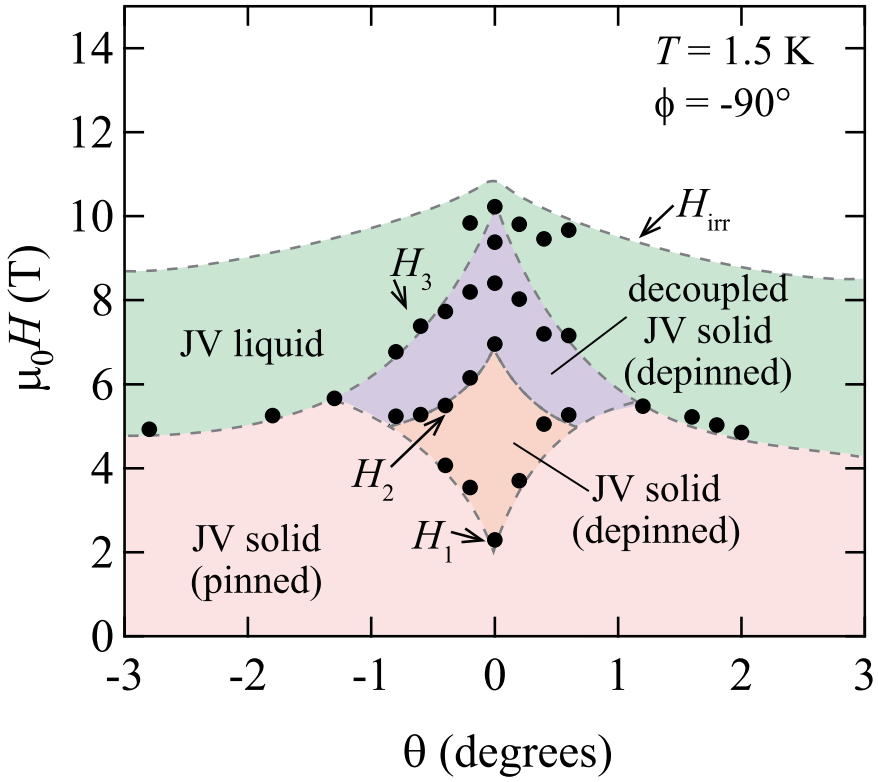

Figure 80: Angular dependence of the dips in $-d^2R/dH^2$ curves at 1.5 K.

Chapter 2

Discussion

2.1 Superconducting anisotropy

The β''-SF_5 salt is recognized as a highly 2D superconductor because of the large anion between the superconducting layers. Here, we discuss the anisotropy of the superconducting state. The superconducting anisotropy parameter γ can be expressed in terms of the ratio of the respective effective masses as $\gamma = \sqrt{m_c/m_a}$, where m_c and m_a are the Ginzburg-Landau (GL) superconducting effective masses for the pair motion along the interlayer direction and in the conducting plane, respectively. A few different methods have been used to estimate the parameter γ.

A) Estimation by the anisotropy of the critical field.

The value of γ is given by $\gamma = H_{c2}^{orb}/H_{c2}^{\perp} = \xi_{\parallel}/\xi_{\perp}$, where H_{c2}^{orb} and $H_{c2}^{\perp}$ are the parallel and the perpendicular critical fields, and $\xi_{\parallel}$ and $\xi_{\perp}$ are the in-plane and the out-of-plane coherence lengths, respectively. The H_{c2}^{orb} value can be estimated by the Werthamer–Helfand–Hohenberg formula, given as[104)]

$$H_{c2}^{orb} = 0.7 \left.\frac{dH_{c2}}{dT}\right|_{T=T_c} T_c. \tag{58}$$

We estimate $dH_{c2}/dT \approx 5.9$ from a fit of the $T_c(H)$ curve [Fig. 63(b)] at $T \approx T_c = 5.2$ K. I$\mu_0 H_{c2}^{orb} \approx 21.5$ T is obtained by using the above formula. Using $\mu_0 H_{c2}^{\perp} \approx 1.3$ T determined by the thermal-expansion measurements,[73)] $\gamma = 16.5$ is obtained. From the values of $\mu_0 H_{c2}^{orb}$ and $H_{c2}^{\perp}$, $\xi_{\parallel} \approx 16$ nm and $\xi_{\perp} \approx 0.96$ nm are estimated from the relations $H_{c2}^{\perp} = \Phi_0/2\pi\xi_{\parallel}^2$ and $H_{c2}^{orb} = \Phi_0/2\pi\xi_{\parallel}\xi_{\perp}$.

B) Estimation from the magnetic torque curve

The values of γ have been reported as $\gamma = 55$–200 for $Bi_2Sr_2CaCu_2Ox$ (Bi:2212), and $\gamma \approx 90$ for $Tl_2Ba_2CaCu_2O_x$.[106–108)] These values are obtained by fitting the experimental magnetic torque date with the anisotropic GL expression in the London limit derived by Kogan.[105)] For the 2D superconductors, the magnetic torque for $\gamma \gg 1$ and $H_{c1} \ll H \ll H_{c2}$ can be written as

$$\frac{\tau}{H\cos(\theta)} = \frac{\Phi_0}{16\pi\mu_0\lambda^2}\frac{\gamma H_z}{H\epsilon(\theta)}\ln\left(\frac{\gamma\eta H_{c2}}{H\epsilon(\theta)}\right), H\epsilon(\theta) = \sqrt{H_x^2+\gamma^2 H_z^2}. \quad (59)$$

Figure 81(a) shows the angular dependence of the magnetic torque curve (black curve) at $\mu_0 H = 8$ T and $T = 1.1$ K, and the calculated result (dashed red curve) by Eq. (59) for $\mu_0\eta H_{c2} = 1.5$ T and $\gamma = 50$. The magnetic torque curve corresponds to the perpendicular magnetization as discussed in section II–1.1. The sharp increase in the torque signal near 0° arises from the Meissner effect of the superconducting layers. The data at low angles only are well reproduced by the theory. At higher angles, the calculation is significantly larger than the experimental data. At 6.5 T [Fig. 81(b)], the discrepancy is more enhanced at high angles, probably because of the angular dependence of the γ value. The obtained γ values (45–50) are approximately three times as large as that obtained by method A.

In Bi:2212, the γ value decreases from 1500 to 280 with field increasing from 0.2 to 1.2 T. Such field dependence of γ is inconsistent with the anisotropy GL model in which γ is supposed to be independent of the field.[88] At present, the origin of the discrepancy between the two methods is not fully understood yet. It is likely that the γ value depends on both temperature and field since γ should be a function of the order parameter. If so, it is difficult to compare the γ values between the two methods because γ is defined at zero temperature in method A. Further investigation will be required for the detailed understanding.

In the β"-SF_5 salt, γ may also depend on the magnetic field similar to the case of Bi:2212. Therefore, the γ value could not be estimated from a fit of torque curve to Eq. (59) for the β"-SF_5 salt.

2.2 FFLO phase diagram

The observation of $H_{\rm peak1}$ in a very limited angle region [Fig. 63(a)] is consistent with the scenario of the FFLO transition; the FFLO phase is strongly destabilized by the orbital effect. The field dependence of the RF response (RF change of a tunnel diode oscillator) shows an anomaly at ∼10.5 T for $T = 0.45$ K.[74] The ^{13}C NMR measurement shows a kink at ∼9.3 T in the relaxation rate for $T = 0.13$ K.[75] These features are interpreted as the FFLO phase transition, approximately consistent with the MCE peak at $H_{\rm peak1}$. As the field increases, the perpendicular diamagnetism is expected to reduce at the FFLO phase because the flux lines can penetrate the sample along the nodes of the order parameter. (Fig. 82)

Therefore, the kink in the $-dM_z/dH_z$ curve (Fig. 58) also provide strong evidence of the FFLO transition.[81] The FFLO phase boundary is terminated at ∼8 T and ∼2 K, where a tricritical point exists.

The Clausius–Clapeyron relation at the FFLO phase transition is given by $\Delta S/\Delta M = -\partial H_{\rm FFLO}/\partial T$, where ΔS and ΔM are the jumps of the entropy and magnetization at the FFLO transition field $H_{\rm FFLO}$.S The entropy jump at $H_{\rm FFLO}$ should be very small $\Delta S \approx 0$ since $\partial H_{\rm FFLO}/\partial T \approx 0$ at low temperatures below ∼0.4 K. Consequently, the latent heat $T\Delta S$ should

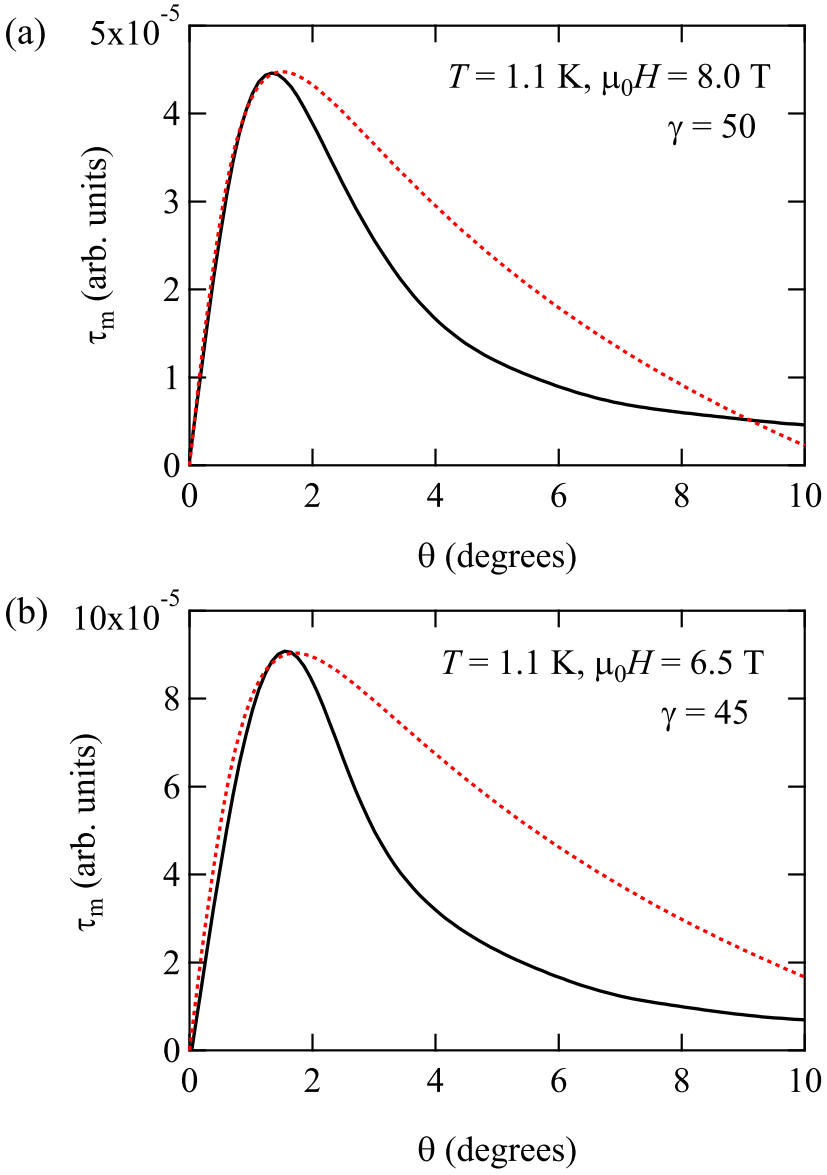

Figure 81: Angular dependence of the magnetic torque without the pinning effect of the vortices at constant fields of (a) 8 T and (b) 6.5 T. Dashed red curves are the results calculated by Eq. (59).

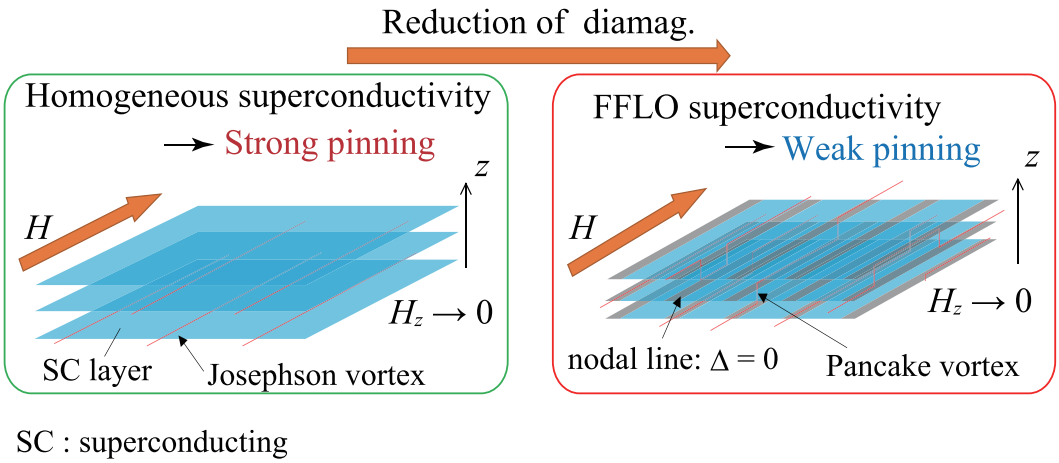

Figure 82: Schematic illustration of diamagnetic reduction.

also be small at $H_{\rm FFLO}$. The MCE peak at $H_{\rm FFLO}$ arises predominantly from the ΔT term in Eq. (41). Since the heat capacity jump is given by $\Delta C = T\partial\Delta S/\partial T$, it is very difficult to observe the FFLO transition in the heat capacity measurements. Above ∼0.5 K, we see $\partial H_{\rm FFLO}/\partial T < 0$ (Fig. 63) and $\Delta M > 0$ (Fig. 58) at $H_{\rm FFLO}$ as the field increases. Therefore, we conclude $\Delta S > 0$; the entropy in the FFLO phase is larger than that in the homogeneous superconducting phase. However, no sign reversal of the MCE signal at $H_{\rm FFLO}$ in the entire temperature range shows that ΔS is too small to detect.

2.3 Vortex phase transitions

In layered superconductors, the following two types of vortices are formed in tilted fields: PVs penetrating superconducting layers and JVs in insulating layers between the superconducting layers. At low temperatures and fields, where thermal fluctuation is suppressed, the PVs and JVs likely occur in a solid phase. As the field increases, the lattice constant $a_{\rm PV} = \sqrt{\Phi_0/H}$ for the PV and $a_{\rm JV} = \Phi_0/sH$ for the JV decreases, where Φ_0 and s are the flux quantum and layer spacing, respectively. When the mean-square amplitude of the vortex fluctuations in a solid phase becomes comparable to the lattice constant, the vortices melt.[95] This melting transition will take place even at zero temperature because of the quantum fluctuations. In the parallel field, as the field increases, the Josephson coupling between the layers is suppressed and the flux lines are highly entangled. Therefore, it is likely that the JVs melt first followed by the PVs; $H_{\rm peak2}$ and $H_{\rm peak3}$ in the MCE (Fig. 67) are assigned to the melting transitions of the PVs and JVs, respectively. The JVs are confined in the insulating layers, showing a melting of the 1D array, in contrast to the 2D melting for the PVs. In general, the fluctuation effect is more enhanced in a lower dimension system. It is probably the reason for the much broader melting transition of the JVs than that of the PVs.

The H_{c2} value rapidly increases as $\theta \to 0°$, showing that both the Josephson coupling and

order parameter are enhanced. Therefore, it will be reasonable that the melting transition fields of the PVs and JVs increase as $\theta \to 0°$. For $\theta \approx 0°$, we note that $H_{\rm peak3}$ exceeds $H_{\rm peak1}$; the JVs melt in the FFLO phase. The number of the PVs ($n_{\rm PV}$) decreases as $\theta \to 0°$, proportional to $H \sin(\theta)$. The vanishing of $H_{\rm peak2}$ for $|\theta| < 4°$ in Fig. 62 and Fig. 63(a) suggests that $n_{\rm PV}$ is lower than the dilution limit of the solidification.[96)]

The above results resolve the inconsistencies of the previous experiments. The temperature dependence of the heat capacity at high fields shows a peak below $H_{\rm c2}$ when the field is slightly tilted from the parallel direction.[76)] As the field is tilted, the peak field decreases. From the comparison with our data, the heat capacity peak is the JV melting transition. In the NMR measurements, the ^{13}C relaxation rate in parallel fields has a small jump at 11 T above the FFLO transition for $T = 0.13$ K whereas the Knight shift shows a smooth variation around 11 T.[75)] The jump of the relaxation rate is also likely due to the JV melting.

In the perpendicular field, the flux lines penetrate the superconducting layers perpendicularly, where only PVs are formed in the superconducting layers. Since the PVs in the liquid phase fluctuate greatly and are not pinned in the superconducting layers, the flux jump is expected to observed only in the vortex solid phase. Therefore, the cessation field of the flux jumps in the MCE can be defined as the melting transition field $H_{\rm melt}$ (Fig. 69).

Figure 83 shows the temperature dependence of the PV melting transition field of the β''-SF_5 salt; the vertical and horizontal axes are normalized by $H_{\rm c2}$ and $T_{\rm c}$, respectively. For comparison, the results of a typical organic layered superconductor κ-(BEDT-TTF)$_2$Cu(NCS)$_2$ (κ-Cu(NCS) salt)[93)] are also presented. The melting transition fields $H_{\rm melt}$ of both salts are obtained from the MCE measurements in the perpendicular field. We note that both $H_{\rm melt}(T)$ curves lie on a single curve with an upward curvature.

As shown in section I–1.4, there are two mechanisms causing the melting transition: thermal and quantum fluctuations. The thermal melting line of a 2D solid is given as[109)]

$$T_m^{th}/T_{\rm c} \approx \left(c_L^2/G_i\right)\left(1 - H/H_{\rm c2}\right)^2 \ , \tag{60}$$

where c_L and G_i are the Lindemann criterion and the Ginzburg number, respectively. The dashed line in Fig. 83 is the thermal melting line calculated by Eq. (60) with $c_L = 0.09$ and $G_i = 0.01$. The melting transition field is reasonably reproduced by the theoretical model. For the κ-Cu(NCS) salt, the $H_{\rm melt}(T)$ curve seems to show a saturation behavior at low temperatures. This is probably because of the quantum melting transition.

In the 2D limit relevant for thin superconducting films with $d < \xi$, the quantum melting transition field H_m^Q is given as[110)]

$$H_m^Q/H_{c2} = 1 - 1.2\exp\left[-\frac{\pi^3 c_L^2}{4}\frac{R_Q}{R_N}\right], \tag{61}$$

where R_Q and R_N are the quantum resistance ($\sim$4.1 kΩ) and the sheet resistance ($=\rho_N/d$), respectively. The H_m^Q value, which exponentially depends on R_N, has a large ambiguity because it is difficult to obtain R_N precisely. Assuming $R_N \approx 200$ Ω, we obtain $H_m^Q/H_{\rm c2} \approx 0.67$ from

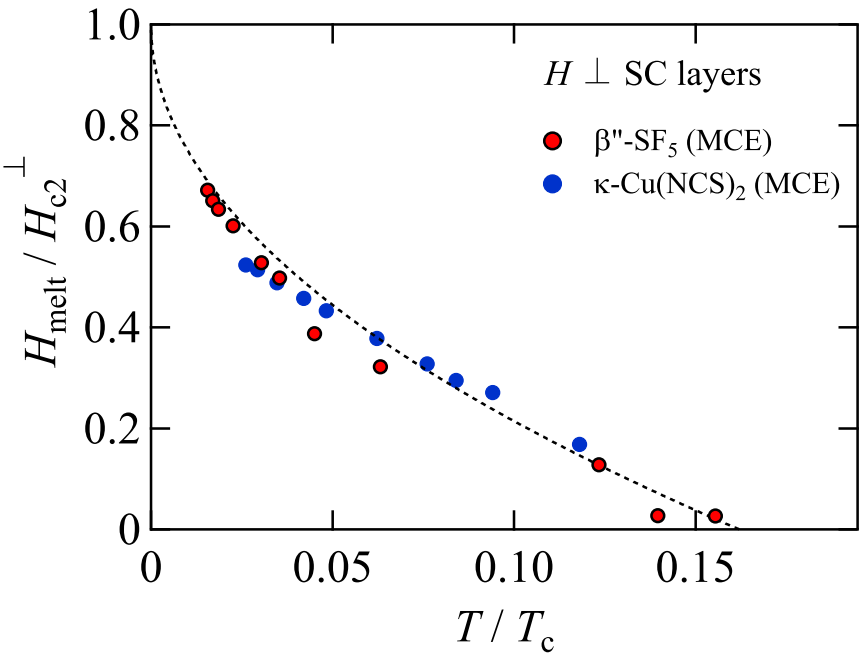

Figure 83: Normalized melting transition fields of PVs as a function of normalized temperature for two layered organic superconductors. The dashed red curve is the result calculated by the thermal melting model given in Eq. (60).

Eq. (61), which is close to the $H_{\rm melt}$ value of the κ-Cu(NCS) salt ($\sim$0.63).[26)]

For the β"-SF$_5$ salt, no saturation behavior in the $H_{\rm melt}(T)$ curve is observed, thus suggesting that the quantum melting transition is relatively higher than that of the κ-Cu(NCS) salt. A possible reason is that R_N is lower for the β"-SF$_5$.

2.4 Commensurability effect

Figure 84 shows a schematic illustration of the JV lattice and the order parameter oscillation. In parallel fields, all the flux lines penetrate in the insulating layers [Fig. 84(a)] When the FFLO state is realized in the layered superconductor, a novel commensurability effect is expected; the JV lattice can be strongly pinned by the periodic structure of the order parameter $\Delta_n \propto \Delta_0 \cos(qr + \alpha_0)$ when the JV lattice constant l is commensurate with the wavelength of the order parameter oscillation $\lambda_{\rm FFLO}$. [Fig. 84(b)] Here, Δ_n and α_0 are the order parameter and the phase of the FFLO modulation in the nth layer, respectively. In the FFLO phase, the Josephson coupling strength between the layers is expected to periodically change with position because of the order parameter oscillation.

The dips of $-d^2R/dH^2$ curves in the FFLO phase, which show a relatively strong pinning of the JVs, can be ascribed to the commensurability effect between the wavelength of the FFLO

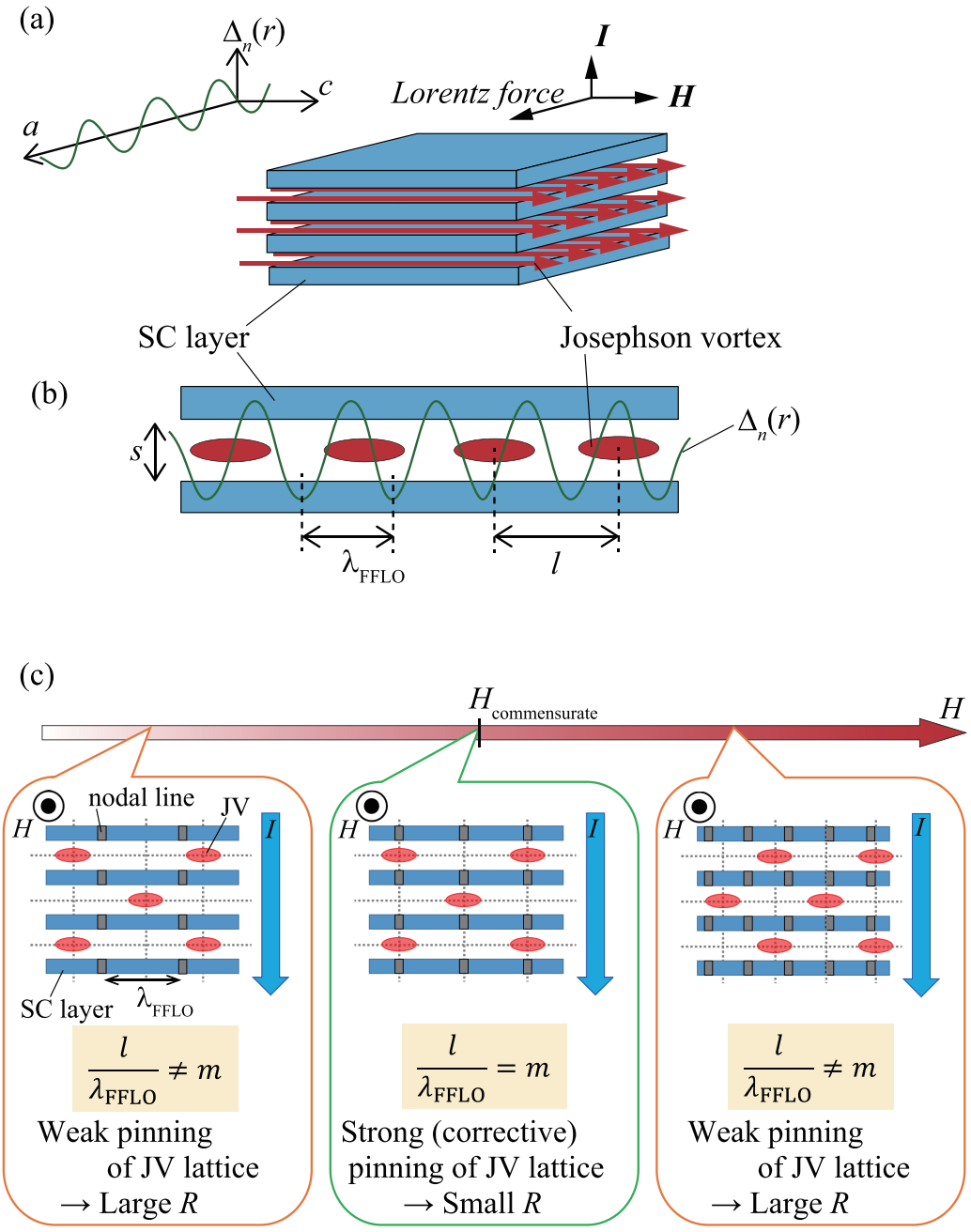

Figure 84: Schematic illustration of the commensurability effect.

order parameter oscillation $\lambda_{\rm FFLO}$ and the JV lattice constant l. The lattice constant is given by $l = \Phi_0/sH$, where s is the layer spacing ($s \approx$1 nm) and Φ_0 is the flux quantum. In the homogeneous superconducting phase, $\lambda_{\rm FFLO}$ should be finite. However, with the increasing magnetic field, $\lambda_{\rm FFLO}$ is expected to jump to a finite value at the FFLO phase transition. After that, $\lambda_{\rm FFLO}$ will decrease with the field increasing up to H_{c2}.

Here, $\lambda_{\rm FFLO}$is estimated on the basis of the following assumptions:
(i) $l/\lambda_{\rm FFLO}$ is given by simple integers N; $l/\lambda_{\rm FFLO} = N$.
(ii) $\lambda_{\rm FFLO}$ is an order of $\xi_{\|}$ ($\approx$ 23 nm) near H_{c2}.
(iii) N is close to unity at $H_{\rm FFLO}$.
The estimated value is shown in Fig. 85(a) as black circles. For simplicity, the q vector is assumed to be perpendicular to the field.

In Fig. 85(a), we note that $\lambda_{\rm FFLO}$ rapidly increases with decreasing field. Similar upward behavior has been obtained for other organic superconductors.[24] Tachiki *etal*. theoretically discussed the superconducting order parameters of a FFLO phase and obtained $\lambda_{\rm FFLO}$ as a function of the magnetic field, which included the orbital effect.[111] They show that the $\lambda_{\rm FFLO}(H)$ curve has an upward curvature with decreasing field, and it ranges from $30\xi_{\|}$ to $13\xi_{\|}$ when the orbital effect is strongly suppressed. In Fig. 85(b), we obtain $\lambda_{\rm FFLO}/\xi_{\|} = 1.3$–$9.5$ for the six dips. Because the stability of the FFLO phase is related to the nesting instability of the Fermi surface, it is theoretically difficult to obtain the optimum q vector for the anisotropic Fermi surface such as the β"-SF_5 salt [Fig. 75(b)].

The abovementioned estimation is made for the case of $q \perp H$, which may not be accurate. For example, when the q vector is tilted by 40° from the field direction, $\lambda_{\rm FFLO}$ becomes smaller by a factor cos(theta), as shown by the green circles in Fig. 85(a). As long as the q vector is not exactly parallel to the field, the abovementioned commensurability model is qualitatively valid and we obtain an upward curvature of $\lambda_{\rm FFLO}(H)$ as theoretically predicted.[111]

2.5 Coupling–decoupling effect of Josephson vortices

Finally the origin of the kinks of the resistance curves for $H \parallel$ superconducting layers in the superconducting phase will be discussed. Non-zero resistance in a wide field region up to H_{c2} for $\theta = 0°$ show that JVs are easily driven by the perpendicular current.

At low temperatures and fields, the superconducting layers are strongly Josephson-coupled (Fig. 86: Region I) , suggesting that the JV layers are coupled between adjacent layers. (Figs. 77, 86: Regions I and II) As the field increases, the interlayer coupling of the JVs weakens and the JV layers will be decoupled. After decoupling, each JV layer can be driven independently (Fig. 86: Region III). This decoupling, which effectively reduces the pinning force, will lead to an increase in the interlayer resistance. This is a possible mechanism of the appearance of kinks in the out-of-plane resistance. As the temperature increases, the kink fields decrease. The result is consistent with the mechanism explained above, and the Josephson coupling is reduced with increasing temperature.

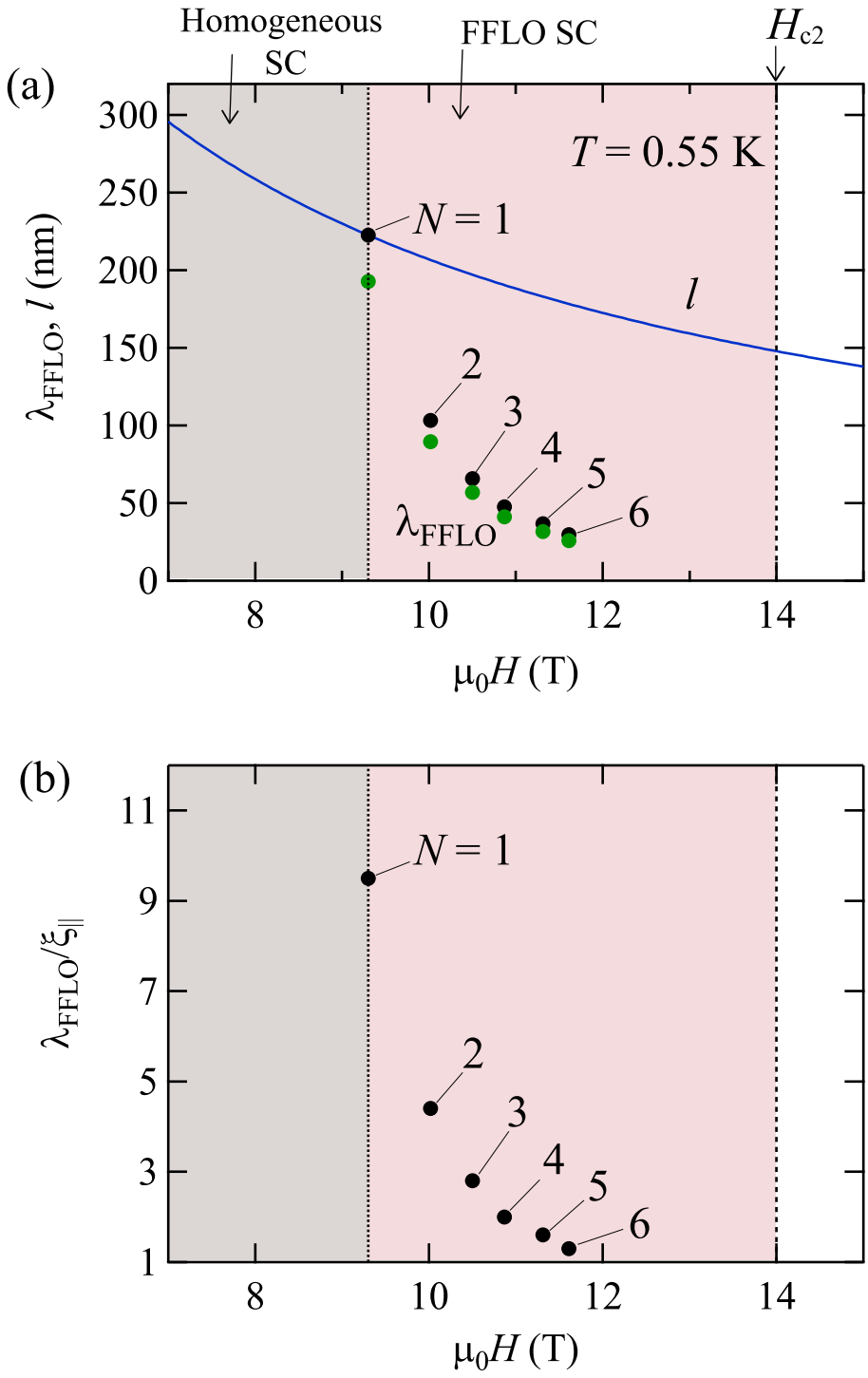

Figure 85: (a) Estimated λ_{FFLO} values and calculated l as a function of the magnetic field. The green circles show the results when the q vector is tilted by 50° from the field. (b) Estimated λ_{FFLO} values by using the following assumptions: $q \perp H$, $s = 1$ nm, $\lambda_{\mathrm{FFLO}} \approx \lambda_{\mathrm{FFLO}}$ at H_{c2}, and N is given by simple integers. The integer N is indicated.

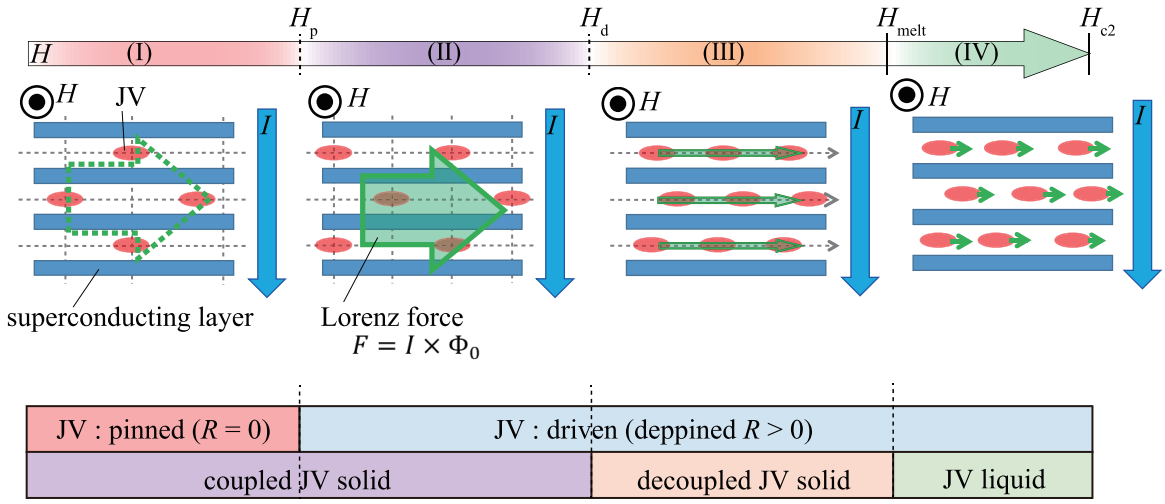

Figure 86: Schematic illustration of Josephson vortices phase transition.

Chapter 3

Conclusion

To observe the FFLO phase transition distinct from vortex melting transitions, the magnetic torque, the magnetocaloric effect, and the resistance in the β"-SF_5 salt were measured.

In magnetic torque measurements, each torque curve exhibits hysteresis between the up and down sweeps of the magnetic field, where the irreversibility fields ($H_{\rm irr}$) can be defined The diamagnetic signals at all temperatures decrease with increasing field, which are associated with kinks. The critical field $H_{\rm c2}$, which should be slightly larger than $H_{\rm irr}$, can not be determined without ambiguity because of the smooth variation above $H_{\rm irr}$. The $H_{\rm irr}$ value decreases with increasing temperature.

In nearly perpendicular fields, we clearly see de Haas–van Alphen oscillations [Fig. 56(b)]. The result shows that the superconductivity is within the clean limit, which is required for the FFLO phase. The frequency of the oscillation ($F \approx 200$ T) is consistent with previous results.

The perpendicular diamagnetic susceptibility $-dM_z/dH_z$ as a function of field at various temperatures, is obtained from the angular dependence of the torque. The diamagnetic signals at all temperatures decrease with increasing field, which are associated with kinks. The kink field $H_{\rm kink}$ is lower than $H_{\rm irr}$ for $T \leq 1.1$ K, which corresponds to the FFLO transition.

In the ΔT curves, three series of peaks are observed. Only in a limited angle region ($|\theta| \lesssim 1.5°$), a broad peak (denoted by $H_{\rm peak1}$) is observed at ~ 9.5 T, which is associated with a small hysteresis between the up and down sweeps. The peak at $H_{\rm peak1}$ is ascribed to the FFLO transition. Since the periodic nodal line structure is formed in the FFLO phase, the vortices are expected to be reconfigured in the sample, which also causes heating for both sweeps. The observation of $H_{\rm peak1}$ in a very limited angle region is consistent with the scenario of the FFLO transition; the FFLO phase is strongly destabilized by the orbital effect.

When the field is tilted from the superconducting layers, two additional series of peaks associated with a hysteresis are observed: sharp and broad peaks, denoted by $H_{\rm peak2}$ and $H_{\rm peak3}$, respectively. $H_{\rm peak2}$ and $H_{\rm peak3}$ show rapid increases as $\theta \to 0°$.

In perpendicular fields, the QOs are clearly observed. Sign inversion of the ΔT curves are observed between the up and down sweeps, which is caused by the second term. The field angle dependence of the quantum oscillation frequency is well fitted by $1/\cos\theta$. The $1/\cos\theta$

dependence clearly shows the presence of the 2D Fermi surface.

At 5 K, the resistance has a steep increase at a very low field, which then gradually increases with increasing field. As the temperature decreases, anomalous waving behavior is observed. At 0.7 K, the resistance increases above 2 K, has a step-like behavior between 4 T and 10 T, and then steeply increases again. Since H_{c2} is ∼14 T at 0.7 K, the non-zero value of the resistance in the wide field region up to H_{c2} is likely caused by the vortex dynamics.

In the resistance, characteristic structures are clearly observed. With increasing fields at 0.55 K, a broad dip is observed at ∼2 T (H_1), above which the finite resistance can be observed. At ∼8 T (H_2) and ∼9.5 T (H_3), the second and third dips are observed, where the $R(H)$ curve exhibits a step-like structure. In the range ∼9.5–12.5 T, oscillating behavior is observed. Above ∼12.5 T (H_4), no structure is found and the second derivative curve becomes flat. All the characteristic fields (H_1–H_3) decrease with increasing temperature. The dip at H_3 and the oscillating behavior are observed only below ∼2.6 K. Above 3.2 K, H_2 and H_3 can not be defined. The structure of the resistance below H_{c2} is likely related to vortex dynamics.

References

[1] H. Kobayashi, H. Cui, and A. Kobayashi, Chem. Rev. **104**, 5265 (2004).

[2] H. Taniguchi, M. Miyashita, K. Uchiyama, K. Satoh, N. Mori, and H. Okamoto, J. Phys. Soc. Jpn. **72**, 468 (2003).

[3] T. Mori, Bull. Chem. Soc. Jpn. **71**, 2509 (1998).

[4] M. Kurmoo, A. W. Graham, P. Day, S. J. Coles, M. B. Hursthouse, J. L. Caulfield, J. Pratt, F. L. Singleton, W. Hayes, L. Ducasse, and P. Guionneau, J. Am. Chem. Soc., 117, 12209 (1995).

[5] E. Coronado, J. R. Galan-Mascaros, C. J.Gomez-Garcia, and V. Laukhin, Nature **408**, 447 (2000).

[6] T. Mori and M. Katsuhara, J. Phys. Soc. Jpn. **71**, 826 (2002).

[7] H. Kobayashi, H. Tomita, T. Naito, A. Kobayashi, F. Sakai, T. Watanabe, and P. Cassoux, J. Am. Chem. Soc. **118**, 368 (1996).

[8] H. Kobayashi, H. Tanaka, E. Ojima, H. Fujiwara, Y. Nakazawa, T. Otsuka, A. Kobayashi, M. Tokumoto, and P. Cassoux, Synth. Met. **120**, 663 (2001).

[9] K. Sugii, K. Takai, S. Uji, T. Terashima, H. Akutsu, A. Wada, S. Ichikawa, J. Yamada, T. Mori, and T. Enoki, J. Phys. Soc. Jpn. **82**, 054706 (2013).

[10] H. Fujiwara, K. Wada, T. Hiraoka, T. Hayashi, T. Sugimoto, H. Nakazumi, K. Yokogawa, M. Teramura, S. Yasuzuka, K. Murata, and T. Mori, J. Am. Chem. Soc. **127**, 14166 (2005).

[11] H. Fujiwara, T. Hayashi, T. Sugimoto, H. Nakazumi, S. Noguchi, L. Li, K. Yokogawa, S. Yasuzuka, K. Murata, and T. Mori, Inorg. Chem. **45**, 5712 (2006).

[12] X. Xiaoa, J. Fanga, J. Zhoua, H. Gaoa, H. Fujiwarab, and T. Sugimoto, Synth. Met. **160**, 2413 (2010).

[13] P. Fulde, and R. A. Ferrell, Phys. Rev. **135**, A550-563 (1964).

[14] A. I. Larkin, and Y. N. Ovchinnikov, Zh. Eksp. Teor. Fiz. **47**, 1136 (1964).[translation Sov. Phys. JETP 20, 762 (1965).]

[15] H. Matsui, H. Tsuchiya, T. Suzuki, E. Negishi, and N. Toyota, Phys. Rev. B **68**, 155105 (2003).

[16] S. Endo, T. Goto, T. Fukase, H. Matsui, H. Uozaki, H. Tsuchiya, E. Negishi, Y. Ishizaki, Y. Abe, and N. Toyota, J. Phys. Soc. Jpn. **71**, 732 (2002).

[17] K. Hiraki, H. Mayaffre, M. Horvatic, C. Berthier, S. Uji, T. Yamaguchi, H. Tanaka, A. Kobayashi, H. Kobayashi, and T. Takahashi, J. Phys. Soc. Jpn. **76**, 124708 (2007).

[18] S. Uji, H. Shinagawa, C. Terakura, T. Terashima, T. Yakabe, and Y. Terai, M. Tokumoto, A. Kobayashi, H. Tanaka and H. Kobayashi, Phys. Rev. B **64** 024531 (2001).

[19] C. Hotta and H. Fukuyama, J. Phys. Soc. Jpn. **69**, 2577 (2000).

[20] M. Tokumoto, T. Naito, H. Kobayashi, A. Kobayashi, V. N. Laukhin, L. Brossard, and P. Cassoux, Synth. Met. **86**, 2161 (1997).

[21] L. Brossard, R. Clerac, C. Coulon, M. Tokumoto, T. Ziman, D. K. Petrov, V. N. Laukhin, M. J. Naughton, A. Andouard, F. Goze, A. Kobayashi, H. Kobayashi, and P. Cassoux, Eur. Phys. J. B **1**, 439 (1998).

[22] S. Uji and J. S. Brooks, J. Phys. Soc. Jpn. **75**, 051014 (2006).

[23] S. Uji, H. Shinagawa, T. Terashima, T. Yakabe, Y. Terai, M. Tokumoto, A. Kobayashi, H. Tanaka, and H. Kobayashi, Nature **410**, 908 (2001).

[24] S. Uji, T. Terashima, M. Nishimura, Y. Takahide, T. Konoike, K. Enomoto, H. Cui, H. Kobayashi, A. Kobayashi, H. Tanaka, M. Tokumoto, E. S. Choi, T. Tokumoto, D. Graf, and J. S. Brooks, Phys. Rev. Lett. **97**, 157001 (2006).

[25] S. Uji, K. Kodama, K. Sugii, T. Terashima, Y. Takahide, N. Kurita, S. Tsuchiya, M. Kimata, A. Kobayasahi, B. Zhou, and H. Kobayashi, Phys. Rev. B **85**, 174530 (2012).

[26] S. Uji, Y. Fujii, S. Sugiura, T. Terashima, T. Isono, and J. Yamada, Phys. Rev. B **97**, 024505 (2018)

[27] M.M. Mola, S. Hill, J. S. Brooks and J. S. Qualls, Phys. Rev. Lett. **86**, 2130 (2001)

[28] S. Uji, K. Kodama, T. Terashima, T. Yamaguchi, N. Kurita, S. Tsuchiya, M. Kimata, T. Konoike, A. Kobayashi, B. Zhou, and H. Kobayashi, J. Phys. Soc. Jpn. **82**, 034715 (2013).

[29] I. Rutel, S. Okubo, J. S. Brooks, E. Jobiliong, H. Kobayashi, A. Kobayashi, and H. Tanaka, Phys. Rev. B **68**, 144435 (2003).

[30] S. Komiyama, M. Watanabe, Y. Noda, E. Negishi, and N. Toyota, J. Phys. Soc. Jpn. **73**, 2385 (2004).

[31] E. Negishi, T. Kuwabara, S. Komiyama, M. Watanabe, Y. Noda, T. Mori, H. Matsui, and N. Toyota, Phys. Rev. B **71**, 012416 (2005).

[32] H. Akiba, S. Nakano, Y. Nishio, K. Kajita, B. Zhou, A. Kobayashi, and H. Kobayashi, J. Phys. Soc. Jpn. **78**, 033601 (2009).

[33] Y. Takahide, T. Konoike, K. Enomoto, M. Nishimura, T. Terashima, S. Uji, and H. M. Yamamoto, Phys. Rev. Lett. **96**, 136602 (2006).

[34] Y. Takahide, T. Konoike, K. Enomoto, M. Nishimura, T. Terashima, S. Uji, and H. M. Yamamoto, Phys. Rev. Lett. **98**, 16602 (2007).

[35] Y. Takahide, M. Kimata, K. Kodama, T. Terashima, S. Uji, M. Kobayashi, and H. M. Yamamoto, Phys. Rev. B **84**, 035129 (2011).

[36] K. Kodama, M. Kimata, Y. Takahide, N. Kurita, A. Harada, H. Satsukawa, T. Terashima, S. Uji, K. Yamamoto, and K. Yakushi, J. Phys. Soc. Jpn. **81**, 044703 (2012).

[37] S. Uji, K. Kodama, K. Sugii, Y. Takahide, T. Terashima, N. Kurita, S. Tsuchiya, M. Kohno, M. Kimata, K. Yamamoto, and K. Yakushi, Phys. Rev. Lett. **110**, 196602 (2013).

[38] T. Sasaki, H. Uozaki, S. Endo, and N. Toyota, Synth. Met. **120**, 759 (2001).

[39] M. Tokumoto, H. Tanaka, T. Otsuka, H. Kobayashi, and A. Kobayashi, Polyhedron **24**, 2793 (2005).

[40] N. Toyota, Y. Abe, H. Matsui, E. Negishi, Y. Ishizaki, H. Tsuchiya, H. Uozaki, and S. Endo, Phys. Rev. B **66**, 033201 (2002).

[41] P. Lunkenheimer, V. Bobnar, A. V. Pronin, A. I. Ritus, A. A. Volkov, and A. Loidl, Phys. Rev. B **66**, 052105 (2002).

[42] Y. Abe, H. Uozaki, H. Tsuchiya, E. Negishi, Y. Ishizaki, H. Matsui, S. Endo, and N. Toyota, Synth. Met. **133-134**, 563 (2003).

[43] R. R. Guseinov, Phys. Status Solidi B **125**, 237 (1984).

[44] T. Fujimoto, S. Yasuzuka, K. Yokogawa, H. Yoshino, T. Hayashi, H. Fujiwara, T. Sugimoto, and K. Murata, J. Phys. Soc. Jpn. **77**, 014704 (2008).

[45] T. Hayashi, X. Xiao, H. Fujiwara, T. Sugimoto, H. Nakazumi, S. Noguchi, T. Fujimoto, S. Yasuzuka, H. Yoshino, K. Murata, T. Mori, and H. A. Katori, J. Am. Chem. Soc. **128**, 11746 (2006).

[46] M. Maesato, T. Kawashima, G. Saito, T. Shirahata, M. Kibune, and T. Imakubo, Phys. Rev. B **87**, 085117 (2013).

[47] N. Toyota, Y. Abe, H. Matsui, E. Negishi, Y. Ishizaki, H. Tsuchiya, H. Uozaki, and S. Endo, Phys. Rev. B **66**, 033201 (2002).

[48] S. Sugiura, K. Shimada, N. Tajima, Y. Nishio, T. Terashima, T. Isono, A. Kobayashi, B. Zhou, R. Kato, and S. Uji, J. Phys. Soc. Jpn. **85**, 064703 (2016).

[49] K. Ito and H. Shimahara, J. Phys. Soc. Jpn. **85**, 024704 (2016).

[50] J. C. Waerenborgh, S. Rabaca, M. Almeida, E. B. Lopes, A. Kobayashi, B. Zhou, and J. S. Brooks, Phys. Rev. B **81**, 060413(R) (2010).

[51] H. Shimahara and K. Ito, J. Phys. Soc. Jpn. **85**, 043708 (2016).

[52] C. Rossel, P. Bauer, D. Zech, J. Hofer, M. Willemin, and H. Keller, J. Appl. Phys. **79**, 8166 (1996).

[53] M. Tokumoto, H. Tanaka, T. Otsuka, H. Kobayashi, and A. Kobayashi, Polyhedron **24**, 2793 (2005).

[54] T. Isono, H. Kamo, A. Ueda, K. Takahashi, M. Kimata, H. Tajima, S. Tsuchiya, T. Terashima, S. Uji, and H. Mori, Phys. Rev. Lett. **112**, 177201 (2014).

[55] T. Sasaki, H. Uozaki, S. Endo, and N. Toyota, Synth. Met. **120**, 759 (2001).

[56] K. Sugii, K. Takai, S. Tsuchiya, S. Uji, T. Terashima, H. Akutsu, A. Wada, S. Ichikawa, J. Yamada, and T. Enoki, J. Phys. Soc. Jpn. **83**, 023704 (2014).

[57] T. Konoike, S. Uji, N. Nishimura, K. Enomoto, H. Fujiwara, B. Zhang, and H. Kobayashi, Physica B 359-361, 457 (2005).

[58] K. Kodama, Dr. Thesis, Graduate School of Pure and Applied Science, University of Tsukuba, Ibaraki (2012)[in Japanese].

[59] S. Uji, K. Kodama, K. Sugii, T. Terashima, T. Yamaguchi, N. Kurita, S. Tsuchiya, T, Konoike, M. Kimata, A. Kobayashi, B. Zhou, and H. Kobayshi, J. Phys. Soc. Jpn. **84**, 104709 (2015).

[60] J. I. Oh, M. J. Naughoton, T. Courcet, I. Malfant, P. Cassoux, M. Tokumoto, H. Akutsu, H. Kobayashi, and A. Kobayashi, Synth. Met. **103**, 1861 (1999).

[61] K. Shimada, N. Tajima, K. Kajita, and Y. Nishio, J. Phys. Soc. Jpn. **85**, 023601 (2016).

[62] K. Hiraki, M. Kitahara, T. Takahashi, H. Mayaffre, M. Horvatić, C. Berthier, S. Uji, H. Tanaka, B. Zhou, A. Kobayashi, and H. Kobayashi, J. Phys. Soc. Jpn. **79**, 074711 (2010).

[63] S. Sugiura, K. Shimada, N. Tajima, Y. Nishio, T. Terashima, T. Isono, A. Kobayashi, B. Zhou, R. Kato, and S. Uji, J. Phys. Soc. Jpn. **86**, 014702 (2017).

[64] Y. Oshima, H. Cui, and R. Kato, Magnetochemistry **3**, 10 (2017).

[65] T. Konoike, S. Uji, N. Nishimura, K. Enomoto, H. Fujiwara, B. Zhang, and H. Kobayashi, Physica B 359-361, 457 (2005).

[66] K. Shimada, N. Tajima, K. Kajita, and Y. Nishio, J. Phys. Soc. Jpn. **85** 023601 (2016).

[67] A. M. Clogston, Phys. Rev. Lett. **9**, 266-267 (1962).

[68] Y. Matsuda and H. Shimahara, J. Phys. Soc. Jpn **76**, 051005 (2007).

[69] Y. Kamihara, T. Watanabe, M. Hirano, and H. Hosono, J. Am. Chem. Soc. **130**, 3296-6297 (2008).

[70] A. Gurevich, Rep. Prog. Phys. **74**, 124501 (2011).

[71] T. Terashima, K. Kihou, M. Tomita, S. Tsuchiya, N. Kikugawa, S. Ishida, C. Lee, A. Iyo, H. Eisaki, and S. Uji, Phys. Rev. B **87**, 184513 (2013).

[72] C. Cho, J. H. Yang, N. F. Q. Yuan, J. Shen, T. Wolf, and R. Lortz, Preprint, Phys. Rev. Lett. **119**, 217002 (2017).

[73] J. Muller, M. Lang, F. Steglich, J. A. Schlueter, A. M. Kini, U. Geiser, J. Mohtasham, R. W. Winter, G. L. Gard, T. Sasaki, and N. Toyota, Phys. Rev. B **61**, 11739-11744 (2009).

[74] K. Cho, B. E. Smith, W. A. Coniglio, L. E. Winter, C. C. Agosta, and J. A. Schlueter, Phys. Rev. B 79, 220507(R) (2009).

[75] G. Koutroulakis, H. Khne, J. A. Schlueter, J. Wosniza, and S. Broun, Phys. Rev. Lett. **116**, 067003 (2016).

[76] R. Beyer, B. Bergk, S. Yasin, J. A. Schlueter, and J. Wosnitza, Phys. Rev. Lett. 109, 027003 (2012).

[77] J. Singleton, J. A. Symington, M.-S. Nam, A. Ardavan, M. Kurmoo, and P. Day, J. Phys.: Condens. Matter 12, L641 (2000).

[78] B. Bergk, A. Demuer, I. Sheikin, Y. Wang, J. Wosnitza, Y. Nakazawa, and R. Lortz, Phys. Rev. B **83**, 064506 (2011).

[79] C. C. Agosta, J. Jin, W. A. Coniglio, B. E. Smith, K. Cho, I. Stroe, C. S. Martin, W. Tozer, T. P. Murphy, E. C. Palm, J. A. Schlueter, and M. Kurmoo, Phys. Rev. B **85**, 214514 (2012).

[80] H. Mayaffre, S. Horvatic, M. Horvatic, C. Berthier, K. Miyagawa, K. Kanoda, and V. F. Mitrovic, Nat. Phys. **10**, 928-932 (2014).

[81] S. Tsuchiya, J. Yamada, K. Sugii, D. Graf, J. S. Brooks, T. Terashima, and S. Uji, J. Phys. Soc. Jpn. 84, 034703 (2015).

[82] C. C. Agosta, N. A. Fortune, S. T. Hannahs, S. Gu, L. Liang, J.-H. Park, and J. A. Schleuter, Phys. Rev. Lett. **118**, 267001 (2017).

[83] S. Uji, K. Kodama, K. Sugii T. Terashima, Y. Takahide, N. Kurita, S. Tsuchiya, M. Kimata, A. Kobayashi, B. Zhou, and H. Kobayashi, Phys. Rev. B **85**, 174530 (2012).

[84] M. A. Tanatar, T. Ishiguro, H. Tanaka, and H. Kobayashi, Phys. Rev. B **66**, 134503 (2002).

[85] W. A. Coniglio, L. E. Winter, K. Cho, C. C. Agosta, B. Fravel, and L. K. Montgomery, Phys. Rev. B **83**, 224507 (2011).

[86] S. Uji, K. Kodama, K. Sugii, T. Terashima, T. Yamaguchi, N. Kurita, S. Tsuchiya, T. Konoike, M. Kimata, A. Kobayashi,B. Zhou, and H. Kobayashi, J. Phys. Soc. Jpn. **84**, 104709 (2015).

[87] U. Geiser, J. A. Schlueter, H. H. Wang, A. M. Kini, J. M. Williams, P. P. Ache, H. I. Zakowicz, M. L. VanZile, and J. D. Dudek, J. Am. Chem. Soc. **118**, 9996-9997 (1996).

[88] J. C. Martinez, S. H. Brongersma, A. Koshelev, B. Ivlev, P. H. Kes, R. P. Griessen, D. G. de Groot, Z. Tarnavski, and A. A. Menovsky, Phys. Rev. Lett. **69**, 2276-2279 (1992).

[89] Beckman, D. S. Wanka, J. Wosnitza, J. A. Schlueter, J. M. Williams, P. G. Nixon, R. W. Winter, G. L. Gard, J. Ren, and M. -H.Whangbo, Whangbo, Eur. Phys. J. B **1**, 295-300 (1998).

[90] S. Wanka, J. Hagel, D. Beckmann, J. Wosnitza, J. A. Schlueter, J. M. Williams, P. G. Nixon, R. W. Winter, and G. L. Gard, Phys. Rev. B **57**, 3084 (1998).

[91] S. Yasuzuka, S. Uji, T. Terashima, K. Sugii, T. Isono, Y. Iida, and J. A. Schlueter, J. Phys. Soc. Jpn. **84**, 094709 (2015)

[92] J. Wosnitza, J. Hagel,1 J. S. Qualls, J. S. Brooks, E. Balthes, D. Schweitzer, J. A. Schlueter, U. Geiser, J. Mohtasham, R. W. Winter, and G. L. Gard, Phys. Rev. B **79**, 180506(R) (2002).

[93] T. Konoike, K. Uchida, T. Osada, T. Yamaguchi, M. Nishimura, T. Terashima, S. Uji, and J. Yamada, Phys. Rev. B **79**, 054509 (2009).

[94] F. Zuo, P. Zhang, X. Su, J. S. Brooks, J. A. Schlueter, J. Mohtasham, R. W. Winter, and G. L. Gard, J. Low Temp. Phys. **117**, 516 (1999).

[95] S. Ryu, S. Doniach, G. Deutscher, and A. Kapitulnik, Phys. Rev. Lett. **68**, 710-713 (1992).

[96] G. Blatter, V. B. Feigel'man, A. I. Larkin, and V. M. Vinokur, Vortices in high-temperature supercondoctors. Rev. Mod. Phys. **66**, 1125-1388 (1994).

[97] C. Rossel, P. Bauer, D. Zech, J. Hofer, M. Willemin, and H. Keller, J. Appl. Phys. **79**, 8166 (1996).

[98] L. Balicas, J. S. Brooks, K. Storr, S. Uji, M. Tokumoto, H. Tanaka, H. Kobayashi, A. Kobayashi, V. Barzykin, and L. P. Gorkov: Phys. Rev. Lett. **87**, 067002 (2001).

[99] W. A. Coniglio, L. E. Winter, K. Cho, C. C. Agosta, B. Fravel, and L. K. Montgomery, Phys. Rev. B **83**, 224507 (2011)

[100] K. Kajita, Y. Nishio, T. Takahashi, W. Sasaki, R. Kato and H. Kobayashi, A. Kobayashi, Y. Iye, Solid Stat. Comm. **70**, 1189 (1989).

[101] R. Lortz, Y.Wang, A. Demuer, P. H. M. Bottger, B. Bergk, G. Zwicknagl, Y. Nakazawa, and J. Wosnitza, Phys. Rev. Lett. **99**, 187002 (2007)

[102] B. Bergk, A. Demuer, I. Sheikin, Y. Wang, J. Wosnitza, Y. Nakazawa, and R. Lortz, Phys. Rev. B **83**, 064506 (2011)

[103] J. A. Wright, E. Green, P. Kuhns, A. Reyes, J. Brooks, J. Schlueter, R. Kato, H. Yamamoto, M. Kobayashi, and S. E. Brown, Phys. Rev. Lett. **107**, 087002 (2011).

[104] N. R. Werthamer K. Helfand, and P. C. Hohenberg, Phys. Rev. **147**-1, 295 (1966)

[105] V. G. Kogan Phys. Rev. B **24**, 1572 (1981)

[106] D. E. Farrell, S. Bonham, J. Foster, Y. C. Chang, P. Z. Jiang, K. G. Vandervoort, D. L. Lam, and V. G. Kogan, Phys. Rev. Lett. **63**, 782 (1989)

[107] K. Okuda, S. Kawamata, S. Noguchi, N. Ito, and K. Kadowaki, J. Phys. Soc. Jpm. **60**, 3226 (1991)

[108] K. E. Gray, R. T. Kampwirth, and D. E. Farrell, Phys. Rev. B **41**, 819 (1990)

[109] G. Blatter, M. V. Feigel'man, V. B. Geshkenbein, A. I. Larkin, and V. M. Vinokur, Rev.Mod. Phys. **66**, 1125 (1994)

[110] G. Blatter, B. Ivlev, and Y. Kagan, Phys. Rev. B **50**17, 13013 (1994)

[111] M. Tachiki, S. Takahashi, P. Gegenwart, M. Weiden, M. Lang, C. Geibel, F. Steglich, R. Modler, C. Paulsen, and Y. Onuki, Z. Phys. B **100**, 369 (1996)

Acknowledgments

I would like to thank everyone who supported me in this work.

First, I express my immeasurable gratitude to my supervisor Prof. S. Uji for giving me the opportunity to work on the fascinating and interesting problems of organic conductors.

I am sincerely grateful to my dissertation committee: Prof. X. Hu, Prof. A. Kanda, and Associate Prof. T. Yamaguchi for their valuable comments and suggestions to improve this dissertation, without which accomplishing this dissertation would not have been possible.

I want to thank all my collaborators.

I would like to express my gratitude to Prof. A. Kobayashi, Prof. H. Kobayashi, and Prof. B. Zhou from Nihon University; Prof. R. Kato from RIKEN; and Dr. J. A. Schlueter from Argonne National Laboratory for providing me high quality samples, without which I could not successfully conducted all the experiments.

I would like to express my gratitude to Prof. Y. Nishio, Prof. N. Tajima, Prof. K. Kajita, and Dr. K. Shimada from the Toho University for their insightful discussions.

I would like to express my gratitude to Prof. S. Yasuzuka from Hiroshima Institute of Technology for providing me with useful discussions and advice.

I would like to express my deep gratitude to all the colleagues in Quantum Transport Properties Group, National Institute for Materials Science (NIMS).

I am grateful to Prof. T. Terashima for providing me valuable advice. His guidance has been a great help in my experiments.

Dr. N. Kikugawa and Dr. Tsuda also gave me valuable discussions. I would like to express my gratitude to them too.

I am also grateful to Ms. Y. Shibata and Ms. M. Saito for supporting our experiments and lives in NIMS.

I would like to express my gratitude to Dr. T. Isono, Dr. Konoike, Dr. K. Sugii, Dr. K. Shimada and Dr. H. Hirose for their valuable time and the many extensive discussions.

I also thank my friends in my doctoral and master courses, especially T. Agatsuma, R. Kurimoto, R. Mizuta, Y. Nakagawa, and Y. Shimada.

I am very grateful to NIMS for making my Ph.D. study possible with the financial support.

Finally, I express my deep gratitude to my family, especially my parents, grandparents, sister, and brother, for their ongoing and never-ending support and encouragement.

Shiori Sugiura

Publications

Refereed papers published in journals (first author)

- S. Sugiura, K. Shimada, N. Tajima, Y. Nishio, T. Terashima, T. Isono, A. Kobayashi, B. Zhou, R. Kato, and S. Uji "Charge Transport in Antiferromagnetic Insulating Phase of Two-Dimensional Organic Conductor $\lambda-(\mathrm{BETS})_2\mathrm{FeCl}_4$" Journal of the Physical Society of Japan, vol. 85, P. 064703, 2016.

- S. Sugiura, K. Shimada, N. Tajima, Y. Nishio, T. Terashima, T. Isono, R. Kato, and S. Uji "Magnetic Torque Studies in Two-Dimensional Organic Conductor $\lambda-(\mathrm{BETS})_2\mathrm{FeCl}_4$" Journal of the Physical Society of Japan, vol. 86, P. 014702, 2017.

- S. Sugiura, K. Shimada, N. Tajima, Y. Nishio, T. Terashima, T. Isono, B. Zhou, R. Kato, and S. Uji "Magnetocaloric Effect Studies in Layered Organic Conductor $\lambda-(\mathrm{BETS})_2\mathrm{FeCl}_4$" (Accepted to Journal of the Physical Society of Japan).

Refereed papers published in journals (co-author)

- S. Uji, Y. Fujii, S. Sugiura, T. Terashima and T. Isono, and J. Yamada "Quantum vortex melting and phase diagram in the layered organic superconductor κ-(BEDT-TTF)$_2$Cu(NCS)$_2$" Physical Review B **97**, 024505 (2018).